

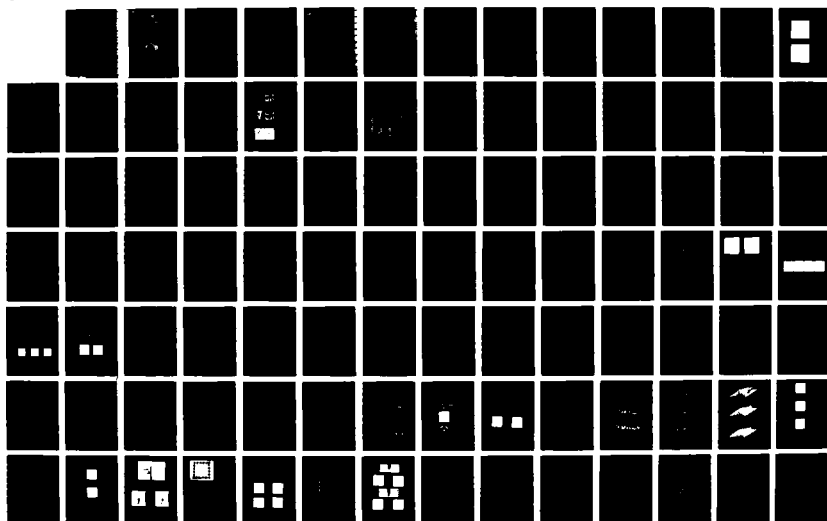
NO-A181 252

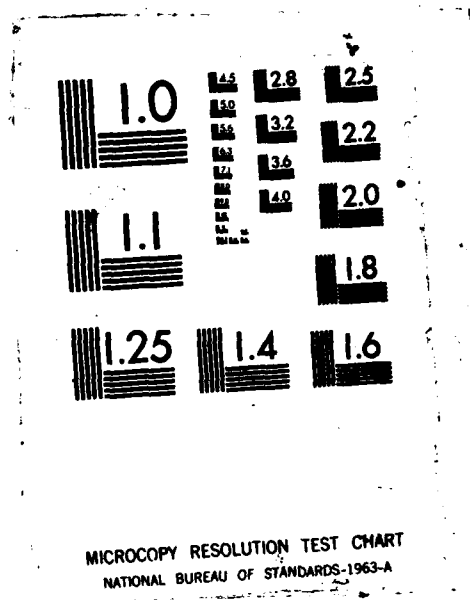
RESEARCH IN IMAGE UNDERSTANDING AS APPLIED TO 3-D
 MICROWAVE TOMOGRAPHIC I. (U) MOORE SCHOOL OF ELECTRICAL
 ENGINEERING PHILADELPHIA PA ELECTR. N H FARHAT MAR 87
 EO/NO-10 AFOSR-TR-87-0741 AFOSR-81-0240 F/G 17/9

1/2

UNCLASSIFIED

NL





DTIC FILE COPY

AD-A181 252



2305 / 41

(2)

AFOSR-TR- 87-0741

UNIVERSITY of PENNSYLVANIA

PHILADELPHIA, PENNSYLVANIA 19104

DTIC
ELECTE
JUN 08 1987
S D

DISTRIBUTION STATEMENT A

Approved for public release
Distribution Unlimited

87 6 5 072

UNIVERSITY OF PENNSYLVANIA
THE MOORE SCHOOL OF ELECTRICAL ENGINEERING
PHILADELPHIA, PA 19104

FINAL REPORT

RESEARCH IN IMAGE UNDERSTANDING AS APPLIED TO
3-D MICROWAVE TOMOGRAPHIC IMAGING WITH NEAR OPTICAL RESOLUTION

PREPARED BY
N.H. FARHAT

FOR

AIR FORCE OFFICE OF SCIENTIFIC RESEARCH
BUILDING 410, BOLLING AIR FORCE BASE
D.C. 20332

UNDER GRANT
AFOSR 81-0240

E.O/M.O REPORT 10

MARCH 1987



Accession For	
NTIS	CRA&I <input checked="" type="checkbox"/>
DTIC	TAB <input type="checkbox"/>
Unannounced	<input type="checkbox"/>
Justification	
By	
Distribution	
Availability Codes	
Dist	Avail and/or Special
A-1	

The findings in this report are those of the author and are not to be interpreted as the official position of the Air Force Office of Scientific Research or the U.S. Government.

UNCLASSIFIED

SECURITY CLASSIFICATION OF THIS PAGE (When Data Entered)

REPORT DOCUMENTATION PAGE		READ INSTRUCTIONS BEFORE COMPLETING FORM
1. REPORT NUMBER AFOSR-JR-87-0741	2. GOVT ACCESSION NO.	3. RECIPIENT'S CATALOG NUMBER
4. TITLE (and Subtitle) RESEARCH IN IMAGE UNDERSTANDING AS APPLIED TO 3-D MICROWAVE TOMOGRAPHIC IMAGING WITH NEAR OPTICAL RESOLUTION		5. TYPE OF REPORT & PERIOD COVERED Final 8/1/80 - 12/31/86
		6. PERFORMING ORG. REPORT NUMBER EO/MO 10
7. AUTHOR(s) Nabil H. Farhat		8. CONTRACT OR GRANT NUMBER(s) AFOSR-81-0240
9. PERFORMING ORGANIZATION NAME AND ADDRESS University of Pennsylvania The Moore School of Electrical Engineering 200 S. 33rd St., Phila., PA 19104-6390		10. PROGRAM ELEMENT, PROJECT, TASK AREA & WORK UNIT NUMBERS 61102F 2305/B1
11. CONTROLLING OFFICE NAME AND ADDRESS United States Air Force Air Force Office of Scientific Research Building 410, Bolling AFB, D.C. 20332 NE		12. REPORT DATE March, 1987
14. MONITORING AGENCY NAME & ADDRESS (if different from Controlling Office) same as 11		13. NUMBER OF PAGES 167
		15. SECURITY CLASS. (of this report) Unclass
15a. DECLASSIFICATION/DOWNGRADING SCHEDULE		
16. DISTRIBUTION STATEMENT (of this Report) Approved for public release; distribution unlimited.		
17. DISTRIBUTION STATEMENT (of the abstract entered in Block 20, if different from Report)		
18. SUPPLEMENTARY NOTES		
19. KEY WORDS (Continue on reverse side if necessary and identify by block number) Diversity imaging, 3-D tomographic imaging radar, range-profile, filtered back-projection, target derived reference, projection imaging, sinogram representation, neural net models, optical analogs, associative memory, target recognition, super-resolution.		
20. ABSTRACT (Continue on reverse side if necessary and identify by block number) Microwave diversity imaging is shown to be a cost-effective means for achieving 3-D tomographic imaging or projective imaging of aerospace objects with near optical resolution. This is achieved by combining spectral, angular, and polarization degrees of freedom in the physical optics regime to maximize the amount of information about a scattering target collected by a highly thinned broad-band aperture. In this research program the role of all three diversities is thoroughly investigated and understood both theoretically and		

experimentally. An *Experimental Microwave Imaging facility* is used to carry out scattering measurements of scale-models of targets of interest in an anechoic chamber environment. Automated scattered field measurements with unprecedented accuracy are possible for any state of polarization in the (2-26.5) GHz range with extension to 40 GHz nearly completed. Smart data acquisition with which one can efficiently access the 3-D Fourier space of a scattering object over any range of aspect angles are made possible with the facility. Two equivalent image reconstruction algorithms: *Fourier inversion* of interpolated polar formatted data and *filtered back projection* have been developed and refined. The filtered back-projection algorithm is found to be more directly related to the physical scattering mechanism of plane wave illumination at a conducting target. Our research has led to the development of a *target derived reference (TDR)* technique in which aspect dependent *range-profile* information is utilized to form a *sinogram representation* of the scattering centers on the target. When the multiaspect range profiles of the target are aligned properly, a clear sinogram pattern emerges. Point-like scattering centers on the target give rise to a sinusoidal trace or segment thereof in the pattern. A direct consequence of TDR is that a common phase reference is synthesized on the target and that the reconstructed image is always obtained centered within the image plane. In TDR, the phase of data acquired by arrays of independent pairs of broad-band coherent transmitter receivers that do not share a common phase reference can be referred to a common central point on the target. TDR also makes the imaging process more immune to atmospheric effects. This is specially useful when millimeter wave spectral windows are used for higher resolution. Because of the nature of scattering mechanisms of microwave (μw) and millimeter wave (mmw) illumination from man-made objects, images of such targets appear to be edge enhanced. The image thus contains only information about characteristic detail on the target, such as edges, outlines, protrusions etc., which aids recognitions by the eye-brain system and has attributes of a *primal sketch* that makes it also very useful for machine recognition. Techniques for accessing the Fourier space of a *moving scatterer* with the same accuracy realized with stationary objects in our imaging facility have also been studied. A doppler compensation scheme employing high speed frequency measurement and synthesis is found to be the most promising.

Resolution in $\mu w/mm w$ diversity imaging is proportional, among other things, to the width of the spectral window over which data is acquired. Very wide spectral windows can in principle yield images of remote targets e.g., aerospace targets with near optical resolution. The use of such extended spectral range is not possible in practice because of equipment limitation, frequency band allocation, and atmospheric effects. It is possible however to conduct measurements over separate segments of an extended spectral range. For this reason a new iterative algorithm for extrapolation of data available in multiple segmented regions covering an extended spectral range has been developed. For objects with discrete scattering centers, the algorithm is shown to furnish images with quality equal to the image obtained had the data been collected continuously over the entire extended spectral range. This result has obvious practical implications in that hardware complexity is traded by cheaper and more readily available computational expenditure. At the same time limitations imposed by frequency allocation and atmospheric effects are cleverly bypassed.

Atmospheric effects limit the spectral range useful for microwave diversity imaging to the lower mmw region. As a result the aperture (physical or synthetic) needed to realize high resolution on remote aerospace targets turns out to be very large as it must collect data for as wide a range of aspect

Abstract - Continued

EO/NO 10

March 1987

angles of the target as possible. It is worth recalling that different aspect "looks" at the target is what is needed for image formation. Although feasible, highly thinned, extended broad-band aperture of the type needed can be very costly. A single coherent broad-band transmitter/receiver can be used then in an ISAR (inverse SAR) mode to collect the data as the target is moving. This however is a non-real-time approach and can be time-consuming and even unacceptable in some situations when a large aperture is to be synthesized in order to achieve high resolution. One is faced then with the classical problem of how to recognize the target in microwave diversity imaging from a few looks i.e., the problem of super-resolution or target recognition from partial information.

For this reason a second approach to $\mu\text{m}/\text{mmw}$ target identification based on machine recognition where no explicit image formation takes place was pursued. This approach developed more recently in our research as a result of research in neural net models and their analogs as a new robust, high-speed, and fault tolerant approach to signal processing. A research effort in radar target recognition from partial information based on neural net models and their opto-electronic implementation has been initiated. Sinogram representations of targets of interest are considered as learning sets. The basic assumption here is that sinogram representations and other kinds of signatures, e.g., polarization maps, of scale models of targets of interest can be generated cost-effectively in our anechoic chamber facility to serve as learning sets for a neural processor that can be subsequently used in the recognition of the actual radar targets from few echoes collected by broad-band tracking radar systems. Careful attention is being given to scaling questions and to the principle of electromagnetic similitude in order to make the "laboratory" generated representations be as realistic as possible and therefore useful in the recognition of echoes obtained by any broad-band radar installation. Preliminary results show that a neural net processor is capable of distinguishing between models of three aero-space objects from a few looks on each corresponding to 10 to 20 percent of their corresponding sinogram representations. The neural net processor in this work performed the function of information storage, processing, and labeling of the target recognized simultaneously. Current work is considering the question of self-organization and learning in neural nets as a means for the net to generate its own representations of the items it is supposed to become familiar with rather than being deliberately programmed to do so as was the case in our preceeding work. Stochastic learning algorithms and fast opto-electronic analog architectures and implementations based on simulated annealing in the context of a Boltzmann machine formalism are being studied. Work in this area is being vigorously pursued as it might have far reaching implications in smart sensing and recognition and artificial intelligence systems. Simulated annealing as an optimization process has also been found in our work to be very useful in phased-array antenna pattern synthesis.

UNCLASSIFIED

TABLE OF CONTENTS

	<u>Page</u>
1. INTRODUCTION	1
2. SUMMARY OF IMPORTANT FINDINGS	2
3. LIST OF PUBLICATIONS	17
4. PARTICIPATING SCIENTIFIC PERSONNEL AND ADVANCED DEGREES EARNED	25
5. APPENDICES	26
I. Image Understanding and Interpretation in Microwave Diversity Imaging	
II. Radar Cross-Section Management Studies Employing Microwave Diversity Imaging	
III. A Multifunctional Microwave/Millimeter Wave Measurement Facility for Multi- Static Imaging and Target Classifica- tion Studies	
IV. Optical Analogs of Two-Dimensional Neural Networks and Their Application in Recognition of Radar Targets	
V. A New Iterative Algorithm for Extra- polation of Data Available in Multiple Restricted Regions with Applications to Radar Imaging	
VI. Architectures for Opto-Electronic Analogues of Neural Networks	
VII. Phased Array Antenna Pattern Synthesis by Simulated Annealing.	

RESEARCH IN IMAGE UNDERSTANDING AS APPLIED TO 3-D TOMOGRAPHIC
IMAGING WITH NEAR OPTICAL RESOLUTION

1. Introduction

Our research in high resolution microwave imaging shows that massive amounts of information about a scattering object can be gathered by measurements that combine angular, spectral and polarization diversity and trade-offs between spectral and angular degrees of freedom can be used to enhance cost effectiveness of microwave diversity imaging systems. The data collected can be used to access the 3-D Fourier space or p-space of the scatterer which can be Fourier inverted to yield 3-D image information either projectively or tomographically (in slices or cross-sectional outlines when the object is metallic). This indicates that three-dimensional microwave imaging of distant aerospace targets at resolutions comparable or exceeding the capabilities of optical imagers (whose operation is severely degraded by atmospheric effects) is feasible. The aim of research described in this report was to attain new levels of image understanding that are useful in the study and demonstration of 3-D microwave remote imaging with near optical resolution or better. Real-time operation and cost-effectiveness were of primary concern. Also the presentation of 3-D image detail to the observer in such a fashion as to aid recognition by the eye-brain system was an objective, although the study of automated identification and classification technique was not excluded and encouraging initial results in this regard have recently been obtained and are included here.

2. Summary of Important Findings

Achievement of the above goals required a new level of insight and understanding of the dynamics of electro-magnetic scattering and inverse scattering in general and those of microwave/millimeter wave diversity imaging in particular. This understanding has lead to the identification of imaging algorithms capable of judiciously combining smart data acquisition, signal processing including image enhancement and restoration, and efficient 3-D image presentation and display. New levels of insight and understanding developed by the program have also contributed to the development of generalized imaging theory applicable to all modes of coherent or incoherent, synthetic or nonsynthetic multidimensional (2-D and 3-D) imaging systems and to the development of new indirect imaging modalities where the object transform is the data collected and from which an image is formed. The availability of the object transform (e.g., Fourier transform) permits the application of sophisticated analysis and filtering methods that play a major role in facilitating the study of imaging processes. Progress in all these aspects has been reported in earlier annual reports, [1]-[4] and in journal articles and proceedings of technical meetings (see list of publications in section 3 of this report).

Real-time, cost-effective imaging of remote scattering objects with near optical resolution using microwaves (or millimeter waves) provides a valuable tool in several applications. These include damage assessment of satellites and other aero-space objects, identification and classification of ground vehicles and aero-space objects and debris with low proability of error, radar cross-section reduction (diaphanization) to reduce probability of detection, non-destructive evaluation (NDE) of critical dielectric and

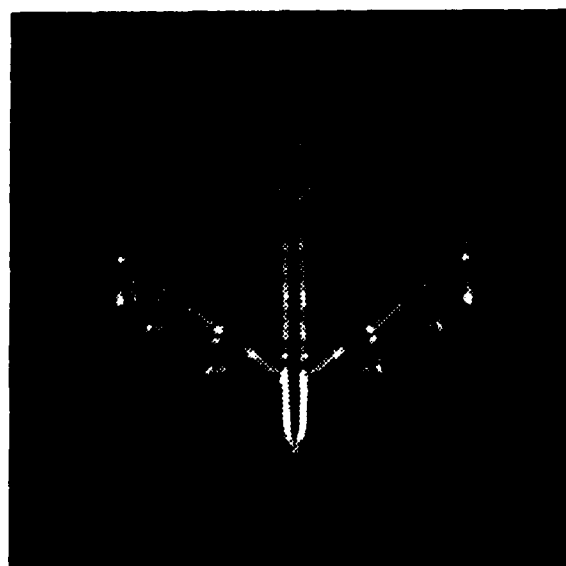
composite material components that do not lend themselves to other NDE techniques, and 3-D analysis and study of storm centers.

Specifically, the approach followed in this research is based on intelligent combination of thorough understanding of scattering mechanisms, image enhancement and restoration, with smart data acquisition over extended spectral windows that start in the lower microwave range and extend into the millimeter wave region. The argument for using extended spectral windows is found in the results of our λ and polarization diversity imaging work in the (6-18) GHz range described in the reports and publications cited earlier. These results made it abundantly clear that the utility of our Experimental Microwave Measurement and Imaging Facility described in earlier reports [1]-[2] can be drastically enhanced by extending its spectral range of operation down to 2 GHz and upto 40 GHz. In particular the reduction in the side-lobe level of the spatially variant point spread function (PSF) provided by inclusion of lower spectral frequencies and the ensuing reduction of speckle, indicated by an idealized analysis given in [1] are two obvious motives. Furthermore, extending operation down to 2 GHz provides probing wavelength ranges up to 15 cm which exceed the characteristic sizes of a number of sub-structures on the test objects utilized in our studies. For example the engines, fuel tanks, and tail section of a 100:1 scale model of a B-52 we frequently use as test target are all of the order of or less than 15 cm. This places scattering from these components in their Rayleigh or resonance regime and enhances image quality by causing a "filling-up" of the image. This leads for example to a desirable alteration of the image of the engines, appearing usually as two dots located at the ends of their nearly cylindrical shapes, to a more continuous image resembling more closely their optical image. It is possible of course to investigate Rayleigh and

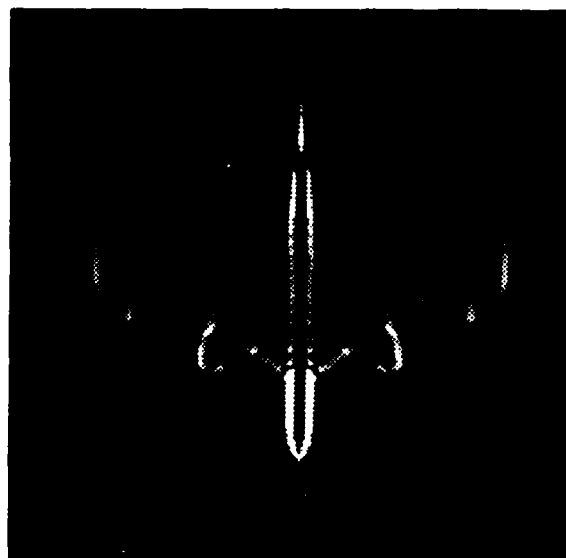
resonance scattering with a (6-18) GHz system by reducing the size of the test models employed. This however will result in an unacceptable reduction of the radar return necessitating the use of higher levels of irradiance at the target. The argument for extending the operational range up to 40 GHz stems from the desire to collect information about finer detail on the scaled target representing for example damaged structure on an actual target.

Figure 1 shows examples of two microwave diversity projection images of the scale model of a B-52 used as a test target in our experimental Microwave Imaging Facility. The image in Fig. 1(a) is obtained using a spectral window of (6-18) GHz while that in Fig. 1(b) is obtained with a spectral window of (2-18) GHz. The angular window of data acquisition in both cases was about 90° from head-on to broad-side in 128 looks. The spectral window were covered by incrementing the frequency in steps of ~ 86 MHz. The elevation angle in both cases was 30° . It is easily verified that the (2-18) GHz image exhibits improved delineation of detail such as the engines and fuel tanks as compared to the (6-18) GHz image. Also the fuselage and sail (vertical tail sections) are better delineated. The outlines of the wings and the tail are however de-emphasized somewhat in the (2-18) GHz image because of the effect of low frequency scattering data included in this image. Extension of the upper limit spectral window for example to 40 GHz while maintaining the 2 GHz lower limit is expected to restore the sharpness of the wings and tail section and to result in further image improvement.

The images shown are symmetry enhanced and polarization enhanced as described in earlier reports and publications and have been obtained by means of an elaborate target derived reference technique (TDR) developed and



(a)



(b)

Fig. 1. Microwave diversity projection images of 100:1 scale model of a B-52.
(a) spectral window of (6-18) GHz, (b) spectral window of (2-18) GHz.

refined in our work which removes the range-phase caused by the unknown range to a specific reference phase center on the target in order to be able to form an intelligible image.

Resolution in $\mu\text{w/mm}$ diversity imaging depends among other things on the width of the available spectral window. Extended spectral windows covering the μw and portions of the mmw range can lead to resolution on remote targets (e.g., aerospace targets) exceeding those of optical systems which are more susceptible to atmospheric effects than $\mu\text{w/mm}$ imaging systems. Hardware availability and frequency band allocation may limit however data acquisition in practice to nonoverlapping bands that can cover a wide spectral range. The question then is how to employ information collected in such multiple restricted frequency bands to retrieve by extrapolation into the missing bands an image of the target equivalent or approaching the quality of that obtained had the entire un-interrupted spectral range been available .

A new iterative method for extrapolation of incomplete segmented data available in multiple separated bands has therefore been proposed and tested. The method uses the Burg algorithm to find the linear prediction parameters and an iterative procedure to improve the estimation of the linear prediction parameters and extrapolation of the data. This method is especially effective when the spectra (Fourier transform of the observed data) are in discrete forms. In the context of radar imaging represented here, this means the object consist of discrete or distinctly spaced scattering centers. The advantage of this algorithm were demonstrated using both numerically generated and realistic experimental data pertaining to high resolution radar imaging. Detail of this work is given in Appendix V.

The image formation principle for microwave diversity imaging systems can be understood by investigating the scattering mechanisms of the object and the image reconstruction algorithms. After looking into these two factors, several numerical and experimental results can be satisfactorily explained. The image of a metallic object obtained using prescribed spectral and angular windows can be predicted accordingly. This successful interpretation is fundamental to research in radar cross section management studies and target imaging and recognition. Recent research in this regard and the results obtained are summarized in some detail in Appendix I.

The ultimate aim of all imaging systems is recognition and identification. In the microwave diversity imaging work described above, the recognition and identification is performed by an observer i.e. identification is done by the eye-brain system.

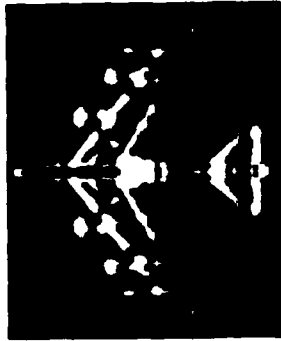
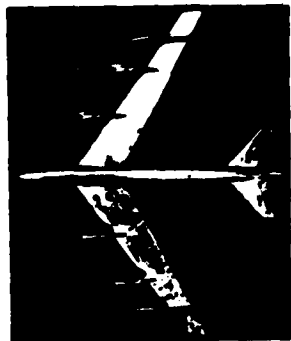
Another approach, to target identification which emerged more recently in our research, is less traditional than mere formation of a high resolution image suitable for human analysis. It involves automated machine recognition. Here we are concerned with issues of correct recognition and labeling by a machine from partial or sketchy information and with systems that can do this in a robust and fault tolerant manner. In this new approach, the role of the eye-brain system in recognizing an image is mimicked by the machine which makes the recognition process "brain-like" in nature. The approach is based on neural net models and their opto-electronic analogs which exploits the fit between what optics can offer (parallelism and massive interconnectivity) and what neural net models can offer (new approach to signal processing that is nonlinear and collective and therefore fast, robust, and fault tolerant). The two approaches are coupled in that automated machine recognition with artificial neural

networks relies on the generation of target or object representations or feature spaces that can lead to "distortion tolerant" recognition i.e., recognition irrespective of target range, orientation, or location within the field of view i.e., what is traditionally referred to as scale, rotation, and shift invariant recognition. The generation of such representations usually involves the same gear employed in traditional $\mu\text{w}/\text{mmw}$ diversity imaging where spectral, angular, and polarization degrees of freedom are combined to realize images of the scattering targets with near optical resolution. In fact the representations or feature spaces often contain exactly the same information contained in a $\mu\text{w}/\text{mmw}$ image of the target except it is arranged in a different format that is more amenable for use in automated recognition schemes. This approach has lead to the emergence of a new concept of achieving the ultimate resolution through correct recognition of the target by a machine. In other words correct recognition of the target by a machine is synonymous with producing a very high resolution image with detail sufficient for reliable recognition by the eye-brain system and for discrimination between closely similar targets.

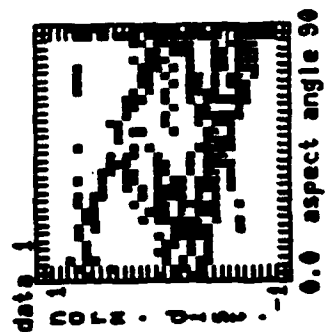
Among its many fascinating capabilities such as robustness and fault tolerance, the brain is also able to recognize objects from partial information. We can recognize a partially obscured or shadowed face of an acquaintance or a mutilated photograph of someone we know with little difficulty. The brain has a knack for supplementing missing information. Capitalizing on this feature and on our knowledge of neural models and their collective computational properties, (see 15 and 16 of list of publications) a study of "neural processing" for recognizing objects from partial information has been initiated. An example of the capabilities of this new

and intriguing approach in automated recognition and labeling of radar targets from partial information is given in Fig. 2. Details of this preliminary work is given in Appendix IV.

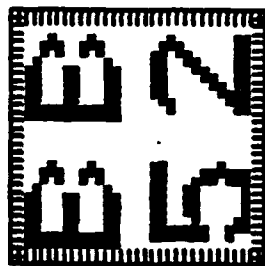
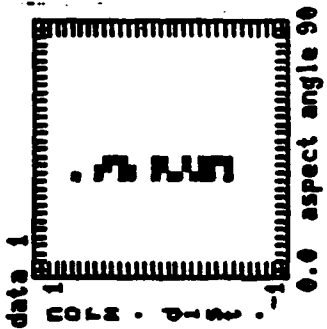
Object recognition employing hetero-associative memory based on models of neural networks may obviate the need for expensive or non real-time image formation in the field. Images of scale models of objects of interest and their sinogram representations are produced indoors in our microwave imaging facility at a fraction of the cost of an actual radar system operating to form images of actual targets intended for recognition by the eye-brain system. (See Appendix IV). The sinogram representations which can be viewed also as signatures or feature-spaces of targets of interest are taught to a hetero-associative memory by associating them with identifying letter labels. When such a hetero-associative memory is presented with partial sinogram information, that can be as low as 10% of the full sinogram, the memory will supplement the missing information and produce the correct label. This ability of supplementing missing information is synonymous with "super resolution". It is akin to our ability for example to recognize a photograph of someone we know even when part of it is missing or to understand a sentence in a handwritten letter even when some of the words are not legible. Partial sinogram information can be produced much more rapidly, easily, and economically in the field by actual radar systems than producing full sinogram or image. Thus a few looks at the target from slightly different aspects may be sufficient for recognition. The real challenge is to recognize the target from one look i.e., from one broadband radar echo and also for non-aerospace targets in the presence of clutter. The achievement of this aim employing artificial neural processors is a major objective of our current and future research. It is important to note



OPTICAL IMAGE (TOP) AND
RADAR IMAGE (BOTTOM) OF
SCALE MODEL OF B-52 AIR-
CRAFT PRODUCED AT THE
EXPERIMENTAL MICROWAVE
IMAGING FACILITY AT
THE UNIVERSITY OF
PENNSYLVANIA



(TOP) DIGITIZED SINOGRAM
REPRESENTATION OR SIGNA-
TURE OF B-52 TAUGHT WITH
OTHER SINOGRAMS (OF AN
AWAC AND A SPACE-SHUTTLE)
TO A HETERO-ASSOCIATIVE
MEMORY BASED ON MODELS
OF NEURAL NETS. (BOTTOM)
CORRECT LABEL PRODUCED
BY MEMORY WHEN IT WAS
PRESENTED WITH A COMPLETE
SINOGRAM OF THE B-52
SIGNIFYING THEREBY
RECOGNITION



SAME CORRECT LABEL OF
B-52 (BOTTOM) WAS PRODUCED
BY MEMORY WHEN PRE-
SENTED WITH PARTIAL SINO-
GRAM INFORMATION (10% OF
THE SINOGRAM REPRESENTA-
TION (TOP).

Fig. 2. Example of automated recognition of radar target employing hetero-associative memory based on models of neural network.

that, unlike a conventional memory in a computer, the hetero-associative memory here performs the functions of storage, processing, and recognition simultaneously. As such it is more correct to regard it as a "neural processor". A primary objective of our future research in this area is the study of generating realistic target representation employing scale models in an anechoic chamber environment. Careful consideration of scaling issues and of the principle of electromagnetic similitude^{*} are called for in order to be able to generate from scale models feature spaces (e.g., sinogram and polarization representations) that resemble those obtained had the actual object been interrogated in the field by a realistic broad-band radar system.

Our research during this period examined also several approaches to the problem of accessing the 3-D Fourier space of a scattering body undergoing irrotational motion. The criterion for selecting the best approach were speed, accuracy and economy. The method chosen, shown in Fig. 3, exploits recent advances in the state-of-the-art of Microwave instrumentation to enable the study of innovative and efficient approaches to data acquisition that were generally thought not to be feasible a short time ago. The scheme utilizes two capabilities of current microwave instrumentation. High speed computer controlled frequency synthesis and high-speed frequency measurement. These capabilities are combined in the arrangement shown to realize rapid determination of the doppler shift F_D in the signal scattered from the moving scatterer (target) which can then be compensated for in the phase and amplitude measurement of the scattered field carried out by the coherent receiver (hp 8410B Network Analyzer) whose intermediate

^{*} J.D. Stratton, Electromagnetic Theory, McGraw Hill, New York (1941). pp. 488-490.

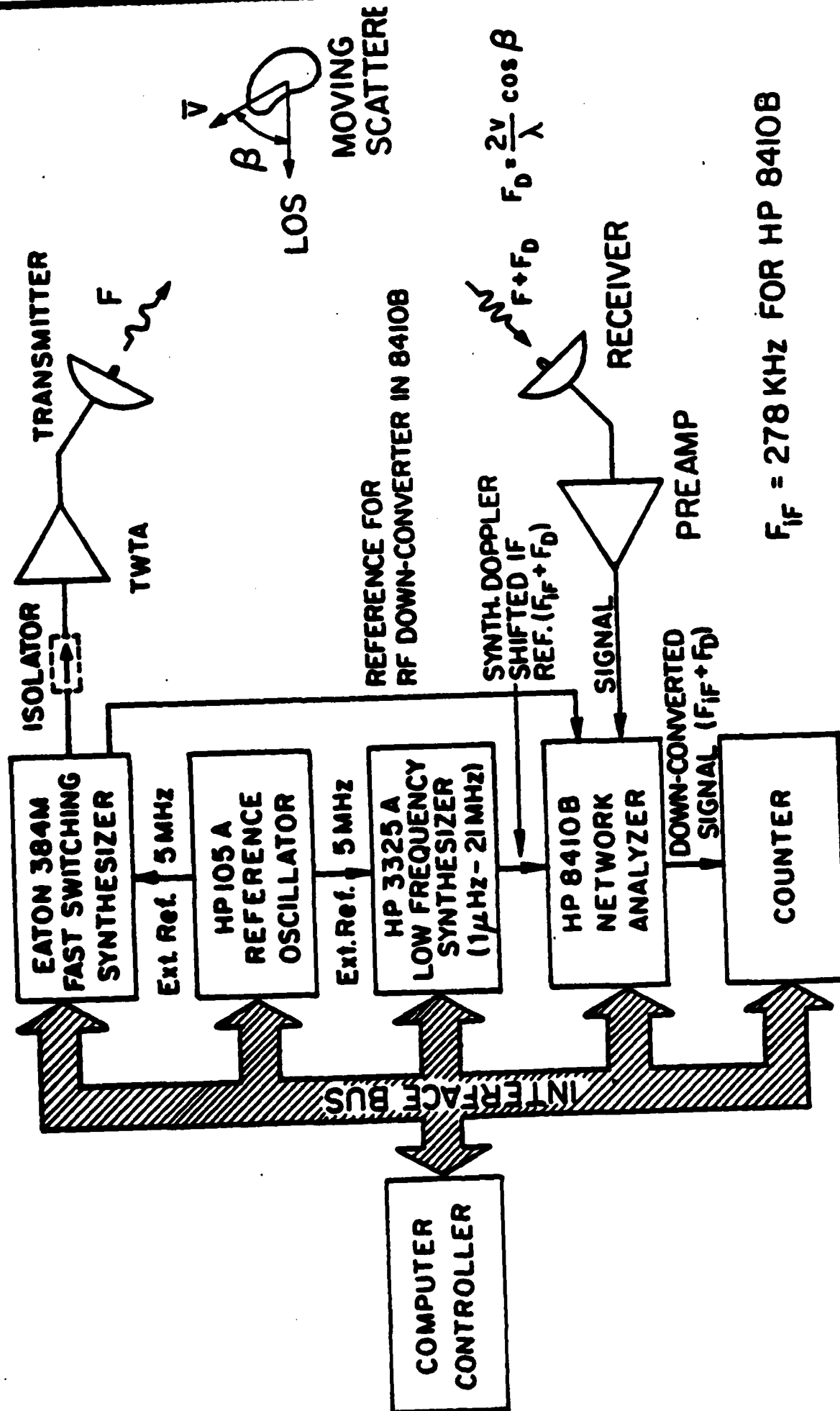


Fig. 3. Doppler compensated arrangement for measuring the stepped frequency response of a moving scatterer.

local oscillator is effectively made to equal $F_{RF} + F_D$ using an externally synthesized signal at frequency $F_{IF} + F_D$ for the reference IF channel of the network analyzer. This eliminates the effect of Doppler shift on the phase measurement and provides data very much similar to that generated had the target been stationary and it merely changes its aspect relative to the line of sight of the interrogating radar system. Note the low frequency synthesizer source of the $F_{IF} + F_D$ signal, the hp 3325A synthesizer, is phase-locked to the RF source of illumination of the target. This synthesized source has been carefully chosen because its high frequency resolution which enables setting the doppler shift of the IF reference precisely to the measured value of F_D . This frequency resolution is necessary because any discrepancy between the intermediate frequency (IF) reference signal and the down converted IF version of the target echo signal in the network analyzer results in an undesirable time varying phase error. In this arrangement the complex frequency response of the moving scatterer is measured rapidly in discrete frequency steps following the determination of the doppler shift and the setting of the low frequency intermediate frequency reference synthesizer to $(F_{IF} + F_D)$. If we assume that 100 frequency stepped measurements per second, as limited by the bandwidth of the phase/amplitude measuring segment of the network analyzer, can be performed, then the Doppler shift during this interval is expected to change negligibly for most practical targets including aerospace targets. Therefore the Doppler measurement and doppler compensation operation need not be performed frequently by the system but only occasionally or at most once at the beginning of each digital frequency sweep.

All the instrumentation to verify this scheme is now available in our laboratory with the exception of the hp 3325A low frequency synthesizer. In the next phase of this research we plan to either purchase or lease this instrument in order to carry out this experiment.

As described earlier, the smart sensing capabilities of our μ w/mmW diversity imaging approach were exploited to generate target representations (sinogram representations or feature spaces) which were used in turn to compute the synaptic connectivity matrix of the neural net processor. This operation is equivalent to deliberate programming of the neural net processor to perform certain pattern recognition task. One of the most intriguing and potentially useful properties of neural nets is their ability to self-organize and learn where the net forms its own internal representations of the associations it is presented with by internally altering the weights of interconnections between its neurons in accordance to some learning algorithm. Self-organization and learning in neural nets by simulated annealing in the context of a Boltzmann machine formalism is one of their attributes that sets them apart from other approaches to signal processing. Self organization and learning in neural nets can play an important role in the development of smart sensing, artificial intelligence, and high-speed knowledge processing systems.

Simulated annealing is known to be an effective tool in the solution of combinatorial optimization problems where an "energy" or "cost" function is to be minimized as a means of finding a solution. It has been applied in the solution of a wide range of combinatorial optimization problems. We have found recently that it can also be an effective tool in phased array antenna design where simulated annealing is applied to determine the binary (+1,-1) weights of the phased array elements that yield an optimal radiation

pattern as far as beamwidth and side-lobe level are concerned. Detail of this work is given in Appendix V.

REFERENCES

1. N.H. Farhat, "High-Resolution 3-D Tomographic Imaging by Wavelength and Polarization Diversity", Univ. of Pennsylvania, Annual Research Report, prepared under grant AFOSR-81-0240, submitted to Air Force Office of Scientific Research, July 1982.
2. N.H. Farhat, "High Resolution 3-D Tomographic Imaging by Wavelength and Polarization Diversity", Annual Research Report, prepared under grant AFOSR-81-0240B, submitted to Air Force Office of Scientific Research, July 1983.
3. N.H. Farhat, "Research in Image Understanding as Applied to 3-D Tomographic Imaging with Near Optical Resolution", Univ. of Pennsylvania Annual Research Report, prepared under grant AFOSR-81-0240C, submitted to Air Force Office of Scientific Research, Nov. 30, 1984.
4. N.H. Farhat, "Research in Image Understanding as Applied to 3-D Tomographic Imaging with Near Optical Resolution", Univ. of Pennsylvania Annual Research Report, prepared under grant AFOSR-81-0240C, submitted to Air Force Office of Scientific Research, March, 1986.

3. LIST OF PUBLICATIONS
Journal and Conference Proceeding Publication:

1. G. Tricoles and N.H. Farhat, "Unconventional Imaging", ICO-12 Proceedings, Taylor and Francis Ltd., Hampshire, England, 1981.
2. C.K. Chan and N.H. Farhat, "Frequency Swept Imaging of Three Dimensional Perfectly Reflecting Objects", IEEE Trans. on Antennas and Propagation - Special Issue on Inverse Scattering, Vol. AP-29, March 1981, pp. 312-319.
3. N.H. Farhat, "Holography, Wavelength Diversity and Inverse Scattering", in Optics in Four Dimensions - 1980, M.A. Machado and L.M. Narducci (Eds.), American Inst. of Phys. publication, New York (1981), pp. 627-642.
4. N.H. Farhat and C.Y. Ho, "The Virtual Fourier Transform and its Application to Three-Dimensional Display", in Optics in Four Dimensions, M.A. Machado and L.M. Narducci (Eds.), American Institute of Physics publication, New York (1981), pp. 341-354.
5. N.H. Farhat, C. Yi Ho and Lie Szu Chang, "Projection Theorems and Their Application in Multidimensional Signal Processing", Advances in Optical Information Processing, G. Michael Morris, Editor, Proc. SPIE 388, pp. 140-149, (1983).
6. N.H. Farhat, T.H. Chu and C.L. Werner, "Tomographic and Projective Reconstruction of 3-D Image Detail in Inverse Scattering", Proc. 10-th Int. Optical Computing Conference, IEEE Cat. No. 83CH7880-40, pp. 82-88, (1983).
7. N.H. Farhat, C.L. Werner and T.H. Chu, "Prospects of 3-D Tomographic Imaging Radar Networks", Proc. of the 1983 URSI Symposium on Electromagnetic Theory, Santiago de Compostella, Spain, pp. 297-301 (1983). (An expanded version of this paper has also been submitted to Radio Science by invitation).
8. D.L. Jaggard and A.K. Jordan, "Inversion Theory for Almost Periodic Media", Proc. of the 1983 URSI Symposium on Electromagnetic Theory, Santiago de Compostella, Spain, pp. 263-266 (1983).
9. N.H. Farhat, "Projection Imaging of 3-D Microwave Scatterers with Near Optical Resolution", in Indirect Imaging, J.A. Roberts (Ed.), Cambridge University Press (1984).
10. N.H. Farhat, C.L. Werner, and T.H. Chu, "Prospects for Three-Dimensional Projective and Tomographic Imaging Radar Networks", Radio Science, Vol. 19, September-October, 1984, pp. 1347-1355.
11. N. Farhat, C.L. Werner and T.H. Chu, "Prospects for 3-D Tomographic Imaging Radar Networks", Proc. URSI Symp. on Electro-Magnetic Theory, Santiago De Compostela, Aug. 1983, pp. 279-301.

12. D.L. Jaggard and A.K. Jordan, "Inversion Theory for Almost Periodic Media", Radio Science, Vol. 19, September-October, 1984, pp. 1333-1341.
13. N.H. Farhat, et. al., "Optical Implementation of the Hopfield Model", Applied Optics, Vol. 24, May 1985, pp. 1469-1475.
14. N. Farhat and T.H. Chu, "Tomography and Inverse Scattering", Proc. ICO-13, 13th Congress of the International Commission on Optics, Sapporo, Japan, 1984.
15. D. Psaltis and N. Farhat, "Optical Information Processing Based on an Associative-Memory Model of Neural Nets with Thresholding and Feedback", Opt. Lett., Vol. 10, 1985, pp. 98-100.
16. N.H. Farhat, et. al., "Optical Implementation of the Hopfield Model", Applied Optics, Vol. 24, May 1985, pp. 1469-1475.
17. D. Jaggard and Y. Kim, "Accurate One-Dimensional Inverse Scattering Using Nonlinear Renormalization Technique", J. Opt. Soc., Part A, Vol. 2, 1985.
18. D.L. Jaggard and K.E. Olson, "Numerical Reconstruction for Dispersionless Refractive Profiles", J. Opt. Soc., Part A, Vol. 2, Oct. 1985.
19. Y. Kim and D.L. Jaggard, "Inverse Blackbody Radiation: An Exact Closed-Form Solution", IEEE Trans. Antenna and Prop., Vol. AP-33, July, 1985, pp. 797-800.
20. D. Psaltis and N. Farhat, "A New Approach to Optical Information Processing Based on the Hopfield Model", 13-th Congress of the International Commission on Optics, ICO-13, Conference Digest pp. 24-25, Published by the Organizing Committee of ICO-13, Sapporo, Printed in Japan SML 8408, 1984.
21. N. Farhat, et. al., "Optical Analog of Two-Dimensional Neural Networks and Their Application in Recognition of Radar Targets", in Neural Networks and Computing, J.S. Denker (Ed.), Am. Inst. of Phys., New York, 1986, pp. 146-152.
22. N. Farhat, "Robust Signal Recovery and Recognition with Optical Analogs of Neural Nets and Spurious Memory Discrimination", SPIE Vol. 700, 1986, pp. 283-288.
23. T.H. Chu and N. Farhat, "Polarization Effects in Microwave Diversity Imaging of Perfectly Conducting Cylinders", IEEE Transactions on Antennas and Propagation, Accepted for publication.
24. H-J Li and N. Farhat, "A New Iterative Algorithm for Extrapolation of Data Available in Multiple Restricted Regions with Application to Radar Imaging", IEEE Trans. on Antennas and Propagation, Accepted for publication.
25. N. Farhat and B. Bai, "Phased Array Pattern Synthesis by Simulated Annealing", Proc. IEEE (Letters), Accepted for publication.

Related Earlier Publications

1. N.H. Farhat, "New Imaging Principle", Proc. IEEE (Letters), Vol. 64, pp. 379-380, March 1976.
2. N.H. Farhat, "Frequency Synthesized Imaging Apertures", Proc. 1976, International Optical Computing Conference, IEEE Cat. #76 CH 1100-7C, pp. 19-24.
3. N.H. Farhat, M.S. Chang, J.D. Blackwell and C.K. Chan, "Frequency Swept Imaging of a Strip", Proc. 1976, Ultrasonic Symposium, IEEE Cat. #76 CH 1120-5SU.
4. J.D. Blackwell and N.H. Farhat, "Image Enhancement in Longwave Holography by Electronic Differentiation", Optics Communications, Vol. 20, Jan. 1977, pp. 76-80.
5. N.H. Farhat, T. Dzekov and E. Ledet, "Computer Simulation of Frequency Swept Imaging", Proc. IEEE (Letters), Vol. 64, pp. 1453-1454, Jan. 1977.
6. G. Tricoles and N.H. Farhat, "Microwave Holography: Applications and Techniques", Invited paper, Proc. IEEE, Vol. 65, pp. 108-121, Jan. 1977.
7. C.K. Chan, N.H. Farhat, M.S. Chang and J.D. Blackwell, "New Results in Computer Simulated Frequency Swept Imaging", Proc. IEEE (Letters), Vol. 65, pp. 1214-1215, Aug. 1977.
8. N.H. Farhat, "Principles of Broad-Band Coherent Imaging", J. Opt. Soc. Am., Vol. 67, pp. 1015-1020, Aug. 1977.
9. N.H. Farhat, "Comment on Computer Simulation of Frequency Swept Imaging", Proc. IEEE, Vol. 65, pp. 1223-1226, Aug. 1977.
10. M.A. Kujorry and N.H. Farhat, "Microwave Holographic Substraction for Imaging of Buried Objects", Proc. IEEE (Letters), Vol. 66, pp. 94-96, Jan. 1978.
11. N.H. Farhat, "Comment on a New Imaging Principle", Proc. IEEE (Letters), Vol. 66, pp. 609-700, May 1978.
12. C.K. Chan, "Analytical and Numerical Studies of Frequency Swept Imaging", University of Pennsylvania, Ph.D. Dissertation (1978).
13. M.A. Kujoory and N.H. Farhat, "Format Generation for Double Circular Scanners For Use in Longwave Holography", Acoustical Imaging and Holography, Vol. 1, No. 2, pp. 133-141 (1979).
14. N.H. Farhat, "Microwave Holographic Imaging - Prospects for a Real-Time Camera", SPIE, Vol. 180, Real-Time Signal Processing, II, (1979).

15. N.H. Farhat and J. Bordogna, "An Electro-Optics and Microwave-Optics Program in Electrical Engineering", IEEE Trans. on Education - Special Issue on Optics Education, Vol. E-23, May 1980, pp. 76-83.
16. N.H. Farhat and C.K. Chan, "Three-Dimensional Imaging by Wave-Vector Diversity", Acoustical Imaging, Vol. 8, A. Methereil (ed.), Plenum Press, New York (1980), pp. 499-515.
17. N.H. Farhat, "Holographically Steered Millimeter Wave Antennas", IEEE Trans. on Antennas and Propagation, Vol. AP-28, July 1980, pp. 476-480.

Conference Presentations

1. N.H. Farhat, C.K. Chan and T.H. Chu, "A Target Derived Reference Technique for Frequency Diversity Imaging", Poster paper, presented at the North American Radio Science Meeting, June 1980, Quebec, Canada.
2. N.H. Farhat and C.Y. Ho, "The Virtual Fourier Transform and its Application to Three-Dimensional Display", presented at the ICO Symposium on Optics in Four Dimensions, Ensenada, Mexico, August 1980.
3. N.H. Farhat, "Holography, Wavelength Diversity and Inverse Scattering", Presented at the ICO Symposium on Optics in Four Dimensions, Ensenada, Mexico, August, 1980.
4. N.H. Farhat and C. Werner, "An Automated Microwave Measurement Facility for Three-Dimensional Tomographic Imaging by Wavelength Diversity", 1981 International IEEE/AP-S Symposium and National Radio Science Meeting, Los Angeles, June, 1981.
5. G. Tricoles and N.H. Farhat, "Unconventional Imaging", ICO-12, Gratz, Austria, Aug., 1981.
6. N.H. Farhat, "Projection Theorems and Their Applications in 3-D Tomographic Image Reconstruction and Display", Poster Session paper presented at the Gordon Research Conference on Holography and Optical Data Processing, Plymouth, N.H., June 1982.
7. N.H. Farhat, "Tomographic and Projective Reconstruction of 3-D Image Detail in Inverse Scattering", Presented at the 1983 URSI Meeting, Jan. 5-7, Boulder, Colorado.
8. N.H. Farhat, "Inverse Scattering Reconstructions From Incomplete Fourier Space Data", Presented at and published in the Technical Digest of the OSA/AFSOS 1983 Topical Meeting on Signal Recovery and Synthesis with Incomplete Information and Partial Constraints, Jan. 12-14, Lake Tahoe, Nev.
9. N.H. Farhat, C. Yi Ho, and Li Szu Chang, "Projection Theorems and their Applications in Multidimensional Signal Processing", Presented at the Conference on Advances in Optical Signal Processing at the SPIE LA/'83 Meeting, Jan. 1983, Also to be published in the Conference Proceeding.

10. N.H. Farhat, C.L. Werner and T.H. Chu, "Microwave Projection Imaging with Near Optical Resolution", Accepted for Presentation at the 1983 International Optical Computing Conference on "Unconventional Imaging and Unconventional Transformations", Boston April 1983. Published in Conference proceedings.
11. N.H. Farhat, C.L. Werner and T.H. Chu, "Prospects for 3-D Tomographic Imaging Radar Networks", Presented at the 1983 International URSI Meeting, Santiago De. Compostela, Spain.
12. N.H. Farhat, D. Jaggard, T.H. Chu, D.B. Ge and S. Mankoff, "Microwave Tomographic and Projective Imaging of Dielectric Bodies", Presented at the 1983 International IEEE APS/URSI Meeting, May 23-26, Houston, TX.
13. D.L. Jaggard and K.E. Olson, "Analytical and Numerical Strategies for Inverse Scattering from Almost Periodic Media", presented at the 3rd Annual Benjamin Franklin Symposium on Advances in Antenna and Microwave Technology", Philadelphia (1983).
14. N.H. Farhat, D.L. Jaggard, T.H. Chu, D.B. Ge and S. Mankoff, "Microwave Imaging of 3-D Dielectric Bodies", presented at the 3rd Annual Benjamin Franklin Symposium on Advances in Antennas and Microwave Technology, Philadelphia, (1983).
15. N.H. Farhat, D.L. Jaggard, T.H. Chu, D.B. Ge and S. Mankoff, "Microwave Tomographic and Projection Imaging of 3-D Dielectric Bodies", presented at the 1983 International IEEE/AP Symposium and National Radio Science Meeting, Houston (1983).
16. A.K. Jordan, S. Ahn and D.L. Jaggard, "Applications of Almost-Periodic Functions to Inverse Scattering Theory", presented at the NATO Advanced Research Workshop on Inverse Scattering Methods for Electromagnetic Imaging (1983).
17. N.H. Farhat and T.H. Chu, "Tomography and Inverse Scattering", in Optics in Modern Science and Technology, Proc. ICO-13, Sapporo, Japan, Aug. 1984, pp. 62-63.
18. D.L. Jaggard, et. al., "Tomographic Microwave Imaging", XXI General Assembly of the International Union of Radio Science, Florence, Italy, August-September 1984.
19. D. Psaltis and N. Farhat, "A New Approach to Optical Information Processing Based on the Hopfield Model", 13-th Congress of the International Commission on Optics, ICO-13, Sapporo, Japan.
20. N. Farhat and D. Psaltis, "Optical Implementation of the Hopfield Model", OSA Annual Meeting, San Diego, Oct. 1984.
21. D. Psaltis and N. Farhat, "Optical Computing Based on the Hopfield Model", OSA Topical Meeting on Optical Computing, Lake Tahoe, March 1985.

22. N. Farhat and D. Psaltis, "Opto-Electronic Implementations of the Hopfield Model", OSA Topical Meeting on Optical Computing, Lake Tahoe, March 1985.
23. N. Farhat and Y. Shen, "Microwave Imaging of Objects in the Presence of Severe Clutter", OSA Annual Meeting, Wash. D.C., 1985.
24. N. Farhat, et. al., "High Speed Fourier Camera", OSA Annual Meeting, Wash. D.C., 1985.
25. K.S. Lee and N. Farhat, "Content Addressable Memory with Smooth Transition and Adaptive Thresholding", OSA Annual Meeting, Wash. D.C., 1985.
26. N.H. Farhat and D. Psaltis, "Architectures of Optical Implementation of 2-D Content Addressable Memories", OSA Annual Meeting, Wash. D.C., 1985.
27. D. Psaltis, E. Paek, J. Hong, and N. Farhat, "An Acousto-Optic Implementation of Neural Network Models", Annual OSA Meeting, Wash. D.C., Oct. 1985.
28. D.L. Jaggard, K. Schultz, Y. Kim and P. Frangos, "Inverse Scattering for Dielectric Media", Annual OSA Meeting, Wash. D.C., Oct. 1985.
29. N. Farhat, T.H. Chu, C.L. Werner and Y. Shen, "Microwave Diversity Imaging with Near Optical Resolution", IEEE AP-S/URSI Meeting, Phila., 1986.
30. T.H. Chu and N. Farhat, "Multiple-Scattering Effects in Microwave Diversity Imaging", IEEE AP-S/URSI Meeting, Phila. 1986.
31. N.H. Farhat and S. Miyahara, "Super-Resolved Target Recognition and Classification Based on Models of Neural Networks", IEEE AP-S/URSI Meeting, Phila., 1986.
32. N.H. Farhat and Y. Shen, "Microwave Diversity Imaging of Objects in the Presence of Severe Clutter", IEEE AP/URSI Meeting, Phila., 1986.
33. C.L. Werner and N.H. Farhat, "Tomographic Imaging of 3-D Incoherent Objects Employing Spectrally Selective Correlation Measurements", IEEE AP-S/URSI Meeting, Phila., 1986.
34. N.H. Farhat, Y-J Li and Y. Shen, "Radar Cross-Section Management Studies Employing Microwave Diversity Imaging", IEEE AP-S/URSI Meeting, Phila., 1986.

Invited Talks

1. N.H. Farhat, "Microwave Holography and Coherent Tomography", Presented at the Electromagnetic Dosimetric Imagery Symposium held in conjunction with the 1980 IEEE/MTT-S International Microwave Symposium, Washington, D.C., May 1980.

2. N.H. Farhat, "Holography and Inverse Scattering", Presented at the First Dennis Gabor Memorial Symposium, Technion City, Haifa, Israel, March, 1980.
3. "Radar Imaging" California Inst. of Technology, Pasadena, Oct. 1984.
4. "3-D Tomographic Imaging Radar", General Dynamic, Ft. Worth Division, Ft. Worth Texas, Oct. 26, 1984. A video cassette recording of this lecture has been furnished courtesy of General Dynamics. A copy of this video tape was furnished to ARO with our Progress Report covering period 1 July 1984 to 31 December 1984.
5. "Smart Sensing and Recognition", Jet Propulsion Laboratory, Pasadena, Aug. 1985.
6. N. Farhat, "Tomographic Radar Imaging with Near Optical Resolution", Drexel University, Dept. of Electrical Engineering, Phila., Jan. 1985.
7. N. Farhat, "Tomographic Radar Imaging", AT&T Technology Systems and Bell Laboratories, National Engineering Week lecture series, Reading, Pa., Feb. 1985.
8. N. Farhat, "Optical Processing for 3-D Tomographic Imaging Radar", Sigma Xi Initiation Dinner. Bucknell University, March 1985.
9. N. Farhat, "Optical Computing Implementation for Neural Processing in the Eye-Brain System", Computer Chapter, IEEE N.J. Coast Section Seminar, April 1985.
10. N. Farhat, "Neural Networks and Optical Computing", DARPA Briefing, April 1985.
11. "Optical Implementation of Neural Nets", Workshop on Neural Networks for Computing, Santa Barbara, May, 1985.
12. "Tomographic Radar Imaging with Near Optical Resolution", Drexel University, Jan. 1986.
13. "Microwave Diversity Imaging and Automated Recognition", presented at the Reconnaissance, Surveillance and Target Acquisition (RSTA) Symposium Held at the Harry Diamond Laboratories, Adelphi, MD, Jan. 28-30 1986.
14. "Microwave Diversity Imaging and Automated Target Recognition", Univ. of California, Elect. Engrg. Dept., Feb. 1986.
15. "Smart Sensing and Image Recognition Based on Models of Neural Networks", AT&T Bell Communications Research Seminar, Feb., 1986.
16. "Neural Nets and Their Applications", Jet Propulsion Laboratory, Aug. 1986.

Other Activities

During the period of this report a group from the Western Space and Missile Center, Vandenberg, AFB, headed by Mr. Edgar Hall, visited our Laboratory on Aug. 17, 1983.

Dr. Farhat participated in the ERIM/Army Research Office Workshop on "Limits of Passive Imaging" held at Mackinac Island, Mich., May 1983 and spent a sabbatical leave at Caltech and JPL working on various aspects of radar imaging and optical information processing related to the research reported here.

N. Farhat has also been invited to participate in the NATO Advanced Study Institute on "EM Modelling and Measurements for Analysis and Synthesis Problem" to be held Aug. 1987 in Il Ciocco, Italy where he will lecture on "Microwave Diversity Imaging and Automated Target Recognition."

4. PARTICIPATING SCIENTIFIC PERSONNEL AND LIST OF DEGREES AWARDED:

N.H. Farhat - Principal Investigator
D.L. Jaggard - Co-Investigator
Lie Szu Chang - Graduate Student
T.H. Chu - Graduate Student (50%)
C.Y. Ho - Graduate Student (50%)
Y. Kim - Graduate Student (50%)
K.S. Lee - Graduate Student (50%)
P. Frangos - Graduate Student (50%)
Y. Shen - Graduate Student (50%)
K. Schultz - Graduate Student (50%)
S. Miyahara - Graduate Student (self-supported)
K.E. Olson - Graduate Student (self-supported)
C.L. Werner - Graduate Student

The following Ph.D. degrees were awarded during the period of this report:

1. C. Yi Ho, "Three-Dimensional Tomographic Image Reconstruction and Display", August 1982.
2. T.H. Chu, "Optimal Methodologies in Inverse Scattering", March 1982.
3. P. Frangos (Ph.D.) - "One-Dimensional Inverse Scattering: Exact Methods and Applications".
4. C.L. Werner (Ph.D.) - "3-D Imaging of Coherent and Incoherent Sources Utilizing Wave-vector Diversity",
5. S. Miyahara (Ph.D.) - "Automated Radar Target Recognition Based on Models of Neural Networks",

The following graduate students are in the last stages of completing their Ph.D. dissertations:

1. K.S. Lee (Ph.D.), "Smart Sensing and Recognition" (manuscript near completion)
2. Y. Shen (Ph.D.), "Dynamic Microwave Imaging", (manuscript near completion).
3. H-J. Li (Ph.D.), Microwave Image Understanding and Radar Cross-Section Management Studies (manuscript near completion).

5. APPENDICES

- I. Image Understanding and Interpretation in Microwave Diversity Imaging
- II. Radar Cross-Section Management Studies Employing Microwave Diversity Imaging.
- III. A Multifunctional Microwave/Millimeter Wave Measurement Facility for Multistatic Imaging and Target Classification Studies.
- IV. Optical Analogs of Two-Dimensional Neural Networks and their Application in Recognition of Radar Targets.
- V. A New Iterative Algorithm for Extrapolation of Data Available in Multiple Restricted Regions with Applications to Radar Imaging.
- VI. Architectures for Opto-Electronic Analogs of Neural Networks.
- VII. Phased Array Antenna Pattern Synthesis by Simulated Annealing.

Appendix I

IMAGE UNDERSTANDING AND INTERPRETATION IN MICROWAVE DIVERSITY IMAGING

Hsueh-Jyh Li, Nabil H. Farhat, Yuhsyen Shen, Charles Werner

The Moore School of Electrical Engineering
University of Pennsylvania
Philadelphia, PA. 19104

ABSTRACT

The image formation principle for microwave diversity imaging systems can be understood from investigating the scattering mechanisms of the object and the image reconstruction algorithms. After looking into these two factors, several numerical and experimental results can be satisfactorily explained. The image of a metallic object obtained by prescribed spectral and angular windows can be predicted accordingly. This successful interpretation is fundamental to research in radar cross section management studies and target recognition.

May 4, 1987

IMAGE UNDERSTANDING AND INTERPRETATION IN MICROWAVE DIVERSITY IMAGING

Hsueh-Jyh Li, Nabil H. Farhat, Yuhsyen Shen, Charles Werner

The Moore School of Electrical Engineering
University of Pennsylvania
Philadelphia, PA. 19104

I. INTRODUCTION

The image properties obtained by microwaves are different from those obtained by optical waves. The relative long wavelength of microwaves is the main reason. Optical wavelengths are usually smaller than the surface roughness of most objects. The surface can be seen through the waves scattered from the rough surface. The same surface might be smooth compared to microwave wavelengths, and therefore its microwave image can be entirely different from its optical counterpart.

Determination of the shape of a perfectly conducting body from a finite number of measurement of the scattered fields has been considered as an inverse scattering problem [1,2,3], where the input (the illuminating plane wave) is known and the outputs (the scattered far fields) are measured, and the object function to be determined is the geometrical shape of the body. It has been proven that under the physical optics (PO) approximation, the object function could be determined if the back-scattered fields could be measured for all frequencies and all directions[2,3]. In reality, the spectral and angular windows for the data are limited. Furthermore, the PO approximation will fail when the wavelength is not small compared to the characteristic dimension of the object. Therefore, the microwave image reconstructed over finite spectral and angular windows are not exactly the geometrical shape of the object.

Microwave images have been obtained by several different schemes, for example, side-looking radar, synthetic aperture radar (SAR), inverse synthetic aperture radar (ISAR)[4], radio camera [5], microwave holography [6], microwave diversity imaging [7,8], etc. Different schemes may produce different images and the images were interpreted in different ways. Radar workers modeled the object with a reflectivity distribution function [9], while electromagnetics workers modeled the object from more rigorous expressions [1,2,3]. The nature of the reconstructed images depends on the data acquisition systems and the reconstruction

algorithm. For example, the SAR image is derived using a range measuring technique in one dimension and the cross range coordinate is then introduced by processing many range returns along the synthesized aperture [9]. The effect of finite range resolution produces a "breaking up" of the image in the range direction that accentuates edges of the image and eliminates portions of the image which have constant intensity over long distances. The radio camera method treats the image problem from the antenna design point of view. Beamforming and scanning are the two main processes of the image reconstruction algorithm, and the element separation is in terms of wavelength [5]. Microwave diversity imaging systems make full use of angular, wavelength, and polarization diversity and to obtain images of metallic objects with nearly optical resolution [8]. 2-D Fourier transform method or filtered back-projection method are the image reconstruction algorithms of that imaging scheme. The image properties are close to those of SAR images.

The principle of microwave diversity imaging is based on the PO approximation and Born approximation. An object scattering function was first defined, and then it was shown that the object scattering function and the corrected scattered fields are 3-d Fourier transform pair. It was thought that the reconstructed image represents the object scattering function. However, if the position of the transmitter is changed, or if the object has been rotated, then the object scattering function cannot be defined clearly. This situation also occurs in SAR or ISAR images. What the image represents and how the image will look like over a given finite spectral and angular windows were not fully explained and discussed.

The principle of image formation for microwave diversity imaging system can be understood from investigating the scattering mechanism of the object and the procedures of the reconstruction algorithm. After looking into these two factors, several numerical and experimental results can be satisfactorily explained. Also, the image of a metallic object obtained by prescribed spectral and angular windows can be predicted accordingly.

In this paper, the microwave diversity imaging system will be briefly described; the scattering mechanism of the object and the procedures of the reconstruction algorithm will be studied; what the images represent and what the image will look like over prescribed angular and spectral windows will be interpreted and predicted; some numerical and experimental examples of reconstructed images will be given and discussed; an alternative interpretation of the edge enhancement property of microwave diversity image will be given and discussed.

II. DESCRIPTION OF MICROWAVE DIVERSITY IMAGING SYSTEMS

The simplified microwave diversity imaging arrangement is shown in Fig.1. A metallic object seated on a rotating pedestal is illuminated by a plane wave with unit amplitude. The distance between the rotation center O and the transmitter and receiver are R_t and R_r , respectively, the unit vectors in the direction of transmitter and receiver are \hat{l}_t and \hat{l}_r , respectively, and both are perpendicular to the rotation axis. Using the PO approximation and far field condition, the vector potential at the receiver can be expressed as [8]

$$\vec{A}(k, \hat{l}_t, \hat{l}_r) = \frac{jk}{4\pi R_r} e^{-jkR_r} \int_{S_{ill}} 2\hat{n}(\vec{r}') \times \hat{l}_H e^{jk[(\hat{l}_r - \hat{l}_t) \cdot \vec{r}']} dS', \quad (1)$$

where k is the wave number, S_{ill} the illuminated region, $\hat{n}(\vec{r}')$ the unit normal vector at \vec{r}' , \hat{l}_H the unit vector of the incident magnetic field. The scattered field is related to the vector potential by

$$\vec{E}_s(k, \hat{l}_t, \hat{l}_r) = j\omega \vec{A}_T(k, \hat{l}_t, \hat{l}_r) \quad (2)$$

where \vec{A}_T is the transverse component of \vec{A} along the direction \hat{l}_r . Express $k(\hat{l}_r - \hat{l}_t)$ as the 3-d position vector \vec{P} in Fourier space and $\hat{n}(\vec{r}') \times \hat{l}_H$ as the object scattering function $\vec{\Gamma}(\vec{r}')$, the vector potential becomes

$$\vec{A}(\vec{P}) = \frac{jke^{-jkR_r}}{4\pi R_r} \int_{-\infty}^{\infty} \vec{\Gamma}(\vec{r}') e^{j\vec{P} \cdot \vec{r}'} d^3\vec{r}' \quad (3)$$

where

$$\vec{\Gamma}(\vec{r}') = \begin{cases} 2\hat{n}(\vec{r}') \times \hat{l}_H & \text{on the illuminated surface} \\ 0 & \text{elsewhere} \end{cases} \quad (4)$$

If the term in front the integral is removed, the integral in Eq.(3) shows that measurement of the vector potential carried out for a sufficient range of values of \vec{P} that are realized by varying \hat{l}_r (angular diversity) and by varying k (frequency or wavelength diversity) permits accessing a finite region of the 3-d Fourier space data [8].

It is noted that the object scattering function is uniquely defined only if both the object and \hat{l}_H are fixed during the measurement interval. This condition holds only if the object and the transmitting antenna are kept stationary relative to each other while the receiving antenna is moved. If the object is rotated (as in the case of Fig.1) or the transmitter is moved (as in SAR), then the object scattering function can no longer be defined uniquely, and the 3-d

Fourier transform relation between the corrected far field and the "object scattering function" will no longer be exactly satisfied.

In spite of the ambiguity of the relationship between the scattered field and "object scattering function" as stated above, microwave images were reconstructed by Fourier transform of the corrected scattered fields. What the image represented and what the image will look like for given spectral and angular windows needed more investigation.

In the following, we will investigate the scattering mechanism of the object and the procedures of the reconstruction algorithm to interpret what the image represents and to predict what the image will look like over prescribed angular and spectral windows.

III. SCATTERING PROPERTIES OF A METALLIC OBJECT

For an object large compared to a wavelength of the incident wave, the major contributions to the scattered field are specular scattering points, edge diffraction, and multiple scattering points [10]. The properties of the above three scattering mechanisms will be briefly discussed.

1. Specular scattering points

Under the physical optics approximation, the asymptotic expression of Eq.(1) as k goes to infinity can be obtained by applying the stationary phase method [11] and the result is

$$\vec{A}(k, \hat{l}_r, \hat{l}_t) = \frac{jk}{4\pi R_r} e^{-jkR_r} \sum_j \frac{j2\pi}{k\sqrt{S_j}} 2\hat{n}(\vec{r}_j') \times \hat{l}_H e^{jk[(\hat{l}_r - \hat{l}_t) \cdot \vec{r}_j']} \quad (5)$$

where \vec{r}_j' are the vectors such that

$$\left. \frac{d[(\hat{l}_r - \hat{l}_t) \cdot \vec{r}_j']}{da'} \right|_{\vec{r}' = \vec{r}_j'} = 0, \quad (6)$$

and

$$S_j = \left. \frac{d^2[(\hat{l}_r - \hat{l}_t) \cdot \vec{r}_j']}{da'^2} \right|_{\vec{r}' = \vec{r}_j'} \quad (7)$$

where $\frac{d}{da'}$ is derivative with respect to the surface curvature. The points corresponding to the solutions of Eq.(6) are called stationary points or equiphase points or scattering centers. The absolute value of the term $\hat{n}(\vec{r}_j') \times \hat{l}_H / \sqrt{S_j}$ is called the scattering strength for those

scattering centers. It is seen that locations of the scattering centers depend on directions of \hat{l}_i and \hat{l}_r as well as the shape of the metallic surface. The scattering strength for each scattering center depends on the local properties of the scattering centers. The second derivative at the stationary point is proportional to the curvature of that point. The above analysis illustrates that the objects we would be dealing with in high frequency radar imaging are of discrete form, consisting of point scattering centers.

2. Conducting wedge with finite length

The diffracted field of a finite edge for arbitrary incidence and observation or diffraction angles has been derived [12], where the concept of equivalent electrical current and equivalent magnetic current has been applied.

Without loss of generality, consider a z-directed finite wedge with included angle $(2-n)\pi$ and edge length L as shown in Fig.2. The origin is chosen at the center of the edge. Let the x-axis be directed along the normal to the edge lying on the front face of the wedge, and the y-axis be coincident with the normal to this face, with \hat{s}' the direction of incident wave, and \hat{s} the direction of diffracted wave. The angles between the \hat{s} and \hat{s}' and the edge are θ and θ' respectively. The angle between the front face and the edge-fixed plane of incidence containing the vectors \hat{s}' and \hat{z} is ϕ' . The corresponding angle for the edge-fixed plane of observation is ϕ .

The incident field can be decomposed into TE and TM components (or parallel and perpendicular polarization) with respect to the plane of incidence while the diffracted wave can also be decomposed into TE and TM components with respect to the plane of observation. Denote the equivalent electric current and equivalent magnetic current on the edge as I and M. The expression of I and M for arbitrary incidence and observation angles has been found in [12]. For the special case of backscattering and plane conductor (i.e., $n=2$), the expression of I and M can be simplified as:

$$I = E_z^i \frac{\sqrt{\frac{\mu}{\epsilon}} (\cos \phi - 1)}{jk \sin^2 \theta \cos \phi} - H_z^i \frac{2 \cos \theta (1 + \cos \phi)}{jk \sin^2 \theta \sin \phi} \quad (8)$$

$$M = H_z^i \frac{\sqrt{\frac{\mu}{\epsilon}} (1 + \cos \phi)}{jk \sin^2 \theta \cos \phi} \quad (9)$$

where H_z^i and E_z^i are the z component of the incident fields along the edge. The scattered fields can be shown to be

$$E_\theta = \frac{j\omega\mu}{4\pi} \frac{e^{-jkr}}{r} \sin \theta \cdot I \cdot L \frac{\sin(kL \cos \theta)}{kL \cos \theta} \quad (10)$$

$$E_\phi = \sqrt{\frac{\mu}{\epsilon}} \frac{j\omega\epsilon}{4\pi} \frac{e^{-jkr}}{r} \sin \theta \cdot M \cdot L \frac{\sin(kL \cos \theta)}{kL \cos \theta} \quad (11)$$

3. Multiple reflection points

In some situations, multiple reflections become the major contributors to the scattered field. To determine the positions of the multiple reflection points, the ray optics approximation can be used. The ray should satisfy Snell's law, i.e., the angle of incidence should be equal to angle of reflection. Assume now that the multiple reflection points have been found, then the scattered field due to a set of two multiple reflection points may be approximated by

$$\vec{A}(k) = \frac{jke^{-jkr}}{4\pi R_r} \frac{j2\pi}{k\sqrt{S_2}} 2\hat{n}(\mathcal{P}_2') \times \vec{H}_2(k) e^{jk[(\hat{l}_r - \hat{r}_{21}) \cdot \mathcal{P}_2']} \quad (12)$$

where

$$\vec{H}_2(k) = \frac{\hat{r}_{21} \times \vec{A}_2(k)}{\eta} \quad (13)$$

$$\vec{A}_2(k) = \frac{jke^{-jkr_{21}}}{4\pi R_{21}} \frac{j2\pi}{k\sqrt{S_1}} 2\hat{n}(\mathcal{P}_1') \times \hat{l}_H e^{jk[(\hat{r}_{21} - \hat{l}_1) \cdot \mathcal{P}_1']} \quad (14)$$

where R_{21} is the distance between the two scattering points, \hat{r}_{21} the unit vector connecting from scattering point 1 to point 2, \mathcal{P}_2' and \mathcal{P}_1' the position vectors of the two multiple scattering points, S_1 and S_2 the second derivative at points 1 and 2 as defined in Eq.(7), and $\hat{n}(\mathcal{P}_1')$ and $\hat{n}(\mathcal{P}_2')$ the normal vectors at position \mathcal{P}_1' and \mathcal{P}_2' respectively.

IV. INTERPRETATION OF THE RECONSTRUCTED IMAGES

The reconstruction method used in microwave diversity imaging systems is either the back-projection method or the 2-d FT method. These two methods have been proven to yield equivalent results [13]. The back-projection algorithm, however, provides more physical insight to the image formation process of microwave diversity imaging. The two basic procedures in the back-projection algorithm are first to obtain filtered range profiles and second the back-projection. The Fourier transform of the frequency response with respect to

frequency will give the range profiles at that view angle. The filtered range profile is the FT of the product of the frequency response and a frequency weighting function.

The range profiles due to different scattering mechanisms can be obtained by taking the Fourier transform of the respective corrected scattered field frequency response. Because the scattered fields are measured only over a finite bandwidth and low frequency data is not available, the range profile obtained by FT of the passband data will be different from that obtained by FT of the infinite bandwidth data. The effect of passband filter will be discussed in more detail in the later section. Where the scattering centers are the major contributors, the Fourier transform of Eq.(5) with respect to frequency will give peaks at the differential ranges of the scattering centers with amplitude equal to the scattering strength. Where an edge is the major contributor, the Fourier transform of Eq.(10) and (11) will give two peaks which are at the differential ranges of the end points of the edge with an amplitude roughly proportional to $\text{sinc}(kL \cos \theta)$. Where the multiple reflection points are the major contributors, the Fourier transform of Eq.(12) will give peaks at a range equal to the differential range of the multiple scattering path. To a first order approximation, the scattered field of a complex object can be expressed as the linear superposition of the scattered field from discrete scattering centers, diffraction from the "visible" edges, and the scattered fields from any present multiple reflection points. Peaks of the range profiles, therefore, correspond to the differential ranges of the specular points, the end points of the "visible" edges, and the differential ray path length of the multiple scattering points.

Once the range profiles are known for sufficient number of object aspects, the next step is to back-project the range profiles onto each pixel of the image plane. When the object is rotated or the receiver is moved, the scattering centers will move to those points which satisfy Eq.(6) with scattering strengths given by Eq.(7). The differential ranges and the equivalent scattering strength of the end points of edges will also be changed.

The implementation of the back-projection algorithm should satisfy the following requirements [14]:

- (1). The back-projection line should contribute to those pixels which it intersects and to no others.
- (2). The contribution to the backprojection line must be proportional to the scattering strength.

- (3). The contributions to a pixel from different filtered range profiles must add 'coherently' such that the bipolar nature of the filtered range profiles is preserved.

If only the scattering centers are considered, after back-projection, the image reconstructed can be interpreted as "collections of the projected scattering centers over the angular window". To predict what the image will look like over the angular window, one can formulate the surface equations of the target, use Eq.(6) and Eq.(7) to locate the positions and calculate the scattering strength of the scattering centers for each view angle, and then use back-projection to reconstruct the images. If the surface of the object is smooth, and the incremental rotation angle is small, then the image will be "the projected outline of the scattering centers of the object over the angular window".

For an edge with finite length, its image can also be formulated through back-projection. To simplify the discussion, only the back-scattering case (i.e., when $\hat{s} = -\hat{s}'$ in Fig. 2) is considered. Let L be the length of the wedge. For a specific aspect angle, the positions of the peaks in the range profile are located at the projections of the end points along the line of sight. Amplitudes of the peaks are functions of θ and ϕ and are proportional to $\text{sinc}(kL \cos \theta)$, where θ, ϕ are defined in the edge-fixed coordinate as described in Fig.2. After back-projection, the contribution to the reconstructed image due to this view angle will be two lines. Each of these lines passes through one of the end points. When the object is continuously rotated, θ and ϕ will also be changed. The contributions to the reconstructed image due to the data of each view is two lines, except when $\theta = 90^\circ$. All the back-projection lines pass through one of the two points, which means the brightness of the end points is intensified. If the angular window contains a view so that $\theta = 90^\circ$ (the incident wave is normal to the edge), then the back-projection due to this view will produce a bright line because $L \cos \theta = 0$, and $\text{sinc}(kL \cos \theta) = 1$, and this bright line will overlap with the edge. The edge, then, will appear in the reconstructed image only if the angular window contains this view; otherwise, the reconstructed image of an edge will be only two bright points.

V. EXAMPLES

Some examples of the reconstructed images and their interpretations are given next. In the following numerical examples, the frequency coverage is from 6 GHz to 16 GHz. In the first example, we show the dependence of the image on the data acquisition geometry (monochromatic and bistatic schemes). Consider an infinite metallic cylinder with radius 20 cm. The

cylinder axis is parallel to the rotation axis. The transmitting and receiving antennas have the same linear polarization which is parallel to the axis of cylinder. The reconstructed images are obtained by rotating the target over 360° and by changing the bistatic angle of the transmitter and receiver over 360° . The scattering center of a cylinder in the monostatic case is at a point with its surface normal vector parallel to the incident wave, while the scattering center in the bistatic case is at a point with its surface normal vector parallel to the line bisecting the directions of incidence and observation. The scattering strength of the scattering center for the bistatic case is proportional to $\cos \alpha$, where α is the bistatic angle. The collection of the scattering centers is a circle for the monostatic case and is a semicircle for the bistatic case. The positions of the scattering centers on the cylinder by rotating the object (or equivalently by rotating the transmitter/receiver around the object) and by rotating the receiver only and the sketches of the back-projection for these two cases are shown in Fig.3(a) and 3(b) respectively. The numerical simulated images are shown in Fig.3(c) and 3(d).

In another example, we show the effect of the angular window on the reconstructed image. The geometry of a plate is shown in Fig.4(a). The inclination angle between the plate and the rotational axis is α . The polarizations of the transmitting and receiving antennas are right-hand circularly polarized and left-hand circularly polarized respectively, which means that the image is formed from the co-polarized scattered field. The scattered fields of the hexagonal plate are assumed to be contributed by the six edges. The images reconstructed from angular window 1 ($0^\circ, 180^\circ$), window 2 ($0^\circ, 110^\circ$), window 3 ($70^\circ, 180^\circ$), and window 4 ($0^\circ, 87^\circ$) are shown in Fig.4(b) to 4(e) respectively. In window 1, each edge becomes normal during rotation of the object to a particular incident vector, therefore, all edges appear in the image of Fig.4(b). In window 2, there is no incident vector normal to edge 1 and 4, hence these two edges disappear in Fig.4(c); but the end points have been intensified. The image of Fig.4(d) and 4(e) can be interpreted in the same manner.

In another example, we show the effect of multiple scattering on the image and the effect of different bistatic angles of data acquisition. The object consists of two parallel separated long cylinders as shown in Fig.5(a). The radius of each cylinder is 4 cm, and the distance between the two cylinders is 60 cm. Both the transmitting and receiving antennas are right-hand circularly polarized which mean that the image is formed from the cross-polarized scattered field. In this transmitting and receiving antenna system, multiple scattering phenomenon is more pronounced, because the specular reflection will be rejected by the antenna arrangement. Experimental and numerical results concerning multiple scattering on this structure has

been discussed in [15]. Series expansion solutions were used to calculate the scattered fields, and lengthy computing time is needed to generate the field data. However, under high frequency approximation, the multiple reflection points for a given set of aspect angle and bistatic angle can be found by ray optics. The detail of the derivation is given in the appendix. The differential path length versus rotation angle ϕ and the numerically reconstructed images with bistatic angle $\alpha = 0^\circ$, $\alpha = 16^\circ$, and $\alpha = 40^\circ$ are shown in Fig. 5(c),(d) and (e) respectively. For a bistatic case, there are two sets of multiple reflection points. The differential path lengths of these two sets are different and is a function of the bistatic angle, which explains the difference between these images. It is seen that multiple reflections has produced artifact in the image, that does not correspond to the physical shape of the object.

An experimental example of the reconstructed image of a complex object is given next. The test object, a metalized 100:1 scale model of a B-52 aircraft with 79 cm wing span and 68 cm long fuselage was mounted on a computer-controlled positioner situated in an anechoic chamber environment. 201 equal frequency steps covering the 6.1 to 17.5 GHz range were used to obtain the frequency response of the object. The transmitting and receiving antennas are both right-hand circularly polarized. The reconstructed image of the test object using data collected in an angular window of 90° extending from head-on to broadside in 128 looks is shown in Fig.6. The intensity or brightness of each pixel in the image is proportional to the average scattering strength of that portion over this angular window. This fact indicates that microwave diversity imaging can be applied to the study of radar cross section (RCS) management.

Over this angular window, there exist certain rotation angles such that the edges of the right wing and right tail are perpendicular to the bisection line or of the angle between the lines joining the transmitter and receiver to the rotation center of the target. However, there is no such rotation angle that the bisecting line is perpendicular to the edges of the left wing and tail. Therefore, the edges of the right wing and right tail can be seen in the reconstructed image, while the appearance of the left tail in the image shows only the end points of the edges as shown in Fig.6(b).

If the angular window is reduced to 72° from head-on as shown in Fig.6(c), the reconstructed image becomes as shown in Fig.6(d). Over this reduced angular window, there is no specular reflection from the fuselage and engines and fuel tank on the right side. This explain the difference between Fig.6(b) and 6(d). From the above experimental examples, we can

conclude that the microwave images represent the "collection of the projected scattering centers, those visible edges which are perpendicular to the bisection line, and end points of the visible edges, over the prescribed angular window".

The above examples show that the reconstructed image is dependent on the data acquisition parameters (monostatic, bistatic, polarization, frequency range, angular window) and hence care must be taken for proper interpretation of the image.

VI. ALTERNATIVE INTERPRETATION OF EDGE ENHANCEMENT PROPERTY OF MICROWAVE IMAGE

As mentioned in Sec.II and ref [2,3], the scattering object function defined is related to the geometrical shape of the object. SAR images or the images obtained by microwave diversity imaging, however, are not solid filled images, but are contoured or edge-enhanced images as illustrated in the previous examples. This property can be explained from the image formation principles described in the previous sections, however, it can also be explained from another point of view.

In SAR, in stead of the object scattering function, a target reflectivity $\rho(x, R)$ is defined in terms of the range coordinate R and cross-range coordinate x measured from the center of the synthetic aperture [9]. The effect of the finite range resolution on the nature of SAR image was discussed [9]. The range processed return with finite resolution was derived using successive integration by parts, and a conclusion was made that the finite range resolution accentuates edges of the image and eliminates portions of the image which have constant intensity over long distances. This conclusion can also be easily obtained by analyzing the scattered fields from the frequency domain over a finite bandwidth. By using the same example as in [9], the range reflectivity is shown in Fig. 7. The scattered field which is the Fourier transform of the range reflectivity can be obtained by successive differentiation of the range reflectivity with respect to range. From the fundamental Fourier transform theorem, we have the following FT pairs:

$$f(R) \longleftrightarrow F(\omega)$$

$$f'(R) \longleftrightarrow j\omega F(\omega)$$

$$f''(R) \longleftrightarrow -\omega^2 F(\omega)$$

The FT of $\delta(R - R_0)$ is $e^{-jR_0\omega}$. The FT of Fig. 7 can be easily expressed as

$$F(\omega) = a_1 \frac{e^{-jR_1\omega}}{j\omega} + a_2 \frac{e^{-jR_2\omega}}{-\omega^2} - a_3 \frac{e^{-jR_3\omega}}{-\omega^2} - a_4 \frac{e^{-jR_4\omega}}{j\omega} \quad (15)$$

where a_2 and a_3 are the slope of the segment 2 and 3 respectively. If the ratio of the highest frequency to the lowest frequency of the measurement system is not much larger than 1, then the denominator can be approximated by

$$\frac{1}{\omega} \approx \frac{1}{0.5(\omega_{\max} + \omega_{\min})} \approx \frac{1}{\omega_o} \quad (16)$$

$$\frac{1}{\omega^2} \approx \frac{1}{\omega_o^2} \quad (17)$$

The estimated target reflectivity (or range profile) will be

$$\hat{f}(R) = [a_1\delta(R-R_1) + a_2\delta(R-R_2) - a_3\delta(R-R_3) - a_4\delta(R-R_4)] * \text{sinc}\left(\frac{r}{\delta R}\right) \quad (18)$$

The above simple example and analysis show the range profile estimated from passband data accentuate the discontinuity of the reflectivity function or object scattering function. From this point view, we can also conclude that the reconstructed image represents the collection of the discontinuities of the reflectivity function over the prescribed window.

Although discontinuity of the reflectivity distribution function can be used to understand and interpret the image formation of the microwave diversity imaging, high frequency asymptotic approximation can give better understanding of the scattering mechanism. Range resolution of SAR or ISAR is usually limited by the pulse width of the transmitted signal or the bandwidth of the chirp signal. The range resolution of microwave diversity imaging is also limited by the bandwidth of the measuring system. However, under high frequency assumption, the scattered fields outside the available bands can be extrapolated and better resolutions can be achieved [16]. The applicability of extrapolations is based on the fact that the objects dealt with in high frequency radar imaging are of finite extent and discrete form, consisting of scattering centers and visible edges. Therefore, the understanding of the scattering mechanism and reconstruction algorithm is more helpful to interpret and to predict the images.

VII. CONCLUSION

The principle of image formation of microwave diversity imaging systems has been understood through investigating the scattering mechanism of the object and the procedures of the reconstruction algorithm. Some numerical and experimental results concerning the images

of a metallic object obtained by prescribed spectral and angular windows have been explained satisfactorily and predicted correctly. The edge-enhanced nature of microwave diversity imaging has been interpreted by a rather simple analysis. These successful interpretations are fundamental to research in several areas, for example, radar cross section management studies [17], target recognition. Furthermore, it gives directions to design some techniques to obscure the reconstructed images, which are the research topics under investigation.

APPENDIX

Consider two parallel identical cylinders with radius a , separated by a distance $2r_0$ seated on a rotating pedestal and illuminated by a plane wave as shown in Fig. 5(a). The cross section of that arrangement is shown in Fig. A1. The line connecting the centers of the cylinders passes through the rotating center and makes an angle θ with the respect to the rotation axis. The polar coordinates and rectangular coordinates of the points on the surfaces of these two cylinders with respect to each cylinder center are $(a, \phi_1'), (x_1', y_1')$, and $(a, \phi_2'), (x_2', y_2')$ respectively. Let the bistatic angle between the transmitter and receiver be α , the unit vectors in the direction of transmitter and receiver be \hat{i}_t and \hat{i}_r respectively. To find the stationary points of the multiple reflection, geometrical optics will be applied. The reflection law requires that the angle between the incident ray and normal line must be equal to the angle between the reflected ray and the normal line.

The stationary points of multiple reflection on the respective cylindrical surfaces for a given set of $\{r_0, a, \theta, \alpha\}$ are to be determined. Assume the incident ray first hit the cylinder 2, reflects to cylinder 1, and then bounces back to the receiver as shown in Fig. A1(a). The notation of the angles $\xi, \psi_1, \psi_2, \alpha, \theta, \phi_1', \phi_2'$ are defined in Fig. A1(a). It can be shown the following relationship must be satisfied in order to satisfy the reflection law.

$$\frac{2r_0 \sin \theta - a [\cos(\phi_2' - \alpha/2) + \sin \phi_2']}{2r_0 \cos \theta + a [\sin(\phi_2' - \alpha/2) - \cos \phi_2']} = -\cot(2\phi_2' - \alpha/2) \quad (A.1)$$

$$\phi_1' = \phi_2' - 90^\circ - \alpha/2 \quad (A.2)$$

where ϕ_2' is restricted to be

$$270^\circ \leq \phi_2' \leq 360^\circ \quad \text{when} \quad -90^\circ \leq \theta \leq 90^\circ$$

$$180^\circ \leq \phi_2' \leq 270^\circ \quad \text{when} \quad 90^\circ \leq \theta \leq 270^\circ$$

For a given set of parameters $\{r_0, a, \theta, \alpha\}$, the azimuth angle ϕ_2' and therefore ϕ_1' can be

determined by solving Eq.(A.1) and (A.2).

The other case is that the incident ray first hit cylinder 1, reflect to cylinder 2, and then bounce back to the receiver. The geometry of this situation is shown in Fig.A1(b). The stationary points must satisfy the following relationship

$$\phi_1'' = \phi_2'' - 90^\circ + \alpha/2 \quad (A.3)$$

$$\frac{2r_0 \sin \theta - a [\cos(\phi_2'' + \alpha/2) + \sin \phi_2'']}{2r_0 \cos \theta + a [\sin(\phi_2'' + \alpha/2) - \cos \phi_2'']} = -\cot(2\phi_2'' + \alpha/2) \quad (A.4)$$

From the above derivation, it can be seen that there are two pairs of multiple reflection points for bistatic system and only one multiple reflection points for monostatic case.

ACKNOWLEDGEMENT

The work was supported by grants from the Army Research Office, the Air Force of Scientific Research, RCA and GE Corporation.

REFERENCE

- [1] R. M. Lewis, "Physical Optics Inverse Diffraction", *IEEE Trans. on Ant and Prop.*, vol. AP-17, pp. 308-314, 1969.
- [2] N. Bojarski, "Inverse Scattering", Final Rep. N000-19-73-C-0312F, Nav. Air Syst. Command, Warminster, Pa., Feb. 1974
- [3] M. Bestero, "The Stability of Inverse Problems," Chap. 5 of *Inverse Scattering Problems in Optics*, edited by H.P. Baltes, Springer-Verlag, Berlin, 1980.
- [4] K. Tomiyasu, "Tutorial Review of Synthetic Aperture Radar (SAR) with Application to Imaging of Ocean Surface," *Proc. IEEE*, vol. 66, pp. 563-583, 1978.
- [5] B. D. Steinberg, *Microwave Imaging with Large Antenna Arrays*, John Wiley and Sons, New York, 1983
- [6] G. Tricoles, N. H. Farhat, "Microwave Holography: Applications and Techniques," *Proc. of the IEEE*, Vol. 65, No. 1, pp.108-121, 1977.
- [7] C. K. Chan and N. H. Farhat, "Frequency Swept Tomographic Imaging of Three-dimensional Perfectly Conducting Objects," *IEEE Trans. Ant and Prop.*, vol. AP-29, pp. 312-319, 1981
- [8] N. H. Farhat, C. L. Werner and T. H. Chu, "Prospect for Three-Dimensional Projective and Tomographic Imaging Radar Networks", *Radio Science*, vol. 19, No. 5, pp. 1347-1355, 1984
- [9] M. R. Wholers, S. Hsiao, J. Mendelsohn, G. Garner, "Computer Simulation of Synthetic Aperture Radar Imaging of Three-Dimensional Objects," *IEEE Trans. on Aerospace and Electronic Systems*, vol. AES-16, pp. 258-271, 1980.
- [10] Ruck, Barrick, Staurart, and Kirchbaum, *Radar Cross Section Handbook*, Plenum Press, New York, 1970.
- [11] Jon Mathews and R. L. Walker, *Mathematical Methods of Physics*, 2nd Ed., W. A. Benjamin, Inc., Menlo Park, California, 1970
- [12] Arie Michaeli, "Equivalent Edge Current for Arbitrary Aspects of Observation", *IEEE trans. Ant and Prop.*, vol. AP-32, No. 3, pp. 252-258, 1984
- [13] Stanley R. Deans, "The Radon Transform and Some of its Applications," John Wiley & Sons, New York, 1983
- [14] Gabor T. Herman, *Image Reconstruction from Projections*, Academic Press, New York, 1980
- [15] T. H. Chu, N. H. Farhat, "Multiple Scattering Effects in Microwave Diversity Imaging," *IEEE Antennas and Propagation International Symposium*, AP-S 1986; pp. 69-72.
- [16] Hsueh-Jyh Li, N. H. Farhat, and Y. Shen, "A new Iterative Algorithm for Extrapolation to Radar Imaging," submitted to *IEEE Trans. AP* for publication.
- [17] N. H. Farhat, H. J. Li, Y. Shen, "Radar Cross Section Management Studies Employing Microwave Diversity Imaging," 1986 National Radio Science Meeting, Philadelphia, pp. 100, June 8-13, 1986.

FIGURE CAPTION

Fig 1. A simplified microwave diversity imaging arrangement

Fig.2 Geometry of a finite wedge diffraction problem

Fig.3 Positions of the scattering centers of a cylinder and the sketch of back-projection for the case of (a). rotating the transmitter/receiver; and (b). rotating the receiver only; over 360° .
(c). the numerically reconstructed image of (a);
(d). the numerically reconstructed image of (b).

Fig.4 (a). Geometry of a hexagonal plate and the measurement arrangement. Image reconstructed from different angular windows:
(b). window 1 (0° , 180°), (c). window 2 (0° , 110°),
(d). window 3 (70° , 180°), (e). window 5 (0° , 87°).

Fig.5 (a). A dual-cylinder object,
and plots of the its numerically calculated differential range of multiple reflection path versus rotation angle and simulated images obtained by using different bi-static angle equal to
(b). 0° , (c). 16° , (d). 40° .

Fig.6 (a). Sketch of a B-52 test object airplane and the angular window.
(b). Reconstructed image of (a).
(c). Reconstructed image of (c).

Fig.7 An example of target range reflectivity together with its successive differentials.

Fig.A1 Multiple reflections of a two-cylinder object.

- (a). The incident wave reaches the left cylinder first, and is then reflected back by the right cylinder.
- (b). The incident wave reaches the right cylinder first and is then reflected back by the left cylinder.

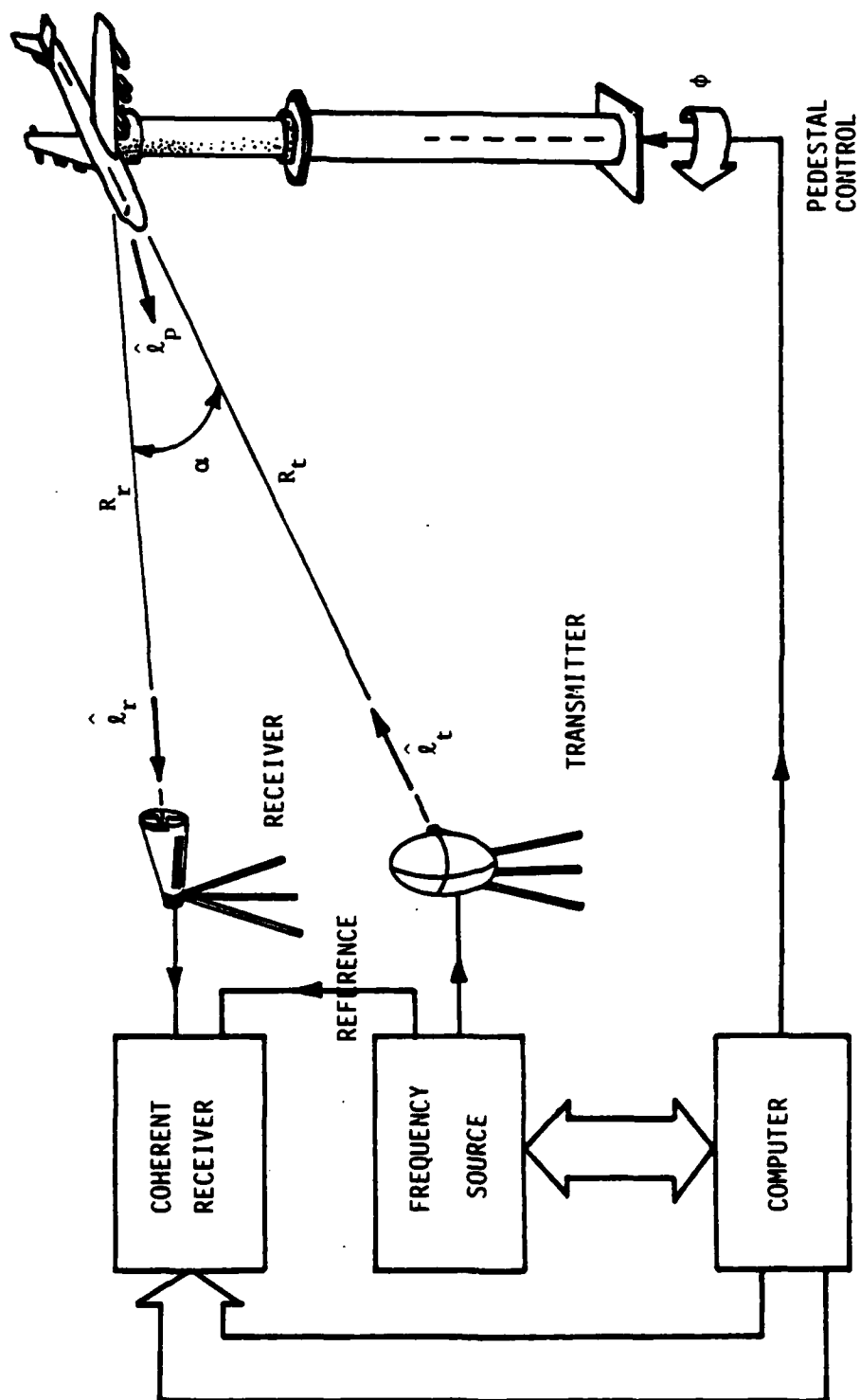


Fig 1. A simplified microwave diversity imaging arrangement

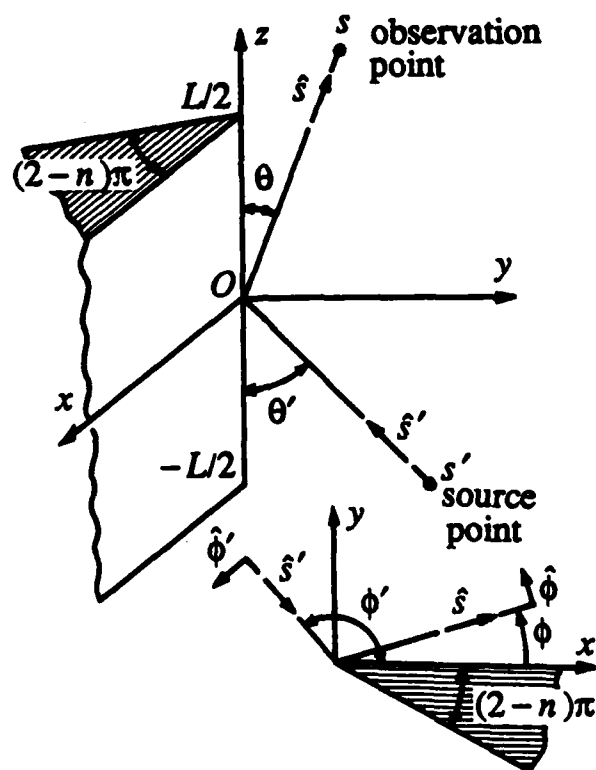
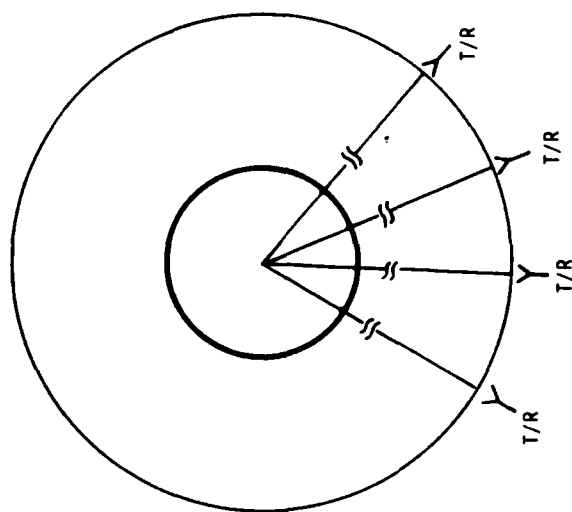


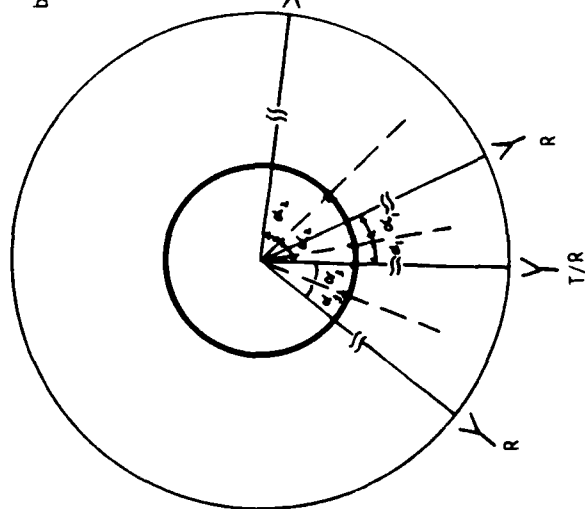
Fig. 2 Geometry of a finite wedge diffraction problem.

ROTATING OBJECT
(or rotating T/R)

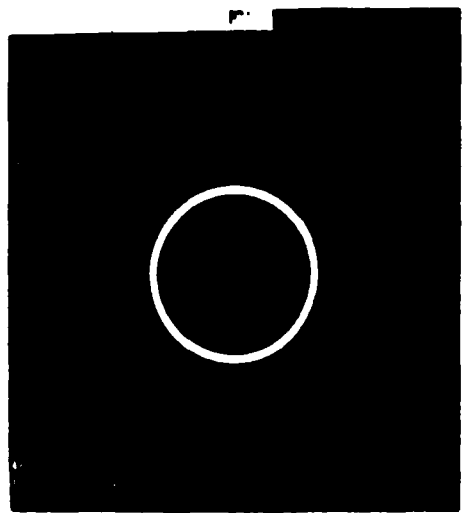


(a)

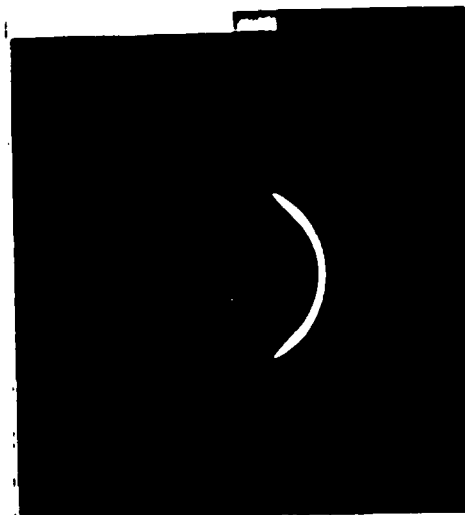
bistatic diversity



(b)



(c)



(d)

Fig.3. Positions of the scattering centers of a cylinder and the sketch of back-projection for the case of (a). rotating the transmitter/receiver; and (b). rotating the receiver only; over 360° . (c). the numerically reconstructed image of (a) and (d). the numerically reconstructed image of (b).

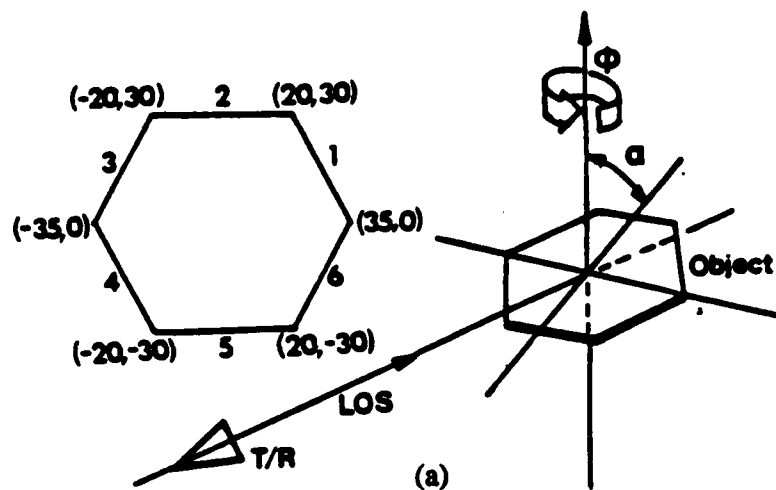


Fig.4 (a). Geometry of a hexagonal plate and the measurement arrangement.
 Image reconstructed from different angular windows:
 (b). window 1 (0° , 180°), (c). window 2 (0° , 110°),
 (d). window 3 (70° , 180°), (e). window 5 (0° , 87°).

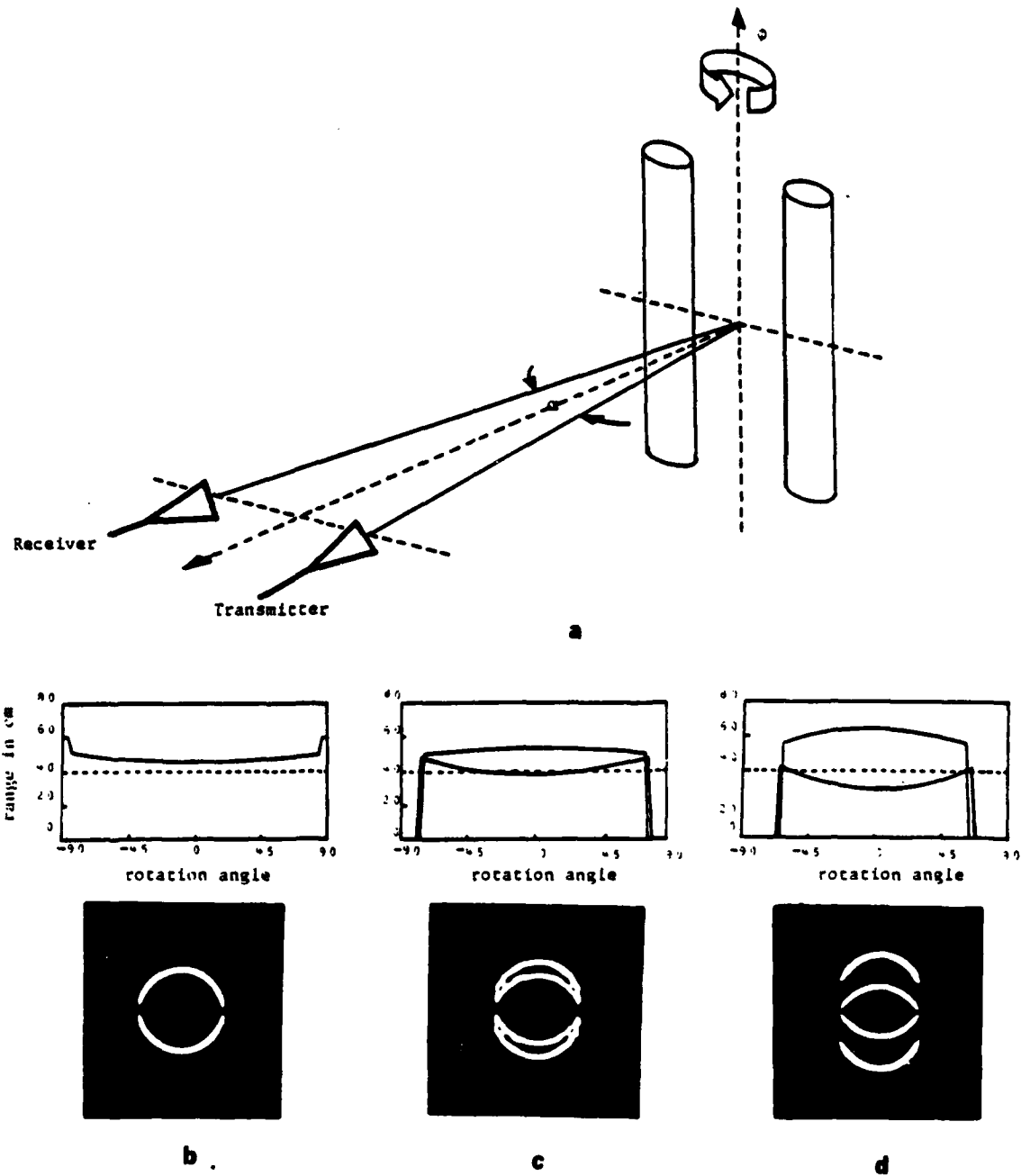
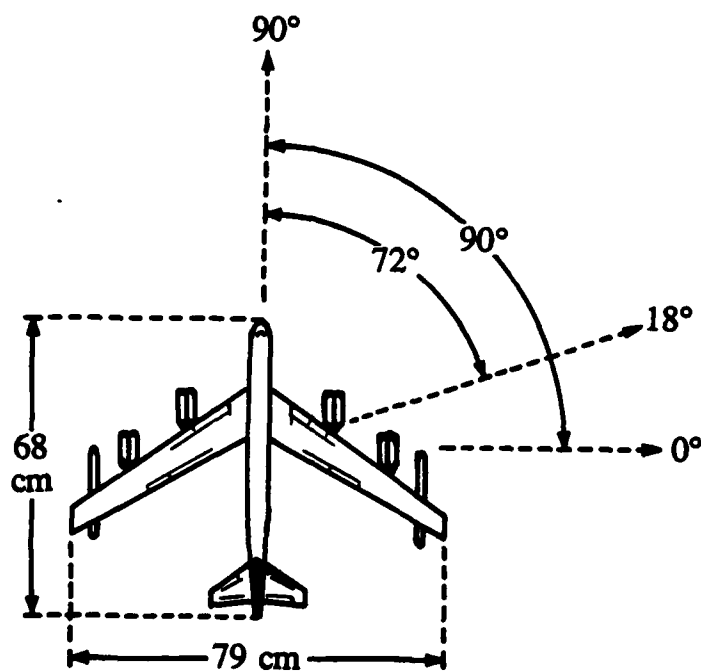


Fig.5 (a). Imaging geometry of a dual-cylinder object. Plots of the numerically calculated differential range of multiple reflection path versus rotation angle and simulated images obtained by using different bistatic angles equal to (b). 0° , (c). 16° , (d). 40° .



(a)



(b)



(c)

Fig.6 (a). Sketch of a B-52 test object airplane and the angular window.
 (b). Reconstructed image over the angular window (0° to 90°)
 (c). Reconstructed image over the angular window (18° to 90°).

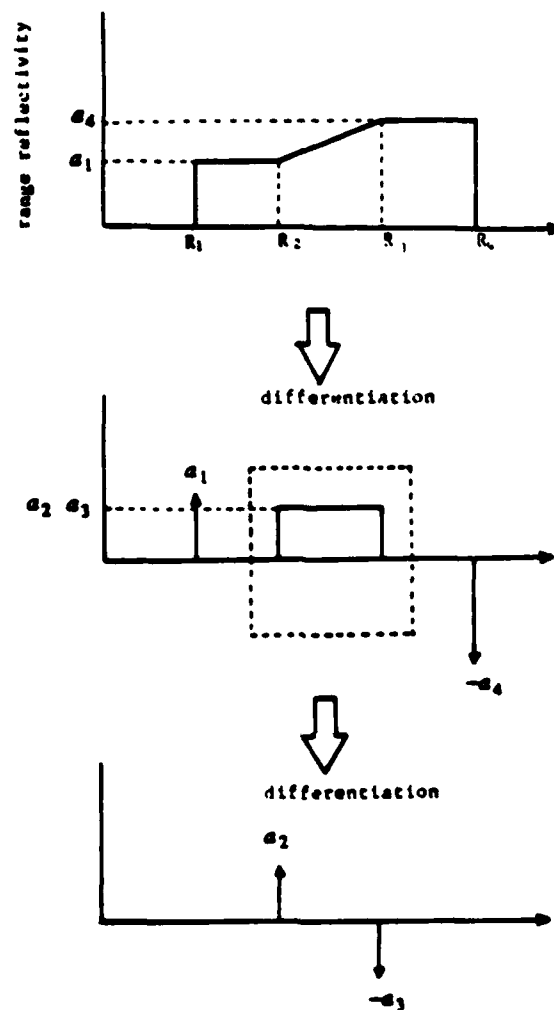


Fig. 7 An example of target range reflectivity together with its successive differentials.

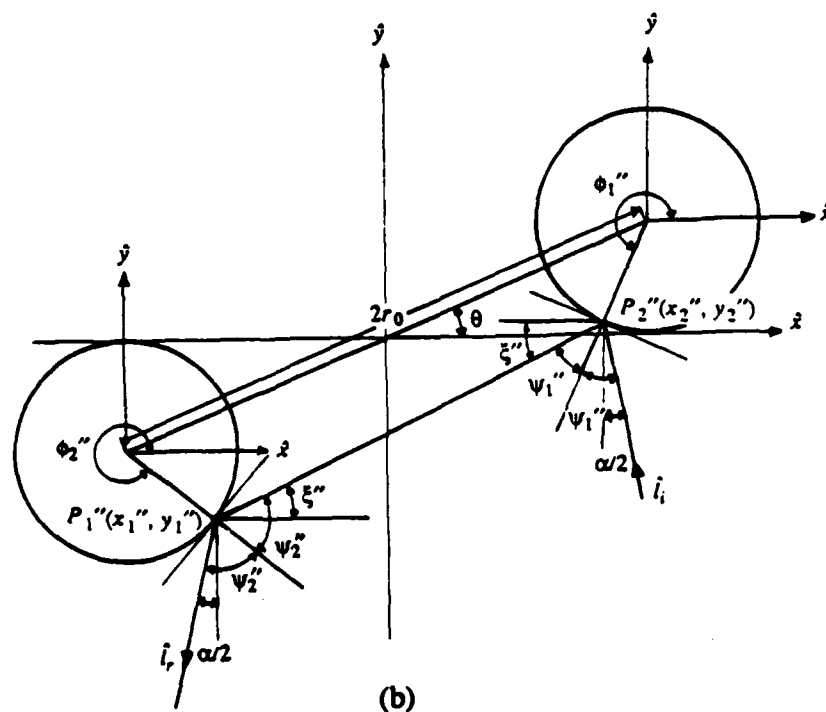
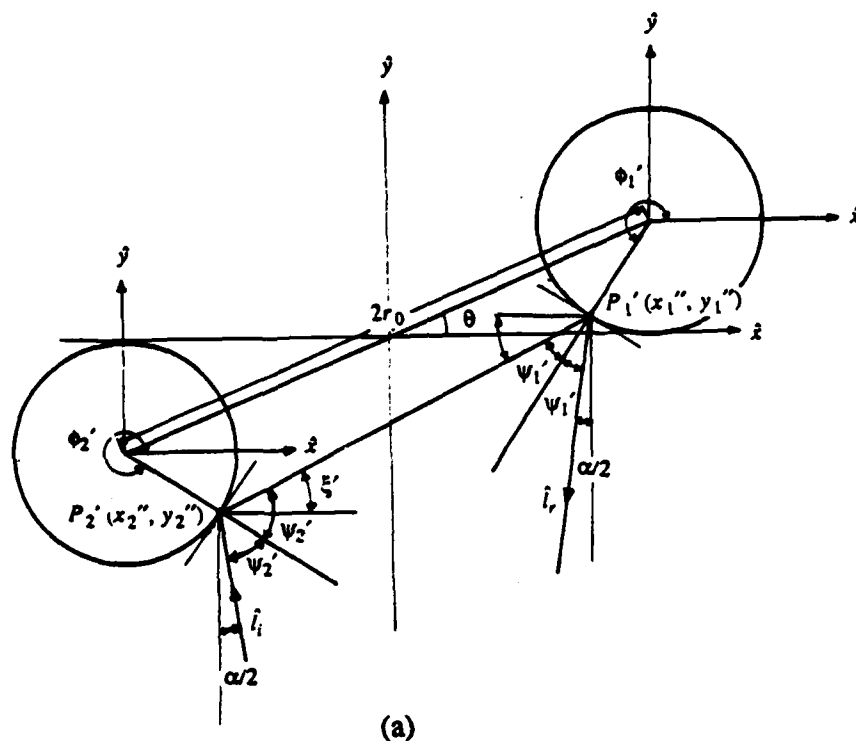


Fig.A1 Multiple reflections of a two-cylinder object. (a). The incident wave reaches the left cylinder first, and is then reflected back by the right cylinder. (b). The incident wave reaches the right cylinder first and is then reflected back by the left cylinder.

Appendix II

RADAR CROSS SECTION MANAGEMENT STUDIES EMPLOYING MICROWAVE DIVERSITY IMAGING

Hsueh-Jyh Li, Nabil H. Farhat, Yuhsyen Shen

The Moore School of Electrical Engineering
University of Pennsylvania
Philadelphia, PA. 19104

I. INTRODUCTION

Radar cross section (RCS) is a measure of the equivalent size of a target as seen by the radar [1]. RCS is a function of aspect angle, frequency, and polarization. For certain applications, it is desirable to enhance the RCS over some specific range of aspect angles. For example, strong return signals are required to track a missile or an aircraft in flight. In contrast, for other applications it is often desirable to reduce or minimize the RCS over specified spectral and angular windows so the target is less likely to be detected.

RCS management is a general term for obtaining the RCS of a scattering object by manipulating the distribution and strengths of the hot spots or flare spots of a target over prescribed spectral and angular windows and states of polarization. Hot spots represent all those areas that have major contributions to the received scattered fields. There are several ways to determine the site of hot spots [2]. An experienced engineer can roughly point out the possible locations of the hot spots; a computer code can be used to estimate the locations of the scattering centers and their scattering if the equations that describe the surface of the object can be formulated. However, all such estimates need experimental verification.

Microwave diversity imaging systems using angular, wavelength, and polarization diversity have been used to obtain images of metallic objects with nearly optical resolution [3]. The pixel intensity or brightness of the reconstructed image is proportional to the mean scattering strength at the corresponding position averaged over the specified angular window and spectral window. This fact suggests microwave diversity imaging can be employed to determine the hot spots and to study RCS management.

Two steps are usually involved in the study of RCS management. First the hot spots must be identified. Certain techniques are then utilized to manipulate the hot spots. Fine resolution of object detail in the reconstructed image is essential for locating the hot spots of an object over the prescribed spectral and angular windows and the given states of polarization of the transmitter and receiver. The range resolution of a frequency diversity imaging system is proportional to the bandwidth of the measurement system. If the bandwidth is too narrow to give acceptable resolution, the algorithm for the extrapolation of data available in multiple restricted bands or in a single narrow band developed in [4] can be applied to locate the hot spots.

Previously, radar workers usually treated the RCS from the detection perspective. Therefore, techniques of reducing RCS were developed to reduce the signal to noise ratio (S/N) so that the target can more easily elude detection from radar. However, as will be shown later a low S/N is not a sufficient criterion for eluding detection when microwave diversity imaging systems are employed where signals from many broadband sensors are combined to form an image. In this paper we will consider therefore the RCS management from the imaging point of view, that is, we consider principles and techniques for making the image unrecognizable by radar.

In Sec. II image formation in microwave diversity imaging will be summarized. A new term, "diaphanization", will be introduced in Sec. III. We will also describe how to use microwave diversity imaging to diaphanize an object in that section. Effects of Gaussian noise on the reconstructed image will be discussed in Sec. IV. Some fundamental concepts for obscuring the image will be proposed in Sec. V. Experimental results on different diaphanization techniques will be given in Sec. VI.

II. IMAGE FORMATION IN MICROWAVE DIVERSITY IMAGING

The simplified microwave diversity imaging arrangement is shown in Fig.1. A metallic object seated on a rotated pedestal is illuminated by a plane wave. For each aspect angle a set of pulses at different frequencies are transmitted and their echoes are received. The object is then rotated and the measurement is repeated to obtain the multiaspect stepped frequency

response of the scattering object. Analysis of microwave diversity imaging has been discussed in [5].

The reconstruction method used in microwave diversity imaging systems is either the back-projection method or the 2-d FT method. These two methods have been proven to yield equivalent results[6]. The back-projection algorithm, however, provides more physical insight into the image formation process in microwave diversity imaging [12]. The two basic procedures in the back-projection algorithm are first obtaining filtered range profiles and then back-projecting the range profiles onto each pixel of an image plane. The range profile of a given aspect is obtained by Fourier transforming the frequency response at that viewing angle while the filtered range profile is the FT of the product of the frequency response and an appropriate frequency weighting function.

At high frequencies the major contributions to the scattered field of a complex shaped metallic object are specular scattering points, edge diffractions, multiple reflection points, creeping waves, and surface traveling waves [7]. Properties of the range profile for each scattering mechanism has been discussed in [5]. Locations of peaks in a range profile reflect the differential ranges of specular points, end points of the "visible" edges, differential ray path length covering the multiple reflection points, and / or the ray path length of the creeping waves and surface traveling waves.

Once the range profile for each aspect angle is determined, the next step is to back-project the range profile onto each pixel. If we only consider the scattering centers, then after back-projection, the reconstructed image can be interpreted as *the projected outline of the specular points of the object for the prescribed angular window*, which usually reflects the projective outline of the visible portions of the object shape. If an edge with finite length is involved, the microwave image of an edge will be two bright points whose locations correspond to the end points of the edge unless the normal aspect (i.e., incident wave is normal to the edge) is included in the angular window; only then will an edge appear in the image [5].

III. DIAPHANIZATION

According to the Webster dictionary, "diaphanous" means:

1. so fine or gauzy in texture as to be transparent or translucent
2. vague or indistinctive, airy.

Accordingly, we introduce a new term "diaphanization", which can be used to describe:

1. All techniques of reducing RCS in order to render a target invisible to radar detection.
2. All techniques of obscuring the image so that the image is vague, indistinctive or not recognizable by an imaging radar

Therefore, diaphanization is a technique which will influence either detection or image formation and recognition.

From the detection perspective, diaphanization will generally lower the target's signal to noise ratio (S/N), thus decreasing the likelihood of detection [1]. Therefore, it is desirable to minimize the RCS. From the imaging point of view, however, low S/N is not a fatal problem for microwave diversity imaging systems. It will be shown later that microwave diversity imaging is very robust to Gaussian noise, even though the noise is stronger than the signal. Therefore, techniques that distort the reconstructed image to make it unrecognizable should be considered. In the following, we will demonstrate how to apply microwave diversity imaging to diaphanize an object and to explain the motivation for studying image distortion.

The procedure of utilizing microwave diversity imaging to diaphanize a target for prescribed spectral and angular windows is as follows:

1. Obtain the image of the target before diaphanization.
2. Identify the hot spots which are the bright portions in the image.
3. Use certain techniques to diaphanize the object, i.e. to minimize reflection from the hot spots.
4. Obtain the image of the target following diaphanization.

5. Compare the images before and after diaphanization.

Techniques of reducing the RCS can be grouped into three classes [7]: covering the object with absorbing material or substituting metallic parts with resistive or composite material; shaping the target; and impedance loading. The first method is based on absorption of the incident radiation. The second method is based on redirecting the incident waves, i.e., scattering the incident illumination into as wide a solid angle as possible or into a direction away from the probing system. The third method, also known as passive cancellation, is based upon the concept to introduce an echo source whose amplitude and phase can be adjusted to cancel another echo source [7]. In this paper, we will give examples showing how microwave diversity imaging is used in RCS management and diaphanization studies of a complex object.

In the following experimental example, 201 equal frequency steps covering the 6.0 to 17.5 GHz range were used to obtain the frequency response of the object for different aspect angles. The magnitude of the scattered fields are measured relative to a reference cylinder. The RCS defined in this paper is the square of the measured relative field and therefore the unit of RCS is a relative level but not an absolute value. Co-polarized waves refer to the waves created when both transmitting and receiving antennas have the same sense of circular polarization; while cross-polarized waves are the waves created when the transmitting antenna and receiving antenna have an opposite sense of circular polarization.

The test object, a metalized 1:100 scale model of a B-52 airplane with 79 cm wing span and 68 cm long fuselage was mounted on a computer-controlled positioner situated in an anechoic chamber environment. A sketch of the B-52 and the reconstructed image using data collected in an angular window of 90° extending from head-on to broadside in 128 looks with cross-polarized waves are shown in Figs. 2(a) and (b) respectively. The intensity or brightness of each pixel is proportional to the average scattering strength of that portion over the angular and spectral windows.

The bright spots are the hot spots of the target. To reduce the RCS, we cover the hot spots with broad-band absorbers (Emerson and Cumming AN-72). Portions of the B-52 model covered with broad-band absorber are indicated by the dark lines in the sketch of Fig. 2(c).

These parts consists of the right hand sides of the fuselage, all edges of the right wing, and the right sides of the two right engines and fuel tank. The RCS of an object is usually reduced after diaphanization, but it is not reduced for every frequency because the scattered field is a result of interference and is a function of frequency. Therefore, it is not proper to measure the effectiveness of a diaphanization on RCS at a specific frequency if a prescribed spectral range is of interest. We have adopted a more reasonable measure — that of comparing the mean scattered fields before and after diaphanization. The mean RCS is obtained by averaging the RCS at each frequency over the prescribed spectral window for a given aspect angle. The mean RCS versus aspect angle before and after diaphanization using cross-polarized waves are shown in Figs. 2(d). From these plots, we find that the RCS has been reduced for most aspect angles. The reconstructed image after diaphanization are shown in Figs. 2(e). The images before and after diaphanization have the same dynamic display range. One can see that diaphanization reduces the brightness of the hot spots. However, if we lower the dynamic display range of the post diaphanization image, the image becomes as shown in Figs. 2(f). Clearly, the nature of the target is still recognizable. From a detection point of view, covering the hot spot portions did reduce the RCS. However, from the imaging perspective, the image is still recognizable.

IV. EFFECT OF GAUSSIAN NOISE ON THE RECONSTRUCTED IMAGE

It is known that low signal to noise ratio (S/N) will decrease detection probability and increase the false alarm rate [1]. For a practical radar detection system, S/N above 15 db is usually required. It is also known that coherent summation will produce coherent gain or superposition gain. That is, if signals contaminated by Gaussian noise are coherently summed n times, the resultant S/N will increase n times [1]. The reconstruction algorithm of microwave diversity imaging involves obtaining the filtered range profiles and back-projecting them in the image plane [12]. Both procedures involve coherent summations and hence result in coherent gain. Therefore, the robustness of microwave diversity imaging to Gaussian noise is expected.

Microwave diversity imaging usually uses stepped frequency response measurement. For each frequency step, the bandwidth of the receiver is kept the same. The standard deviation of the Gaussian noise at each frequency step is therefore the same.

Under the high frequency approximation, at a specific aspect the field scattered from a metallic object can be expressed as the superposition of the scattered fields of N discrete scattering centers [4] such that the scalar fields at frequency f_m is given by

$$E_s(f_m) = \sum_{i=1}^N a_i \exp(j2\pi f_m r_i) \quad f_1 \leq f_m \leq f_2 \quad (1)$$

where a_i is the scattering strength of the i -th scattering center, r_i is the differential range of the i -th scattering center with respect to the reference point, f_1 and f_2 are the lowest and highest frequencies of the measurement system respectively, N_p is the number of frequency points. Assume the noise power level of the receiver at each frequency step is N , then the S/N due to the i -th point scatter is $|a_i|^2 / N$. Assume the point scatterers are well separated apart so that at range r_i the contributions due to the side-lobe of other scatterers can be neglected. The signal (sampled value at r_i in the FT domain or range profile) to noise ratio will become $N_p |a_i|^2 / N$ since the Fourier transform is a process of coherent summation. Therefore N_p is the coherent gain or superposition gain for this example.

Back-projection is a process of coherent summation of the contributions of the back-projection lines obtained from the filtered range profile of each aspect angle at each image plane pixel. This additional coherent process will make the reconstructed image more robust to the Gaussian noise. If the object consists of isotropic point scatterers, i.e., the scattered fields of these point scatterers are isotropically distributed, then the overall coherent gain will be $N_a N_p$ if data from N_a aspect angles are used to reconstruct the image. In practice for a metallic object for example, the locations and scattering strengths of the scattering centers and end points of edges will change or migrate when the object changes aspect (rotation) during data acquisition. Therefore, the signal (image intensity at a pixel) to noise ratio in the image space cannot be expressed in the above simple form.

The following example illustrates the effect of Gaussian noise on the reconstructed image.

Figure. 3(a) shows the mean RCS after diaphanization of the B-52 scale model versus aspect angle. We used the computer to generate Gaussian noise with two levels N_1 and N_2 (see Fig.3(a)) and add those to the measured fields to get two sets of noisy data. The corresponding S/N levels of N_1 and N_2 are about 3 dB and -2 dB respectively relative to the mean RCS. The frequency response of the first aspect angle (broadside view) without and with noise levels N_1 and N_2 are shown in Figs. 3(b), (c), and (d) respectively. The range profiles corresponding to the data in Figs. 3(b), (c), and (d) are shown in Figs. 3(e), (f), and (g) respectively. If we stack the range profiles of the first 64 view angles together in a perspective representation, the range profiles without and with the two levels of Gaussian noise will appear as shown in Figs. 3(h), (i), and (j). The images reconstructed from these three sets of range profiles are shown in Figs. 3(k), (m) and (n) respectively. The results presented in Fig. 3 show clearly that Gaussian noise affects the frequency response most, the range profile less, and the reconstructed image least because of coherent or superposition gain.

V. FUNDAMENTAL CONCEPTS FOR DISTORTING IMAGES

From the above examples, it can be seen that low S/N or strong Gaussian noise is not a sufficient criterion for totally obscuring the images. In order to develop techniques for making the image unintelligible or obscured, one must resort to understanding of the scattering mechanism and the reconstruction algorithm involved.

Radiation can originate from several locations on a scatterer. These include excitation regions, impedance loads, sharp bends, and open ends [8]. The finite passband data and finite range resolution make the range profile accentuate the discontinuities in reflectivity function, and the image can be interpreted as a *collection of the discontinuities of reflectivity function* [5]. The reconstruction algorithm followed by include steps: obtaining filtered range profiles followed by back-projection. Both steps as pointed out earlier are coherent summation processes. Based on these observations we will propose some fundamental concepts or rules for obscuring the image.

1. **Creation of artificial discontinuities:** The image is a collection of the discontinuities of the reflectivity function. For a set of given objects, their images can be obtained and

stored to act as the data base for subsequent recognition purpose. If unexpected discontinuities were created, the reconstructed images of the target will be different from their original ones. In that case, visual recognition will be more difficult or may fail.

2. **Creation of multiple reflections:** Locations of peaks in the range profile due to multiple reflections correspond to the differential ray path between the multiple scattering points on the object. Such peaks correspond to as physical detail on the object and help therefore to distort and obscure information about object. If the object is shaped so that multiple reflections are deliberately produced to be the dominant contributions to the scattered fields, then the image might be obscured or distorted.
3. **Manipulation of local reflectivity:** Here we can make the reflectivity at a given point a function of aspect angle and frequency or randomly modulate it in time. The contributions to a pixel from different filtered range profiles obtained at different aspect angles are added coherently. If the reflectivities of a point obtained at different aspect angles have the same phase, that image point will be intensified after back-projection. If the phase of reflectivity at that point is randomly varied for each frequency and aspect angle, the range profile might produce random peaks and the peaks in the range profile corresponding to those reflection points might become smaller because their reflectivities at each frequency is not in phase. After back-projection, the intensity at that image point might become smaller and the image might be contaminated by random noise.

Based on the above ideas, we will describe next a study of some diaphanization techniques which might be useful in reducing the RCS or obscure the images and make them intelligible.

VI. EFFECT OF DIAPHANIZATION TECHNIQUES ON RCS AND IMAGING

Some techniques for reducing RCS have been extensively analyzed in [7], which include covering the body with absorbing layers, shaping the body, and impedance loading. In the following, we will use microwave diversity imaging as a new tool to experimentally and numerically study the effect of these techniques on RCS and imaging.

6.1 Covering With Absorbers

Microwave absorbers can be divided into four groups [9]: magnetic material absorbers, resonant absorbers, broad-band absorbers, and surface current absorbers. To reduce the RCS over a broad spectral bandwidth, broad-band absorbers are preferred. However, broad-band absorbers available today are not suitable for aerodynamic or spacedynamic applications because they usually consist of light foam material. Nevertheless, broadband absorbers can be a useful tool in experimental study the effect of diaphanization on RCS and imaging in the context of the work reported here.

Shown in Fig.4(a) and (b) are the arrangement for measuring the scattered field of a square conducting plate (40 x 40 cm) and the mean RCS using co-polarized waves before and after diaphanization plotted against rotation angle ϕ with zero degrees taken as the broadside direction. Both faces of the plate were covered with an Emerson and Cumming Eccosorb AN72; the spectral sampling range of the received fields consists as before of 201 frequency points spanning the spectral window (6 to 17.5 GHz). The mean RCS after diaphanization is seen to have been reduced for low rotation angles, and the amount of reduction decreases as the rotation angle increases. However, the mean RCS after diaphanization are greater than those before diaphanization when the rotation angle ϕ is greater than 60° . This simple experiment illustrates that the use of broad-band absorber does not guarantee the mean RCS reduction for all aspect angle.

The reconstructed projective images of the plate before and after diaphanization are shown in Fig.4(c) and (d) respectively. The dynamic display ranges of the two images shown are different with that in (d) being lower than in (c). From the above example together with the example shown in Fig.2, one can see that diaphanization using a broad-band absorber to cover hot spots is generally not very effective in obscuring the image.

6.2 Target Shaping

As one of the methods of RCS reduction, the aim of target shaping is to redirect the incident radiation away from the probing system. As a method of distorting the image, target shaping can also be a technique of generating multiple reflections or creating unexpected

discontinuities or reflections. Multiple reflections will distort and degrade the image and unexpected reflection can decoy the image.

A good example of target shaping is the B-1 aircraft, which is designed to have little specular reflection over practically encountered angular window. A 1:100 scale model B-1 was mounted on a rotating pedestal with inclination angle 20° as shown in Fig.5(a). The reconstructed images with an angular window extending from head-on to tail-on ($-90^\circ, 90^\circ$) of the co-polarized and cross-polarized echoes are shown in Fig. 5(b) and 5(c) respectively.

An important feature of an image is its edges. The microwave image of an edge is either two points or a line depending on the angular window available [5]. If the circumference of the edge is covered or painted with resistive materials with serrated edges, the range profiles will be distorted and will contain more peaks due to arising reflections from added discontinuities. It is expected that the reconstructed image will be different than from that obtained without artificial discontinuities. To illustrate this a conducting plate ($40\text{ cm} \times 40\text{ cm}$) is covered with ceramic substrates as shown in the pictorial view of Fig. 6(a). The dielectric constant of the substrate is about 10 and the thickness is 25 mils. The plate was mounted on the pedestal with an inclination angle θ of about 30° as shown in Fig.6(b). The averaged back-scattered fields of the plate without and with the ceramic substrate covering are shown in Fig. 6(c). The reconstructed images of the plate with and without the substrate using angular windows ($-30^\circ, 60^\circ$) and ($5^\circ, 60^\circ$) are shown in Figs. 6(d) to (g) respectively. The bright portion in the center part of the plate image is due to secondary reflections from the support holder in the presence of the plate and cannot be subtracted effectively during calibration. Figure 6(d) does not look much different from Fig.6(e). The negligible difference is a result of the brightness of the edges, to which the fields of those angles close to 0° (broad-side) contribute. The difference between Fig. 6(f) and Fig. 6(g) is more discernible. Both of these images were reconstructed from an angular window excluding those views close to the broadside. The image of the plate has been decoyed successfully by the presence of the substrate covering for certain view angles. Visual analysis of the image might accordingly be confused and produce a wrong identification.

Unfortunately, obscuring the image in this fashion causes an increase of the RCS due to the extra reflections.

6.3 Impedance Loading

The effect of linear impedance loading on back-scattering from a conducting object has been extensively studied. An N-port loaded scatterer can be represented by a general network diagram [10]. The back-scattered field could be maximized, minimized or nullified by lumped impedance loading. The required loading, however, is highly dependent on frequency, loading positions, number of loading points and aspect angles [2]. Therefore, fixed linear impedance loading is not an effective means for reducing RCS over a broad spectral range. However, to study the effect of linear loading on the image, a straight wire scatterer with linear impedance loading is used as the object, and the moment method is used to numerically analyze the desired properties. The back-scattered field of a thin wire scatterer with and without impedance loading were numerically calculated. Shown in Fig. 7(a) is the geometry of a wire scatterer with seven symmetrically spaced impedance loading points. The locations of the loading points are shown in the figure. The overall length is 30 cm, and the radius to length ratio is 1/100. The spectral window used is from 6 to 16 GHz. In short, the length of the wire in terms of wavelength ranges from 6 to 16. The impedance at each loading point is confined to 50 Ω . The parameters above are arbitrarily chosen. The complex frequency response of the wire without and with impedance loading are shown in the Fourier slices [3] of Fig. 7(b) and 7(e). The radial distance of a given point in these plots represents the operating frequency, while the polar angle represents the angle of incidence θ in Fig. 7(a). The brightness of each point is proportional to the amplitude of the frequency response. The reconstructed images of the wire scatterer without and with loading using angular windows ($20^\circ \leq \theta \leq 90^\circ$) and ($20^\circ \leq \theta \leq 84^\circ$) with θ defined in Fig. 7(a) are shown in Figs. 7(c), (d) and (f), (g). It is interesting to note that a ring with a radius equal to half the length of the wire appears in the reconstructed images shown in Figs. 7(c) and (d). This is due to the waves traveling from one end point to the other end point of the wire[11]. The image of the wire with impedance loading (see Fig. 7(d)) differs notably from that without loading (see Fig. 7(g)). The image is seen

to be blurred. The loading points cause discontinuities that reradiate strongly. The reflection coefficient of a certain loading point is different for each frequency and each aspect angle, and each loading point will cause additional traveling waves or cause additional reflections. This makes the image of a loading point not only a point but instead a sweeping curve.

The phenomenon of traveling waves along the wire is very pronounced because the currents are confined to flow in one direction only, and the physical optics can not be applied in this structure. The image of a wire scatterer is therefore not expected to reflect its shape. For a general 2-d or 3-d object, the effect of traveling waves may not be so pronounced. The effect of linear loading on the image of a 2-d or 3-d object needs more experimental and numerical study.

VII. CONCLUSION

We have employed microwave diversity imaging to treat the problem of RCS management. RCS management is based on understanding of the scattering mechanisms of the object and the reconstruction algorithm in microwave diversity imaging. A new term "diaphanization," defined as all techniques of reducing the RCS and techniques of obscuring the image, has been introduced. RCS management is treated not only from the detection point of view but also from the imaging perspective. The use of microwave diversity imaging as a tool opens a new direction for future research in RCS management studies. We have also shown that microwave diversity imaging is quite robust to the Gaussian noise. We also have proposed some fundamental concepts for obscuring an image. Some techniques of reducing the RCS have been applied to experimentally study their effect on RCS and imaging. It is found images are usually obscured at the price of increasing the RCS. How to reduce RCS and obscure images simultaneously is under investigation.

ACKNOWLEDGEMENT

This work was supported by grants from the Army Research Office, the Air Force of Scientific Research, RCA and GE Corporation.

REFERENCE

- [1] M. I. Skolnik, *Introduction to Radar Systems*, 2nd edition, McGraw-Hill Book Company, New York, 1980
- [2] E. F. Knott, in Chap. 7 of *Radar Cross Section*, E. F. Knott edit., Artech House, Dedham, MA. 1985.
- [3] N. H. Farhat, C. L. Werner and T. H. Chu, "Prospect for Three-Dimensional Projective and Tomographic Imaging Radar Networks," *Radio Science*, Vol.19, No. 5, pp.1347-1355, 1984.
- [4] H. J. Li, N. H. Farhat, and Y. Shen, "A New Iterative Algorithm for Extrapolation to Radar Imaging," to be published in *IEEE Trans. on Antenna and Propagation*, May 1987.
- [5] H. J. Li, N. H. Farhat, Y. Shen, and C. L. Werner, "Image Understanding and Interpretation in Microwave Diversity Imaging," to be submitted for publication.
- [6] S. R. Deans, "The Radon Transform and Some of its Applications," John Wiley & Sons, New York, 1983.
- [7] G. T. Ruck (ed.), *Radar Cross Section Handbook*, Plenum Press, New York, 1970
- [8] E. K. Miller and J. A. Landt, "Direct Time-Domain Techniques for Transient Radiation and Scattering from Wires," *Proceedings of the IEEE*, Vol.68, pp. 1396-1423, 1980.
- [9] W. H. Emerson, "Electromagnetic Wave Absorbers, Useful Tools for Engineer," Emerson & Cumming Co., Canton, MA,
- [10] R. F. Harrington, *Field Computation by Moment Methods*, Macmillan, New York, NY, 1968.
- [11] H. J. Li, N. H. Farhat, and Y. Shen, "Microwave Image of a Straight Wire Scatterer," *IEEE Antennas and Propagation International Symposium*, AP-S, Virginia, 1987.
- [12] N. H. Farhat and T. H. Chu, *Tomography and Inverse Scattering*, *International Commission on Optics, ICO-13, C1*, pp.62-63, 1984.

FIGURE CAPTION

Fig 1. Simplified sketch of a microwave diversity imaging arrangement

Fig.2 (a). Sketch of the B-52 test object and the angular window utilized. **(b).** Reconstructed image of B-52 **(c).** Sketch of the portion of the test object (darkened lines) covered with broad-band absorber. **(d).** The mean RCS versus aspect angle before and after diaphanization. **(e).** The reconstructed image after diaphanization displayed with the same dynamic range as the undiaphanized image in **(b)**. **(f).** Reconstructed image displayed with a lower dynamic range.

Fig.3 (a). Averaged scattered fields of the scale model B-52 after diaphanization versus aspect angle and the generated Gaussian noises with level N_1 and N_2 . Measured frequency response of the first view angle (broadside) **(b).** without added noise, **(c).** with noise level N_1 added, and **(d)** with noise level N_2 added. **(e).** The range profile of data in **(b)**; **(f).** The range profile of data in **(c)**; **(g).** the range profile of data in **(d)**;

A perspective stack range profiles of the first 64 view angles **(h)** without adding noise; **(i)** with noise level N_1 ; and **(j)** with noise level N_2 . The reconstructed image **(k)** without adding noise; **(m)** with noise level N_1 ; and **(n)** with noise level N_2 .

Fig.4 (a). Arrangement for the measurement of a square conducting plate. **(b).** Average scattered fields of a (40 x 40 cm) conducting plate before and after diaphanization. Reconstructed images of the plate **(c)** before and **(d)** after diaphanization.

Fig.5 (a). Pictorial View of scale model of B-1 bomber. **(b).** Reconstructed image using co-polarized waves. **(c).** Reconstructed image using cross-polarized waves.

Fig.6 (a). A conducting plate covered with ceramic substrate. **(b).** Measurement configuration. **(c).** Mean scattered fields of the plate without (solid line) and with substrates (dash-dotted line). **(d).** Reconstructed image of the conducting plate with angular window $(-30^\circ, 60^\circ)$. **(e).** Reconstructed image of the ceramic-covered plate with angular window $(-30^\circ, 60^\circ)$. **(f).** Reconstructed image of the conducting plate with angular window $(5^\circ, 60^\circ)$. **(g).** Reconstructed image of the ceramic-covered plate with angular window $(5^\circ, 60^\circ)$.

Fig.7 (a). Geometry of a straight wire with impedance loading. **(b).** Real part and imaginary part of the frequency response of the straight wire without impedance loading **(c).** Reconstructed image of the wire with angular window $(20^\circ, 90^\circ)$ containing broadside view. **(d).** Reconstructed image of the wire with angular window $(20^\circ, 84^\circ)$, excluding broadside view **(e).** Reconstructed image of the loaded wire with angular window $(20^\circ, 90^\circ)$. **(f).** Reconstructed image of the loaded wire with angular window $(20^\circ, 84^\circ)$.

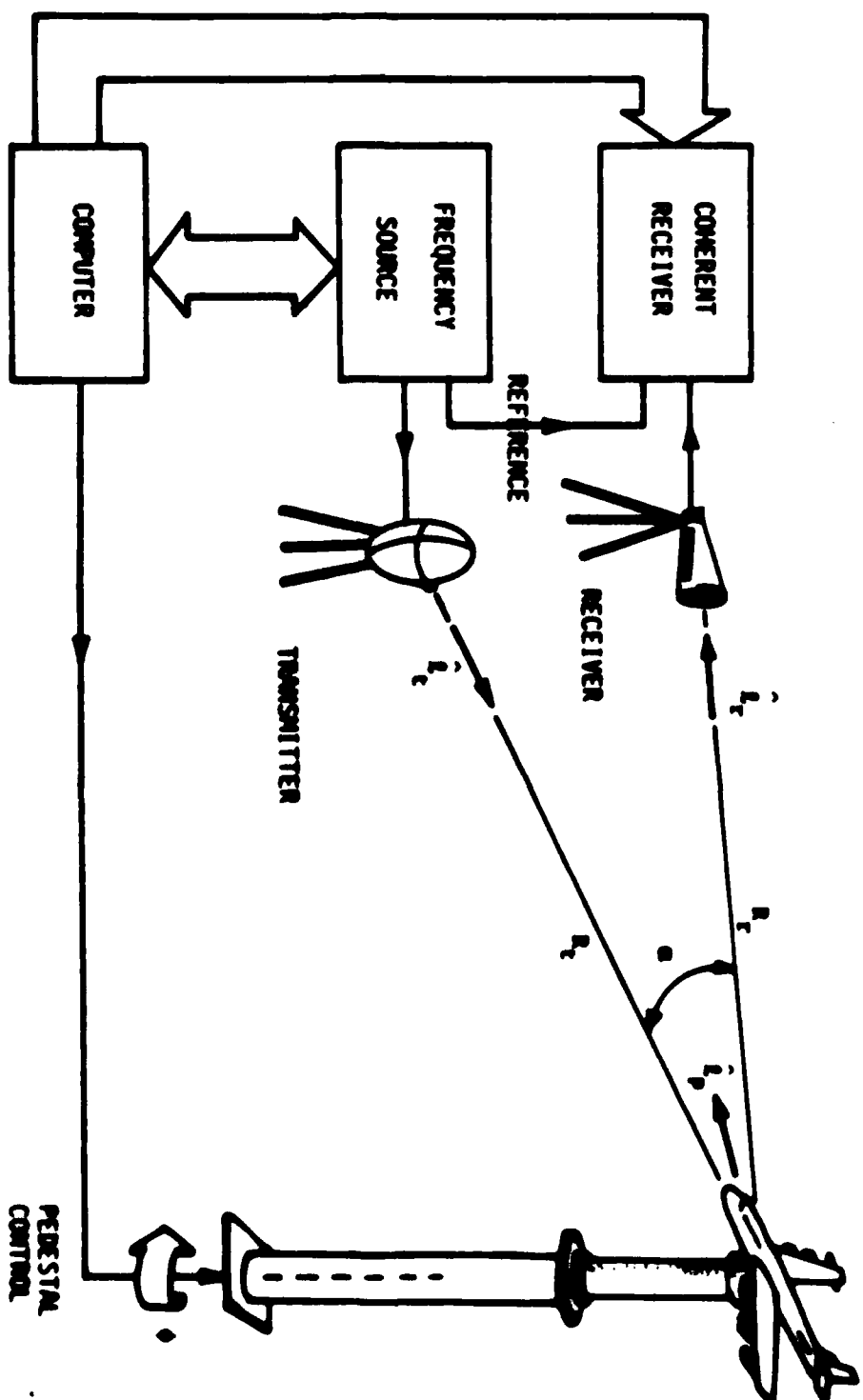


Fig 1. A simplified microwave diversity imaging arrangement

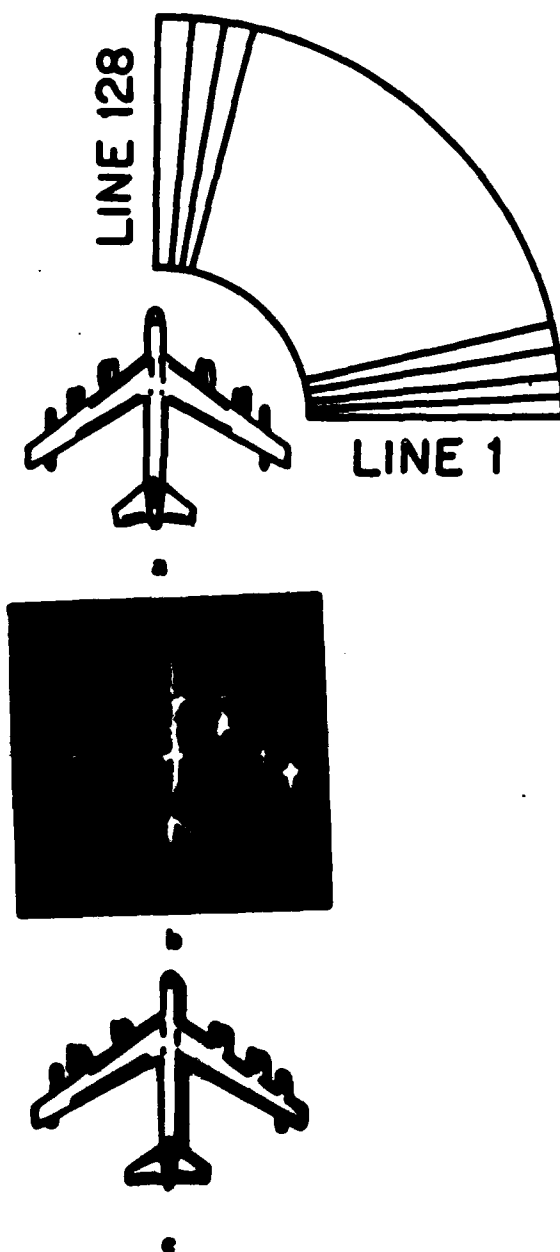


Fig.2 (a). Sketch of the B-52 test object and the angular window utilized.

(b). Reconstructed image of B-52

(c). Sketch of the portion of the test object (darkened lines) covered with broad-band absorber.

(to be continued)

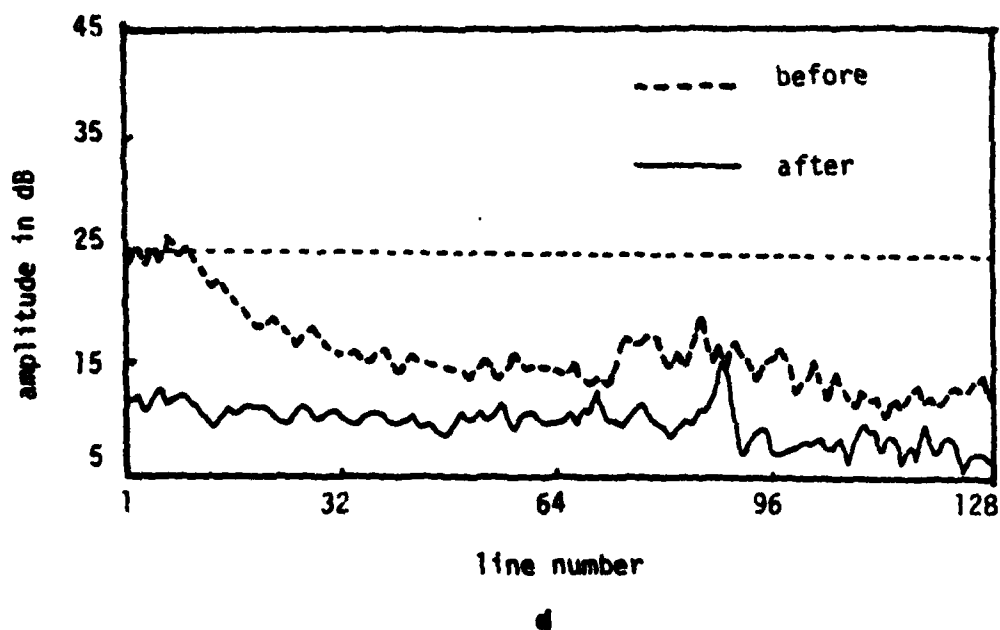
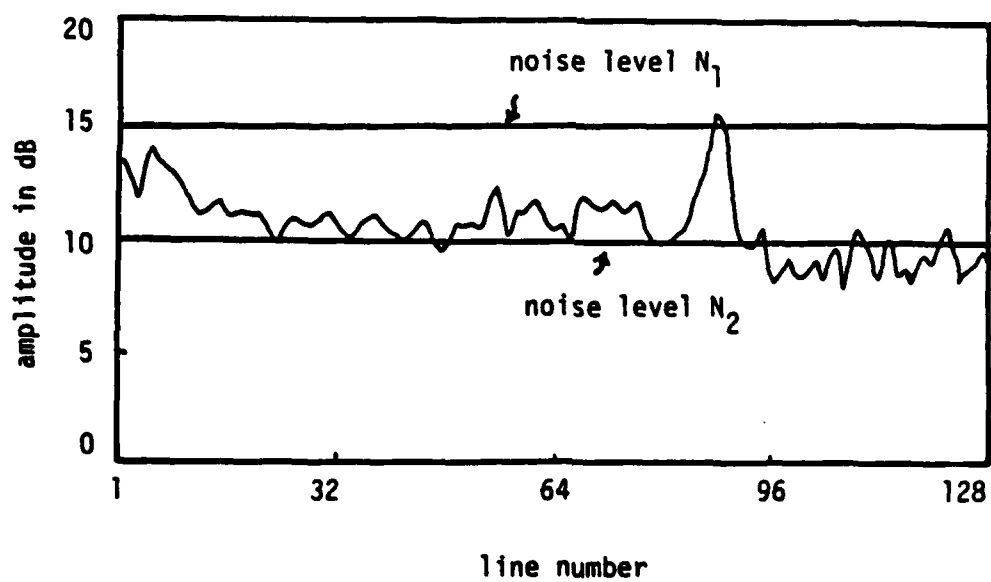


Fig. 2 (continued)

- (d). The mean RCS versus aspect angle before and after diaphanization.
- (e). The reconstructed image after diaphanization displayed with the same dynamic range as the undiaphanized image in (b).
- (f). Reconstructed image displayed with a lower dynamic range.



(a)

Fig.3 (a). Averaged scattered fields of the scale model B-52 after diaphanization versus aspect angle and the generated Gaussian noises with level N_1 and N_2 .

(to be continued)

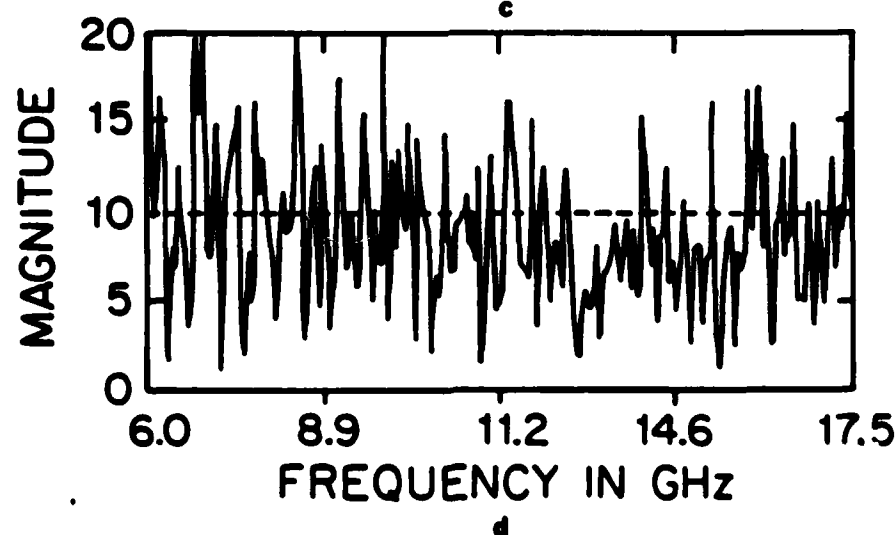
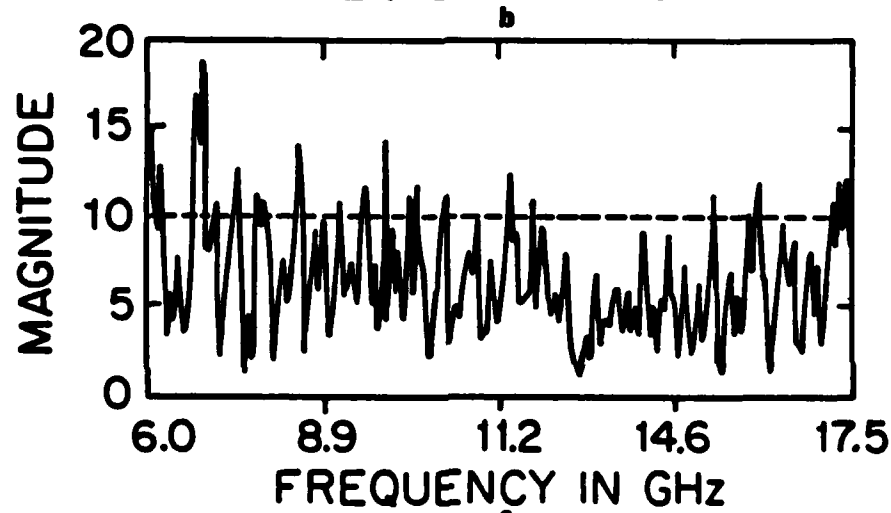
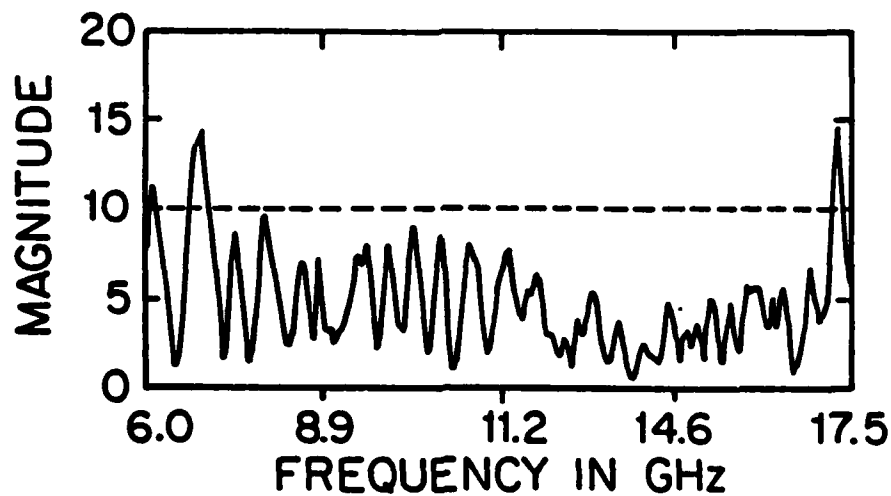


Fig. 3 (continued)

Measured frequency response of the first view angle (broadside)
 (b). without added noise, (c). with noise level N_1 added,
 and (d) with noise level N_2 added.

(to be continued)

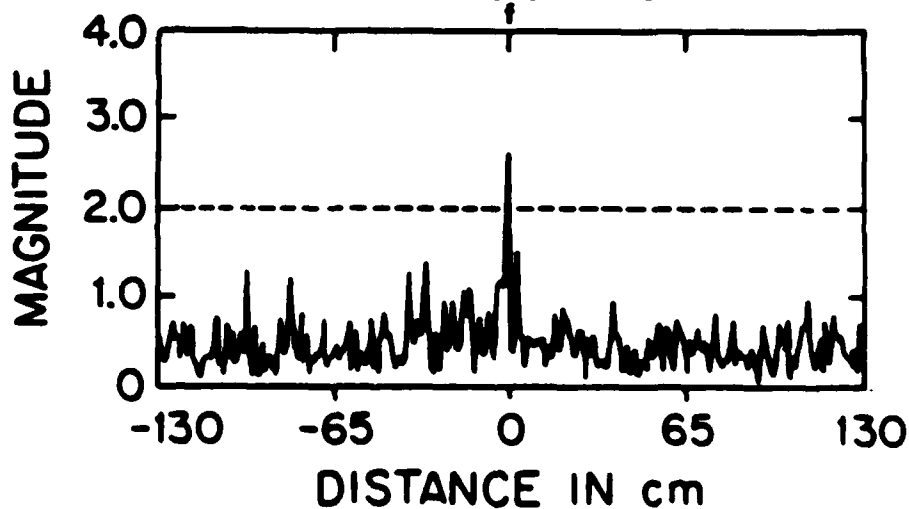
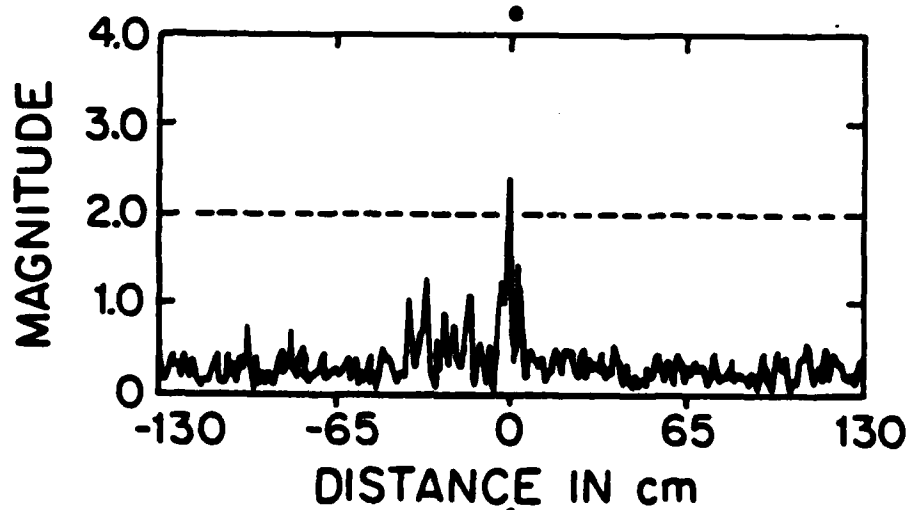
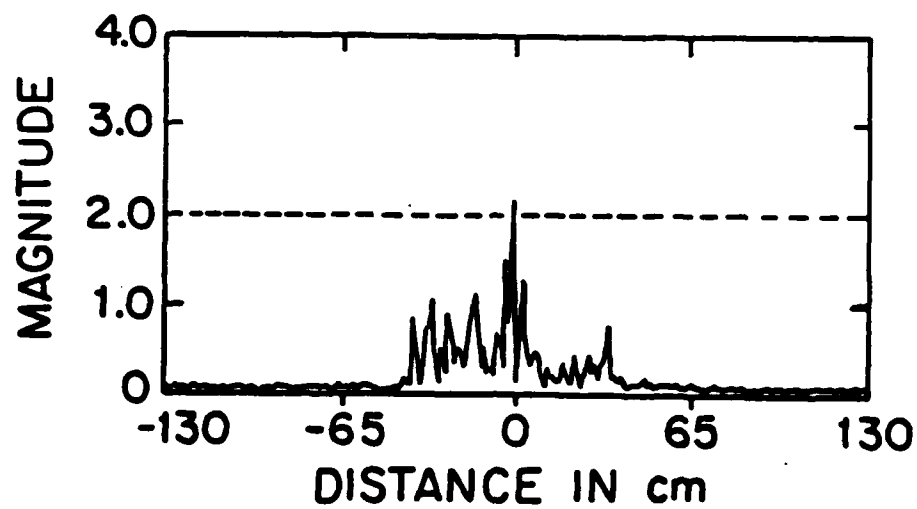
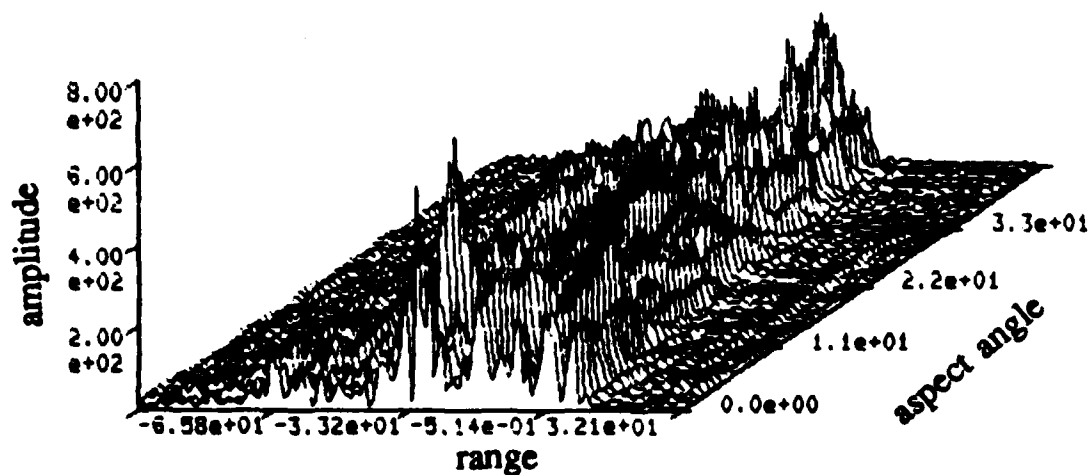


Fig. 3 (continued)

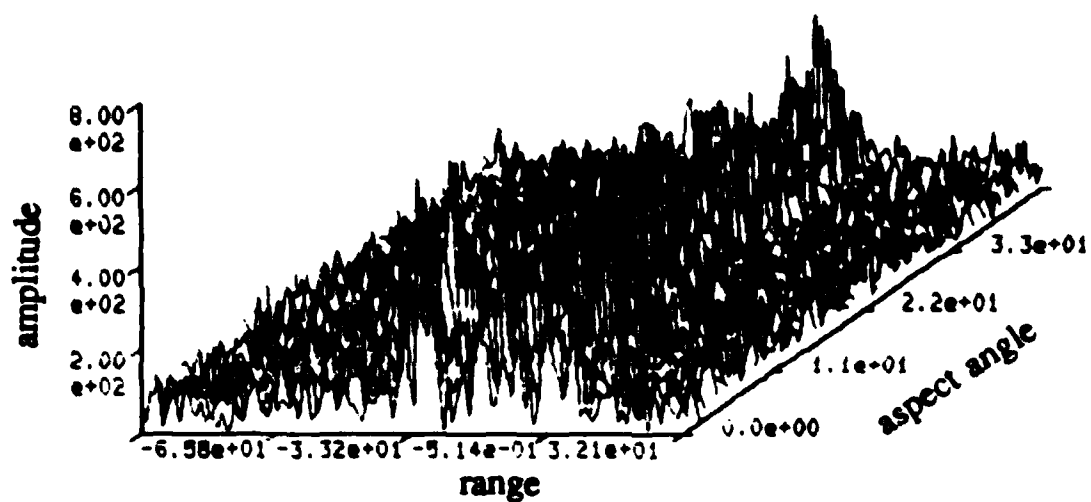
(e). The range profile of data in (b); (f). The range profile of data in (c);

(g). the range profile of data in (d);

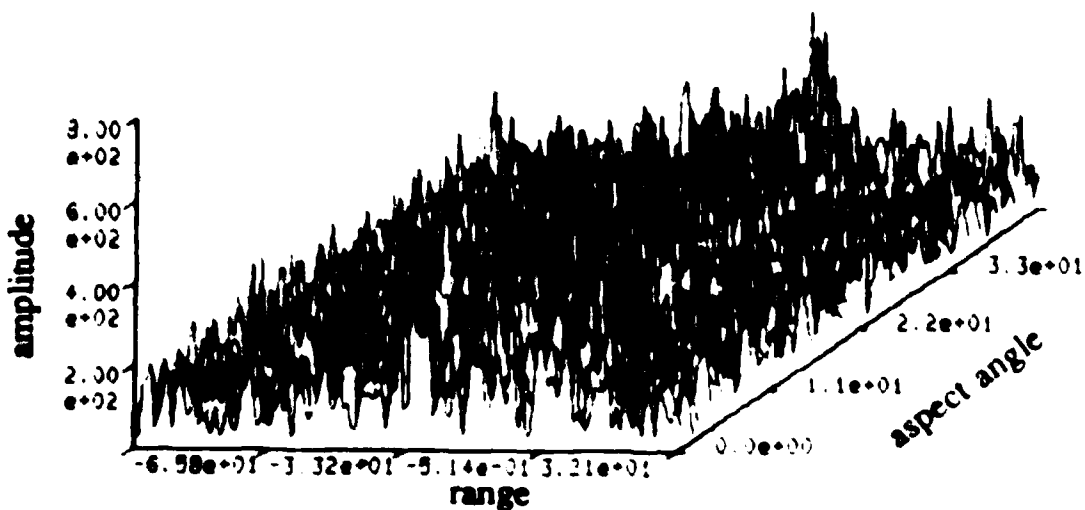
(to be continued)



h



i



j

Fig. 3 (continued)

A perspective stack range profiles of the first 64 view angles (h) without adding noise; (i) with noise level N_1 ; and (j) with noise level N_2

(to be continued)



k



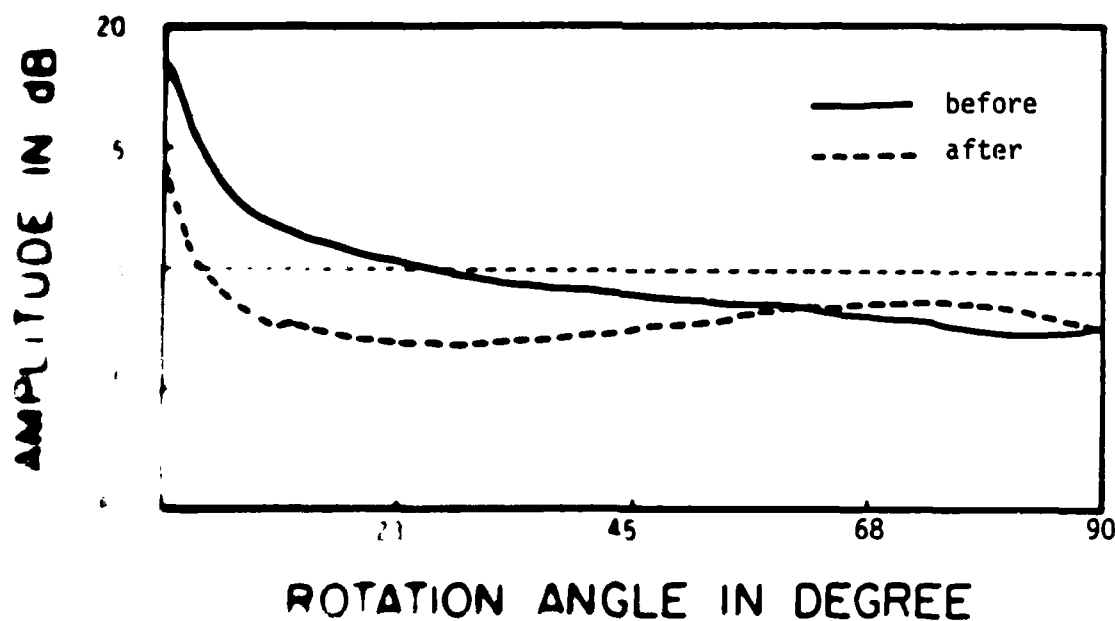
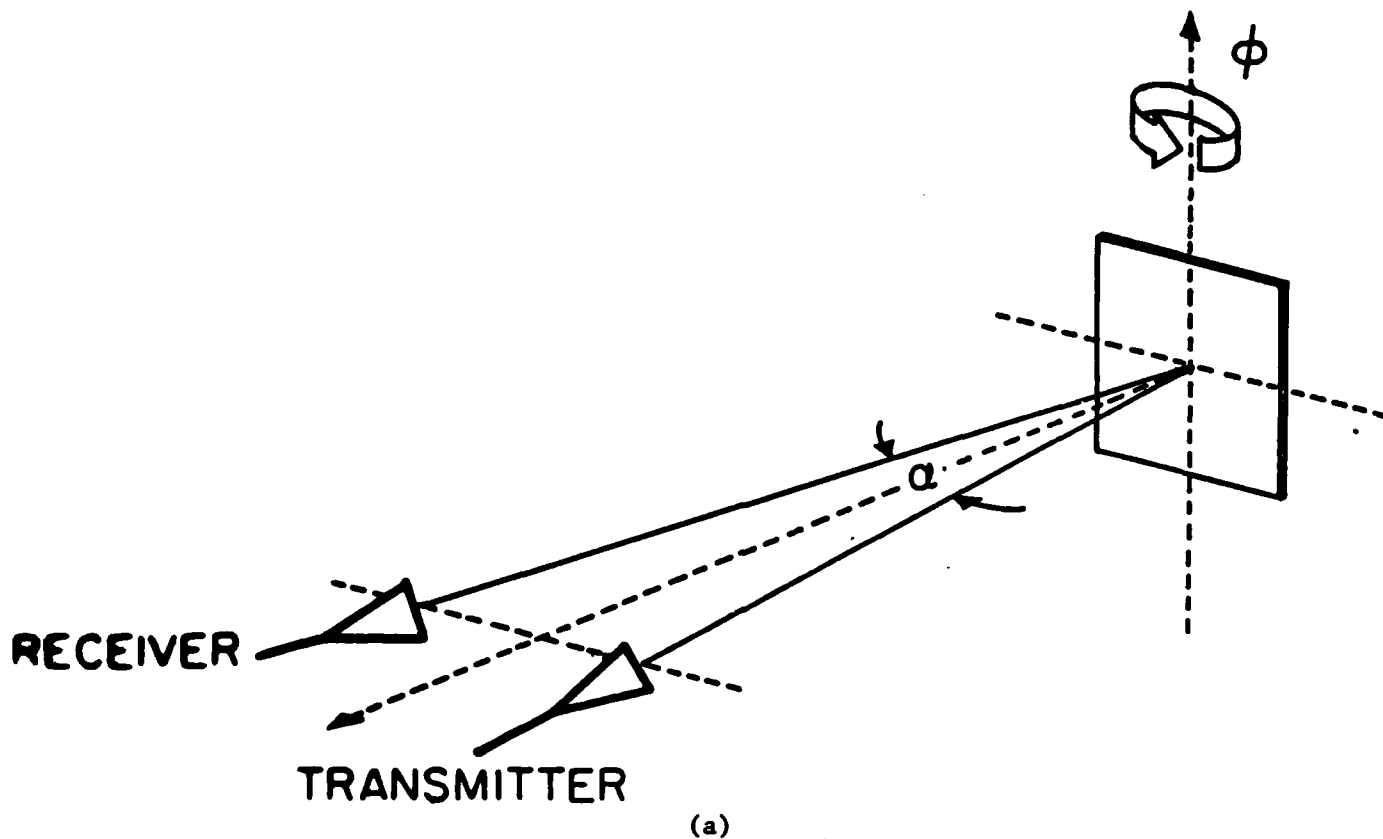
m



n

Fig.3 (continued)

The reconstructed image (k) without adding noise; (m) with noise level N_1 ; and (n) with noise level N_2 .



(b)

Fig. 1. a - Arrangement for the measurement of a square conducting plate.
 b - Average measured fields of a (40 x 40 cm) conducting plate
 before and after lengthening
 c - calculated



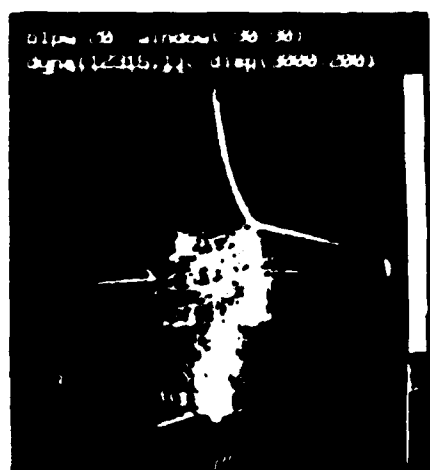
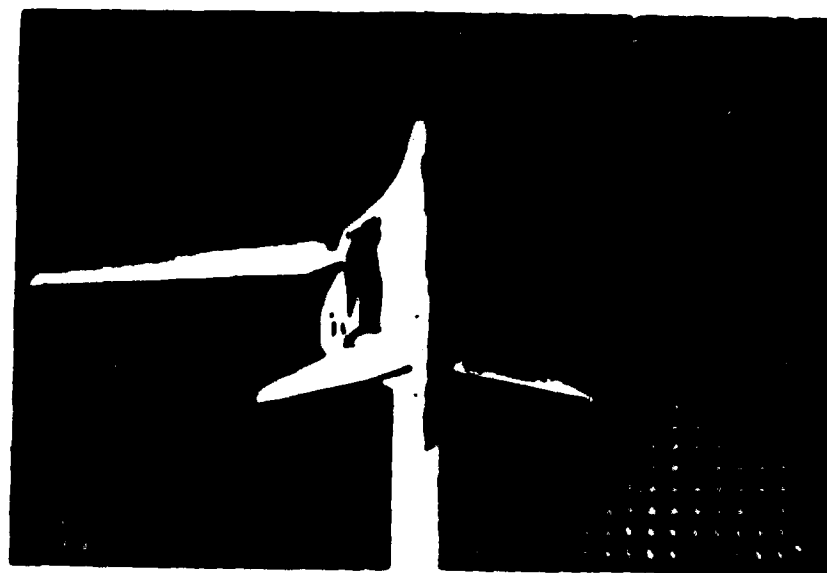
c



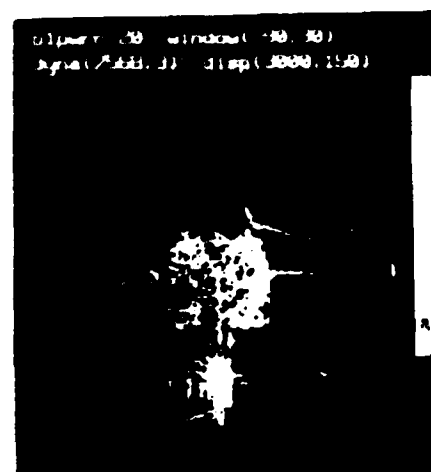
d

Fig. 4 (continued)

Reconstructed images of the plate
(c) before and (d) after diaphanization.



b



c

Fig.5 (a). Picture of the scale model B-1 bomber.
 (b). Reconstructed image using co-polarized waves.
 (c). Reconstructed image using cross-polarized waves.

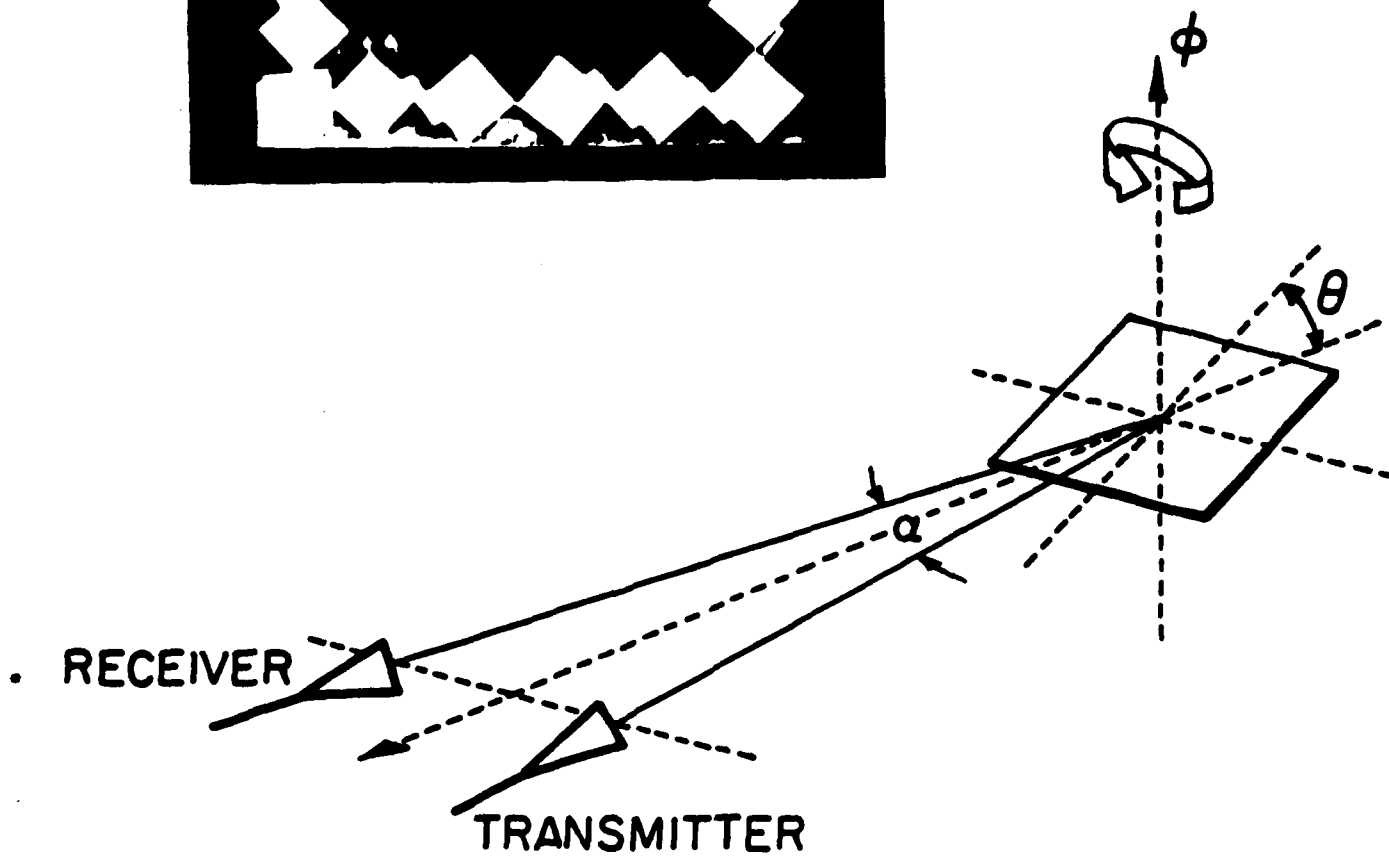
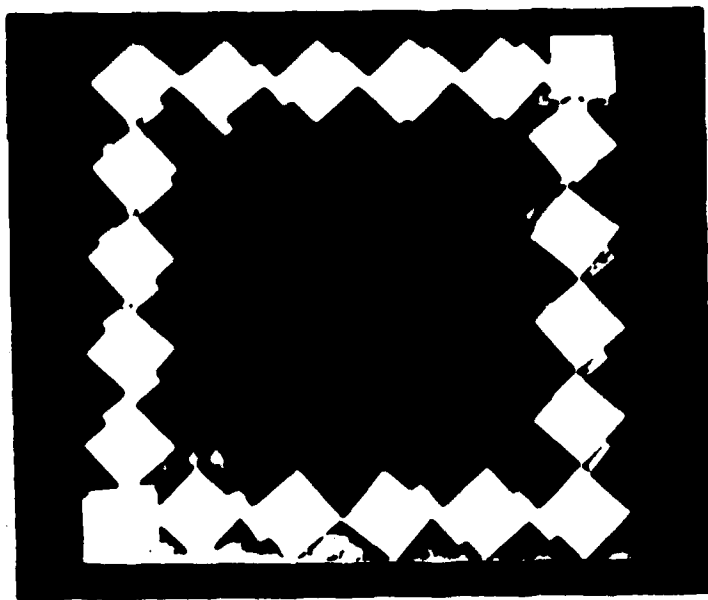
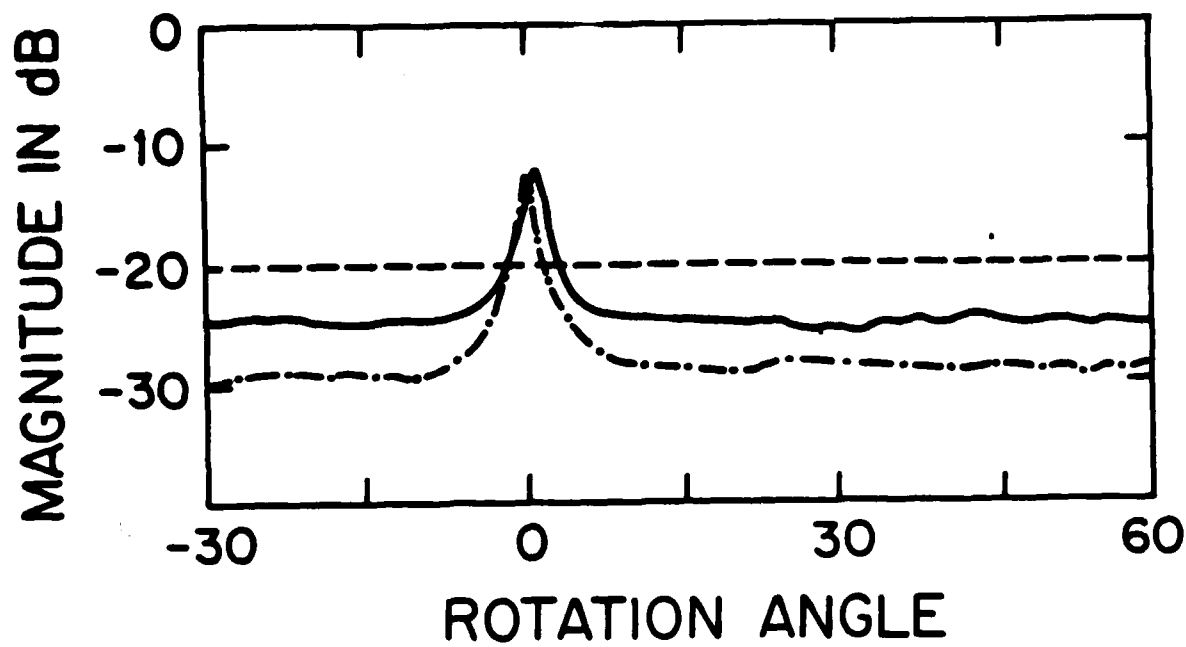
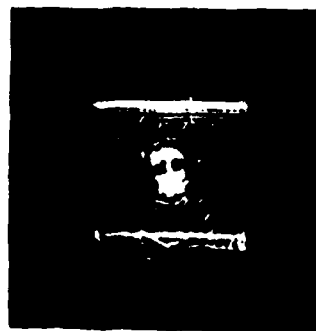


Fig.6 (a). A conducting plate covered with ceramic substrate.
 (b). Measurement configuration.
 (to be continued)



d



e



f



g

Fig. 6 (continued)

- (c). Mean scattered fields of the plate without (solid line) and with substrates (dash-dotted line).
- (d). Reconstructed image of the conducting plate with angular window (-30° , 60°).
- (e). Reconstructed image of the ceramic-covered plate with angular window (-30° , 60°).
- (f). Reconstructed image of the conducting plate with angular window (5° , 60°).
- (g). Reconstructed image of the ceramic-covered plate with angular window (5° , 60°).

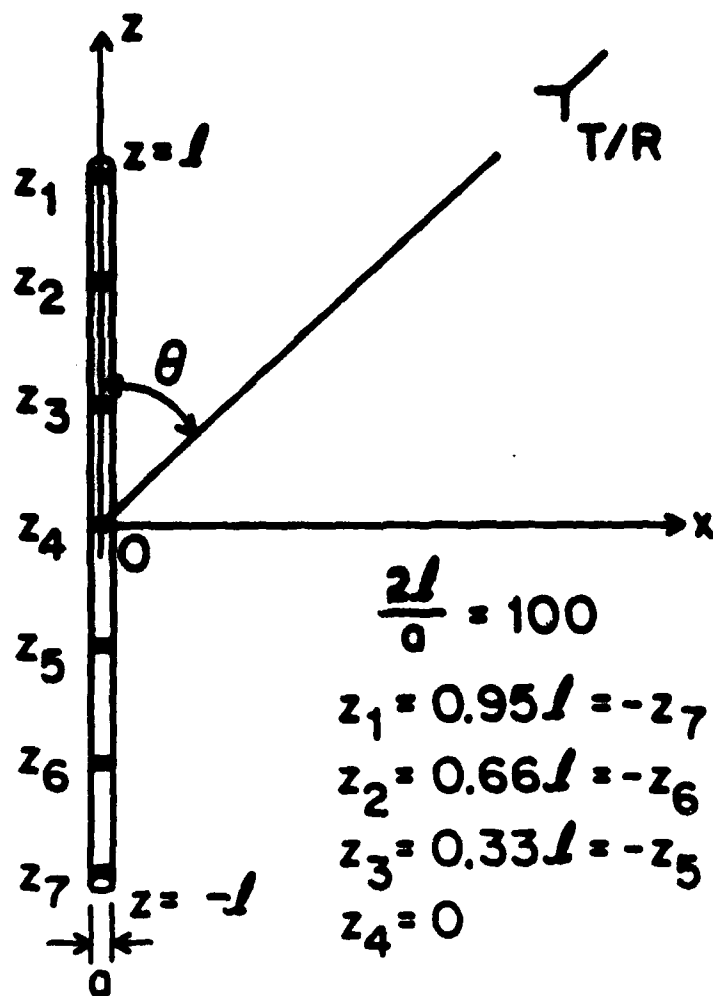


Fig.7 (a). Geometry of a straight wire with impedance loading.
(to be continued)

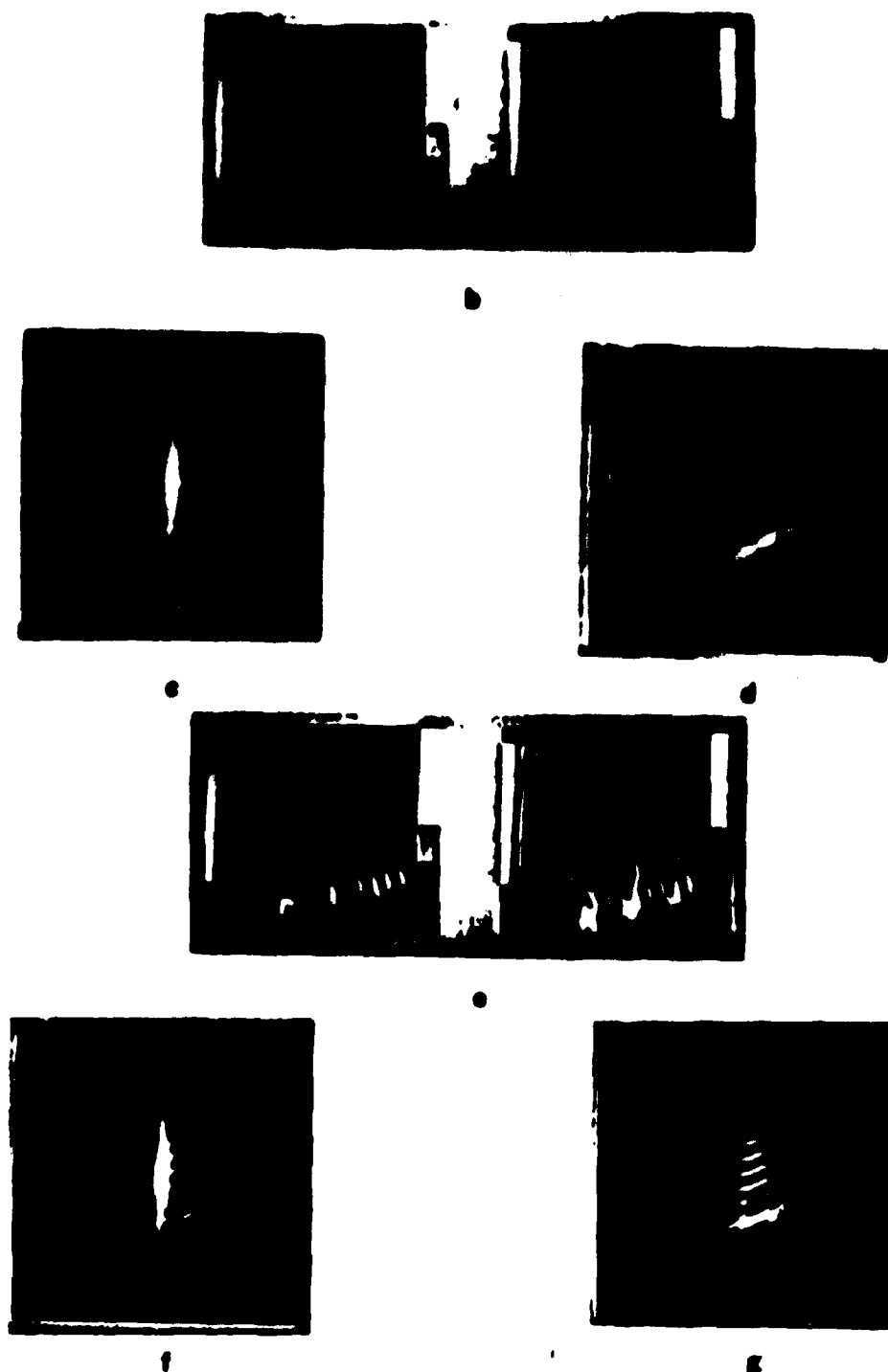


Fig. 7 (continued)

- (b). Real part and imaginary part of the frequency response of the straight wire without impedance loading
- (c). Reconstructed image of the wire with angular window (20° , 90°) containing broadside view.
- (d). Reconstructed image of the wire with angular window (20° , 84°) excluding broadside view
- (e). Reconstructed image of the loaded wire with angular window (20° , 90°).
- (f). Reconstructed image of the loaded wire with angular window (20° , 84°).

APPENDIX III

A MULTIFUNCTIONAL MICROWAVE/MILLIMETER WAVE MEASUREMENT FACILITY FOR MULTISTATIC IMAGING AND TARGET CLASSIFICATION STUDIES

M. Farhat and Y. Shen

I. INTRODUCTION

A measurement system capable of acquiring data covering the microwave/millimeter-wave ($\mu\text{W}/\text{mmW}$) region of the spectrum is a valuable tool in many areas of research. For example, in the study of inverse scattering, the scattered fields from a test object are dependent on the wavelength of the illumination, therefore the availability of scattered data over a wide bandwidth would be important in gaining insight into the scattering phenomenon and in characterizing the object. In the areas of coherent imaging, the wide bandwidth implies better range resolution which leads to high resolution images that are suited for recognition by the human eye-brain system as in microwave and millimeter wave diversity imaging where angular, spectral, and polarization degrees of freedom are combined to cost-effectively form images of scattering objects with near optical resolution.

It is well known that combinations of different polarization states of the incident field and of the antennas receiving the scattered field provide different information about the scatterer. A total of four polarization state combinations, corresponding to the four elements of the scattering matrix, is therefore needed to fully characterize scattering by an object,

provided that other factors such as antenna positions remain fixed. Thus being able to change the polarization states of the incident field and of the antennas measuring the scattered field is important in the study of depolarization effects and target identification utilizing polarization descriptors. It is also worth noting that polarization effects are more pronounced in multistatic and bistatic measurements than monostatic measurement.

Besides the bandwidth and the polarization considerations, the scattered fields are also dependent on the locations and the directions of the transmitting and the receiving (T/R) antennas. A system that allows change in the locations and the orientations of the T/R antennas is useful in aperture synthesis and in bistatic and multistatic scattering and imaging studies. The system can also be used to study the scattering effects in different radiation zones, e.g. near-field versus far field coherent imaging.

In summary, a system that provides wide bandwidth, variable polarization states of the incident field and the measured field, and relocatable positions of the transmitting and receiving antennas relative to the object is a highly desirable tool for the study of $\mu\text{w/mm}$ scattering, imaging, and target representation. The aforementioned features are also referred to as wavelength, polarization, and positional or angular (aspect related) diversities respectively. In the following sections, a measurement system designed to meet these desirable features is described. The system is an upgraded version of the original 9-2018) GHz system configuration residing at the Electro-Optics & Microwave-Optics Laboratory of the Moore School of Electrical Engineering at the University of Pennsylvania which was utilized in our earlier microwave diversity imaging studies. The upgraded system is intended to extend operational capabilities to 60 GHz and to enable

multistatic scattering measurements employing the same operation principles as in the original system but employing different gear.

II. ORIGINAL SYSTEM CONFIGURATION

Shown in Fig. 1 is a schematic diagram of the present system operating from 2 to 18 GHz (S, C, X, and Ku bands in the radar letter-band nomenclature). Two microwave sources, a sweeper oscillator (HP-8620C) and a sweep synthesizer (HP-8340A), are available; either one can be used as the illuminating source. The coherent detector is a network analyzer (HP-8410B or HP-8510A) with a reflection/transmission test unit (HP-8743 or HP-8513). The combination of HP-8620C/8410B can operate from 2 to 18 GHz, while HP-8340A/85120A combination allows operation from 45 MHz to 26.5 GHz. The illuminating signal is amplified by a solid-state amplifier (Litton M5401-00) which furnishes 1 watt in the 2-6 GHz range, and by a TWT amplifier (Varian VZM6991K3) with maximum 10 watts output in 8-18 GHz range before being fed to the transmitting antenna. The TWT, however, is usable in 6-8 GHz with lower gain. Thus the operating bandwidth is limited by the power amplifier to the 2-18 GHz range. Switching between amplifiers is performed manually.

A portion of the transmitted signal is extracted for use as the reference signal and for the source leveling circuit in the HP-8620C/8410B system. For the HP-8340A/8510A combination, a fraction of the output of the source before amplification is used directly as the reference.

A parabolic reflector antenna (AEL APN 102C 18") with interchangeable right-hand-circular and left-hand-circular polarization (RHCP/LHCP) feeds (Transco 9C27400) is used in the 2-18 GHz to produce circularly polarized illumination. The receiving antenna is a dual polarization horn (EM A6100) with a 90 degree hybrid for circular polarization measurement. To obtain measurements of horizontal and vertical (H/V) polarizations, a pair of dual polarization horns (EM A6100) is used without the hybrid. The circular

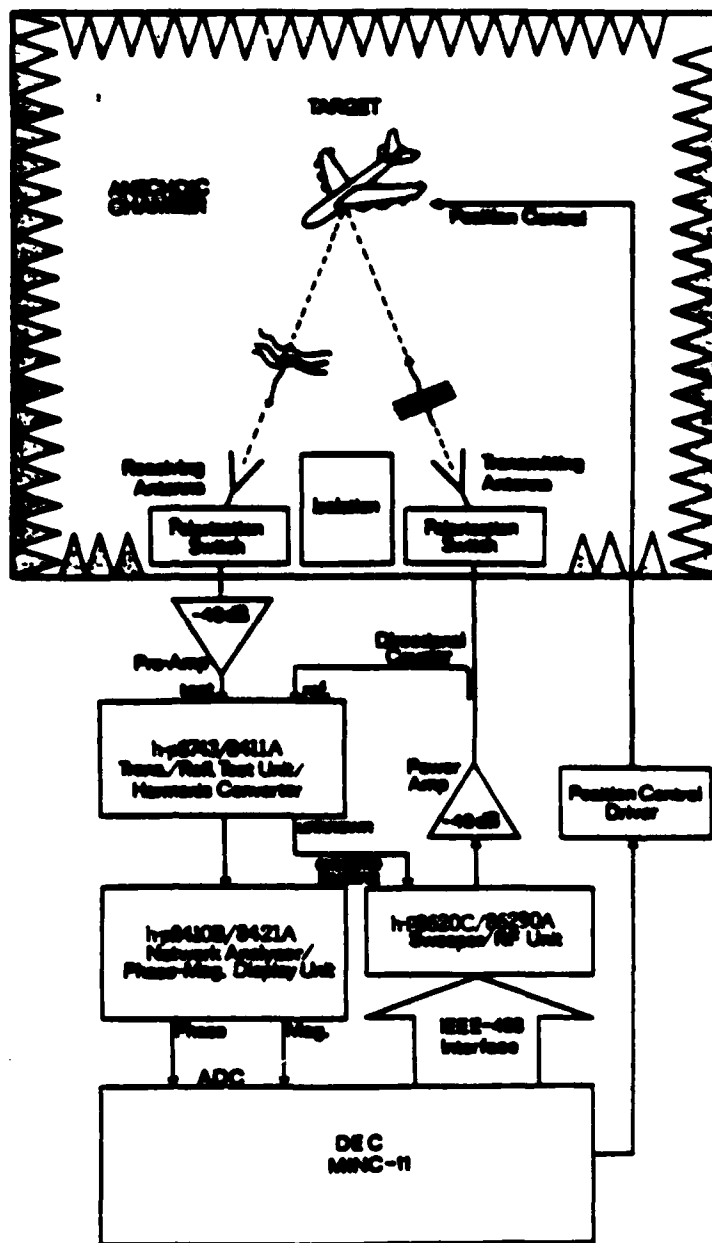


Fig. 1. Experimental Microwave Measurement and Imaging Facility (original system configuration)

polarization states of the RHCP/LHCP measurements are switched manually, while those of the H/V polarization measurements can be switched electronically.

The received field is amplified by low noise solid-state amplifiers, an Avantek AWT-8039M in 2-8 GHz and an Avantek AWT-18039M in 8-18 GHz, with both having about 50 db gain. The pre-amplifiers are switched manually. The amplified signal is then fed to the test channel of the reflection/transmission test set operating in transmission mode, and detected by the network analyzer.

The test range is a rectangular anechoic chamber with dimensions 50' long, 20' wide, and 20' high. The test object is mounted on a pedestal located at the center of the chamber. The T/R antennas are located at one end of the chamber, with slight angular separation between them for insertion of electromagnetic wave absorbing materials to minimize mutual coupling. The main beams of the T/R antennas are manually steered toward the test object for better signal-to-noise ratio. Aside from the slight bistatic angle between the T/R, the arrangement is essentially monostatic. The pedestal is rotated by a stepping motor to change the aspect angles of the test object relative to the T/R which are stationary.

III. UPGRADED SYSTEM CONFIGURATION

The new system to be described next is an upgraded version of the original system described in the preceeding section with several new salient features added. Many of the components used in the original system are incorporated into the new system. Added features of the new system include:

1. Wide bandwidth coverage ranging from 2 GHz to 60 GHz. Thus the operating bandwidth is nearly tripled, covering the microwave region and a

lower segment of the millimeter-wave region. In conventional radar letter-band nomenclature, the system coverage is from S band up to U band. Small frequency gaps may exist between bands due to hardware limitations.

2. Most of the switching between components of different bands are controlled electronically. That part that cannot be switched remotely is due to unavailable hardware. But the system may become fully automated in the future as broadband switches become available.

3. An x,y,z, θ , ϕ positioner that enables positioning a broadband receiver module to nearly any coordinate location in the anechoic chamber and enables orienting the receiver module towards the stationary target greatly enhances the versatility of the new system. Bistatic and multistatic measurements for polarization and aperture synthesis studies that were impossible or difficult earlier can be performed readily with the new system. A sketch of the anechoic chamber depicting the positioner and showing the scattering object located on a separate elevation over azimuth positioner to change the target aspect relative to the receiving module and a stationary transmitter antenna is given in Fig. 2.

Figure 3 depicts the basic blocks of the upgraded system. A central consideration in the design of the upgraded system is the realization of a (2-60) GHz receiver module that is translatable for carrying out bistatic and multistatic scattering measurements. The source generates highly accurate and stable RF signals from 2 to 60 GHz in either sweep mode or stepped frequency CW mode. The transmitter assembly comprises a bank of power amplifiers and the switches needed to guide the signal through an appropriate signal path in accordance with its frequency as detailed in Fig. 4. The amplified signal is coupled out and downconverted to a lower frequency.

AD-A181 252

RESEARCH IN IMAGE UNDERSTANDING AS APPLIED TO 3-D
MICROWAVE TOMOGRAPHIC I. (U) MOORE SCHOOL OF ELECTRICAL
ENGINEERING PHILADELPHIA PA ELECTR. N H FARHAT MAR 87

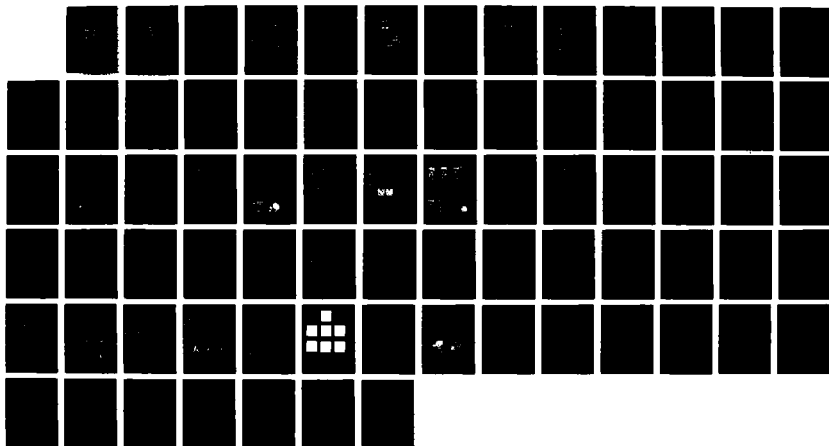
2/2

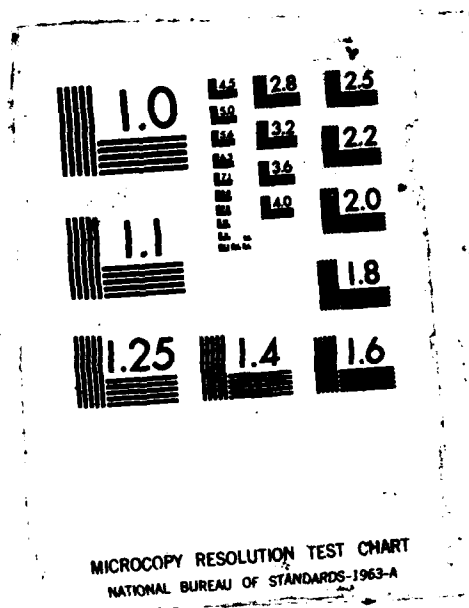
UNCLASSIFIED

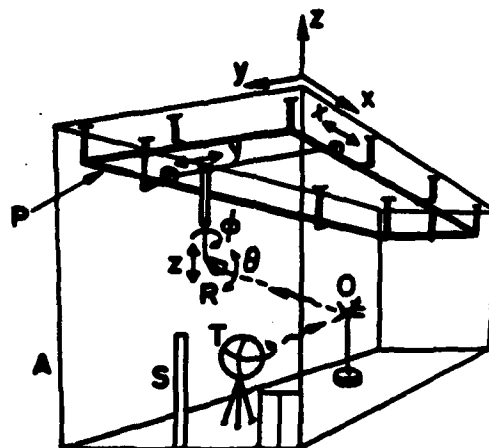
EO/MO-10 AFOSR-TR-87-0741 AFOSR-81-0240

F/G 17/9

NL







- A-Anechoic chamber
- T-Transmitting antenna (illuminator)
- O-Test object (scatterer) mounted on its own elevation over azimuth positioner
- R-Positioner mounted receiver module
- P-Positioner frame
- S-Window for cable connections to external instrumentation

Fig. 2. Sketch of anechoic chamber showing receiver module R mounted on x, y, z, θ, ϕ positioner and scattering object O mounted on an elevation over azimuth positioner in front of a stationary illuminating antenna T.

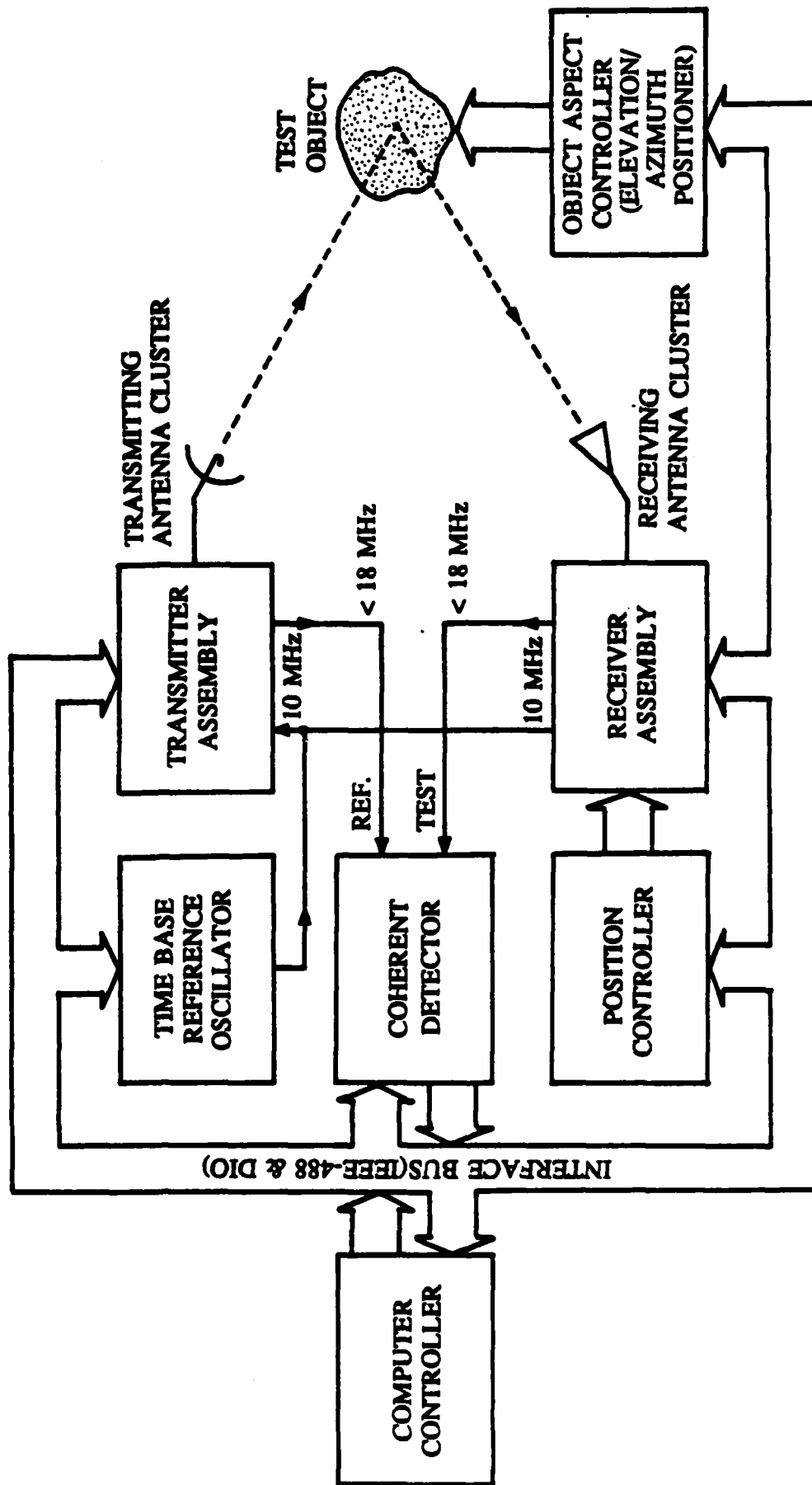


Fig. 3. Block diagram of upgraded system.

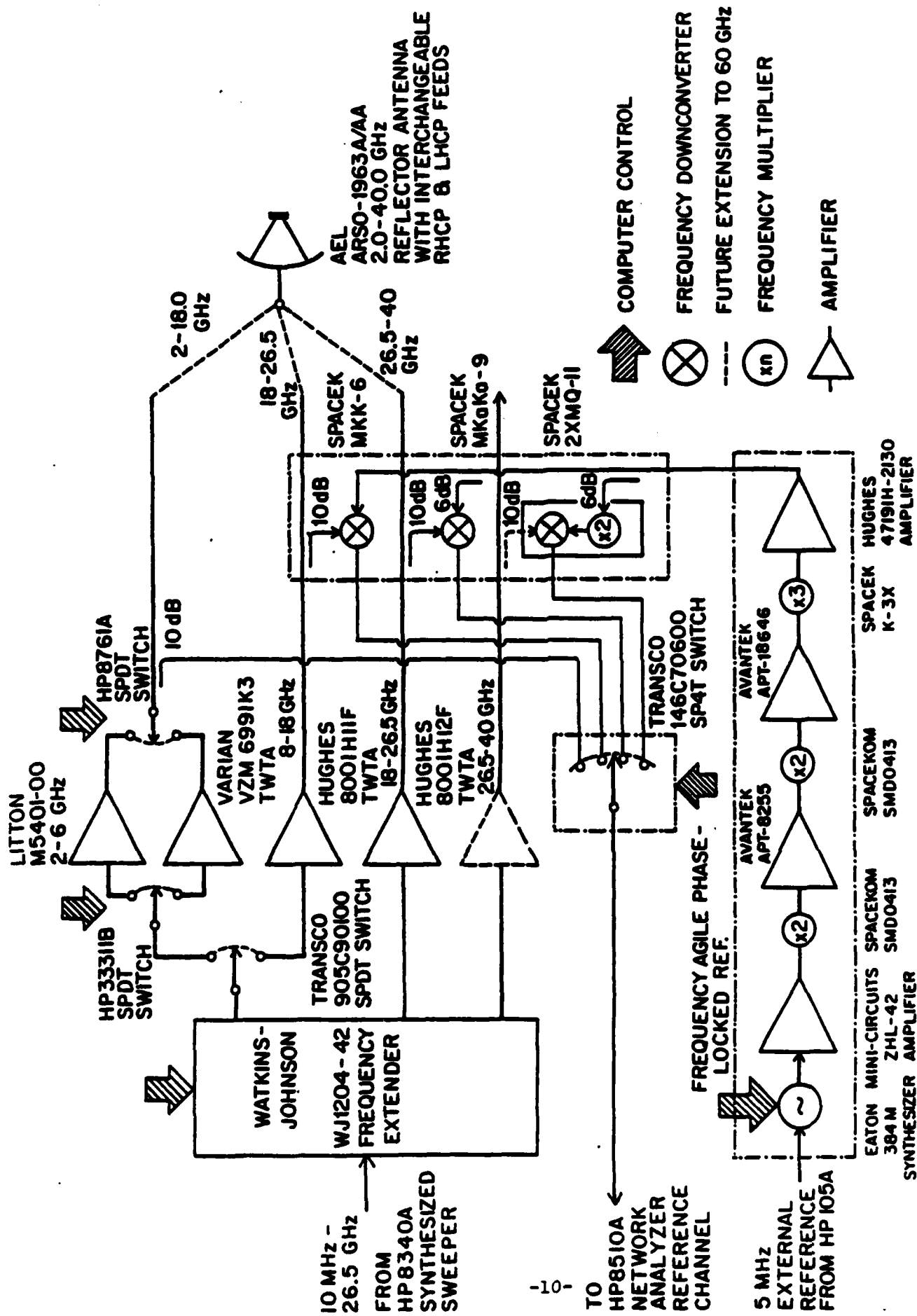


Fig. 4. Detail of (2-60) GHz transmitter assembly.

reference signal for the coherent detector (HP-8510A network analyzer). A local oscillator, phase-locked to a 10 MHz or 5 MHz external reference derived from the time base reference oscillator of the source, furnishes 26.5 GHz for the down-conversion. The major portion of the amplified signal radiates through the transmitting antenna cluster, which consists of high gain antennas of different bands. Further details of the transmitter assembly are given in Fig. 5.

The scattered field is captured by the receiving antenna cluster, the front end of the receiver assembly, shown schematically in Figs. 6 and 7 which consists of several antennas of different bands. The received signal is passed through a bank of switches to effect polarization diversity reception and a bank of low noise amplifiers to attain sufficient signal level for downconversion. Again; a local oscillator, also phase-locked to the 10 MHz or 5 MHz signal derived from the time base reference oscillator of the source, provides the 26.5 GHz reference to downconvert the signal to below 18 GHz. The downconverted signal is then passed through a second bank of amplifiers to increase the power level before being fed to the test channel of the coherent detector (HP 8510A network analyzer) via a low-loss flexible coaxial cable.

The coherent detector is in essence the HP-8510A network analyzer with the HP-8513 reflection/transmission test set. The reference channel input, derived from the transmitted signal, and the test channel input, which is the downconverted returned signal, are again downconverted twice, first to 20 MHz in the HP-8513, then to 100 KHz inside the HP-8510A, before being sampled and fed to the amplitude-phase detector portion of the HP 8510A. The network analyzer is always phase-locked to the reference channel input.

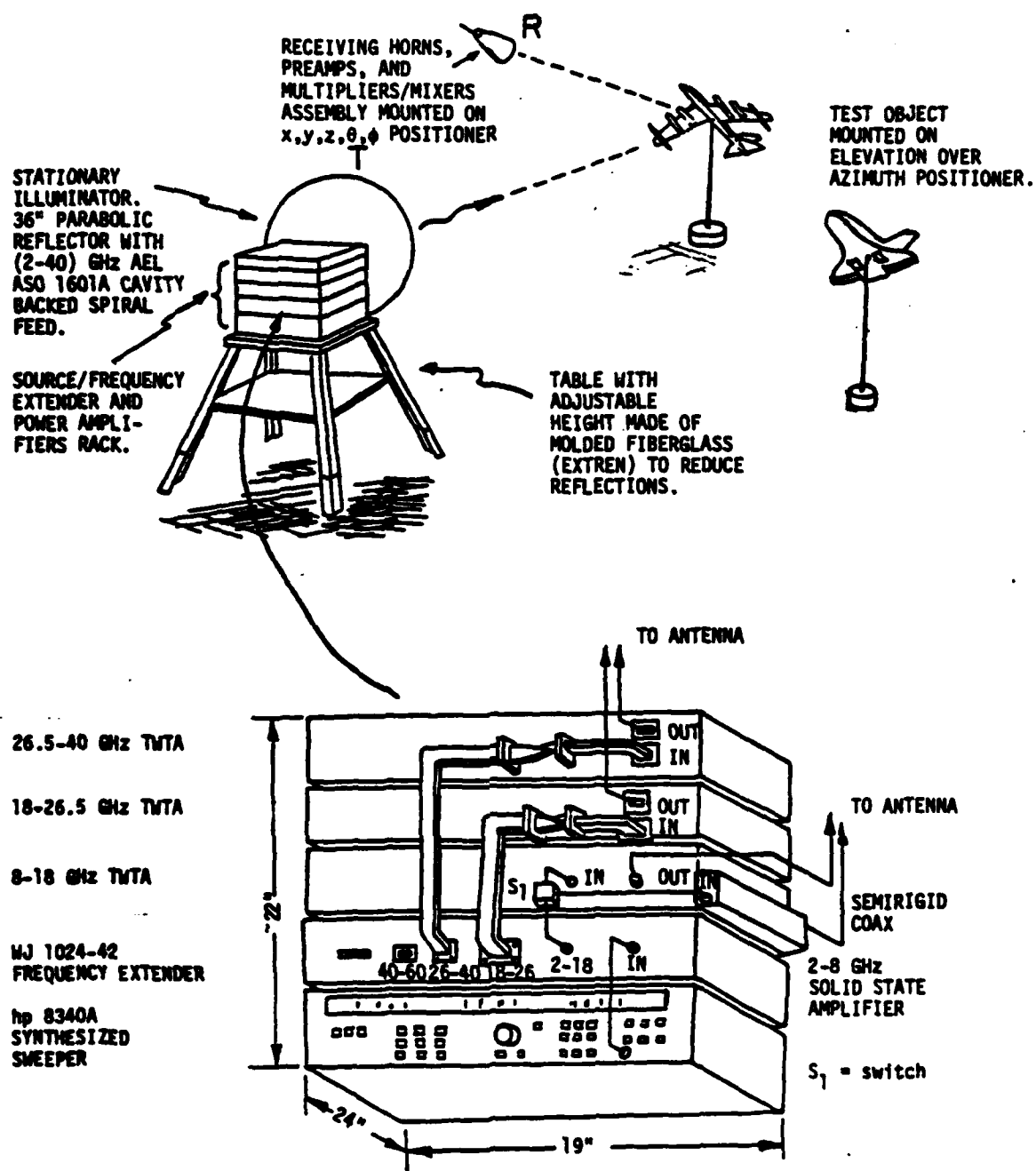


Fig. 5. Transmitter assembly consisting of microwave source (synthesized sweeper), frequency extender, power amplifier pack, and parabolic reflector antenna for use in the study of monostatic and bistatic λ and polarization diversity imaging in an anechoic chamber environment.

There are two position control interfaces: one is for the receiver module (receiver assembly with the receiving antenna cluster), and the other for the test object aspect control. The receiver module can be moved to almost any location in the anechoic chamber, and be oriented so that the antenna cluster is aiming toward the test object. The test object aspect control is realized by mounting it on an elevation over azimuth positioner. All these units, including the source, the transmitter/receiver assemblies, the coherent detector, and the position controls, are under the coordination of a computer/controller shown in the block diagram of Fig. 3. The computer/controller controls these units via the IEEE-488 bus and parallel digital I/O lines. Next we'll describe each block in Fig. 3 in more detail.

IV. THE SOURCE

A simplified version of the source is shown in Fig. 8. It is comprised of two parts: a HP-8340A sweeper synthesizer and a Watkins-Johnson WJ-1204-42 frequency extender, (see also Figs. 4 and 5). This combination delivers signals with greater than 0 dBm unlevelled power and synthesized frequencies over 0.1-60 GHz range. The HP-8340A covers frequency range 10 MHz to 26.5 GHz with minimum levelled power output of about 5 dBm over the entire frequency range. Levelled power output is somewhat higher for lower frequency. For the WJ-1204-42 frequency extender, 0 dBm input power is sufficient. The synthesizer operates in either CW mode, stepped frequency mode, or sweep mode. The synthesizer is controlled by the IEEE-488 GPIB. A highly stable internal time base at 10 MHz of the synthesizer is also used as the phase-locked signal for the local oscillators in the transmitter/receiver assemblies.

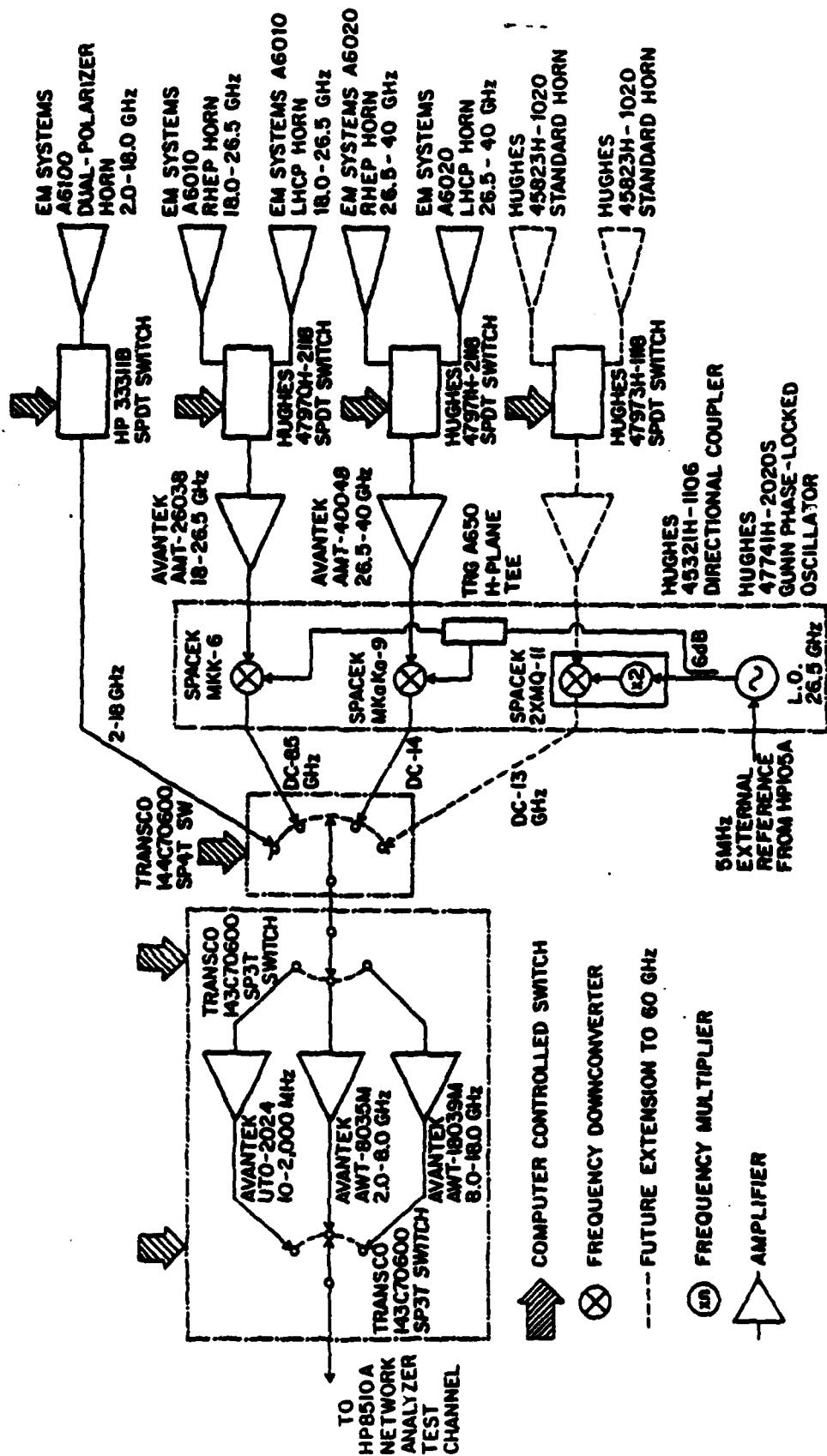
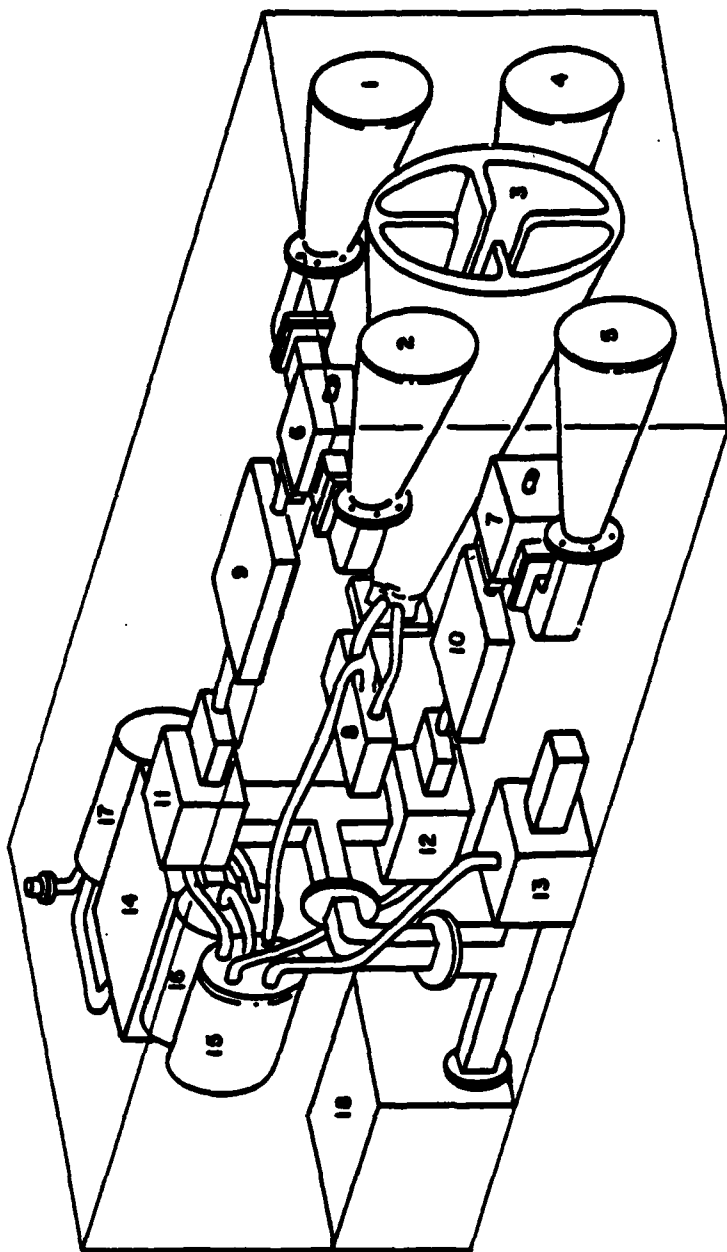


Fig. 6. Detail of 2-40 GHz receiver assembly (extendable to 60 GHz when components shown in dotted lines become available).



1. EM Systems A6010 RHCP Horn
2. EM Systems A6010 LHCP Horn
3. EM Systems A6100 Dual-polarized Horn
4. EM Systems A6020 RHCP Horn
5. EM Systems A6020 LHCP Horn
6. HUGHES 47970H-2118 SPDT Switch
7. HUGHES 47971H-2118 SPDT Switch
8. HP 33311B SPDT Switch
9. AVANTEK AMT-26038 Amplifier
10. AVANTEK AMT-40048 Amplifier
11. SPACEK MKK-6 Frequency Downconverter

12. SPACEK Mkaka-9 Frequency Downconverter
13. SPACEK 2xMQ-11 Frequency Multiplier & Downconverter
14. AVANTEK UTO-2024, AWT-8035M, AWT-18039M Amplifiers
15. TRANSCO 144C70600 SP4T Switch
16. TRANSCO 143C70600 SP3T Switch
17. TRANSCO 143C70600 Sp3T Switch
18. HUGHES 47741H-2020S Gunn Phase-Locked Oscillator

Fig. 7. Mechanically translatable (2-40) GHz receiver module.

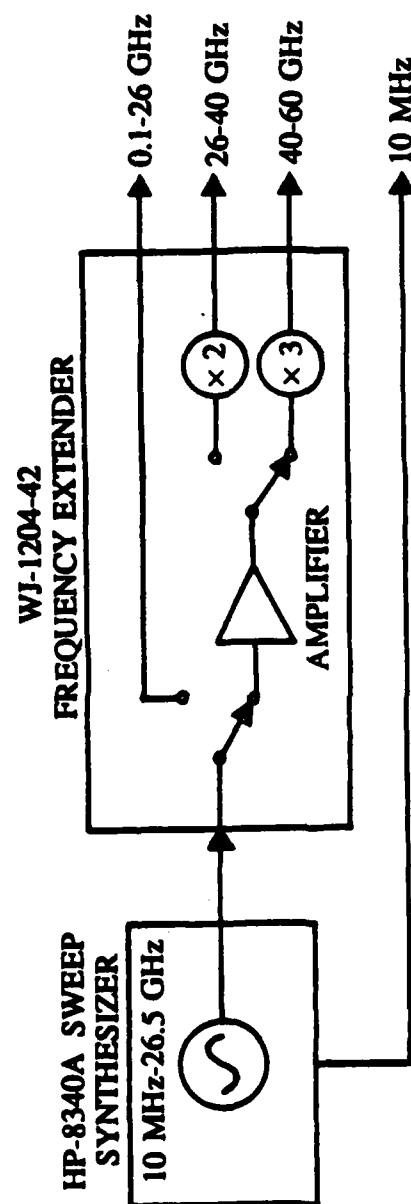


Fig. 8. Simplified schematic of the source in the transmitter assembly of Fig. 4.

The WJ-1204-42 frequency extender is in essence a frequency multiplier. It passes the RF 0.1-26.5 GHz signal from the source to one of the three output ports without much attenuation. For higher frequencies, the RF signal is amplified, then switched to either a doubler or a tripler, with the former providing frequencies in the 26.5-40 GHz range, and the latter in the 40-60 GHz range. The minimum unlevelled output power at these ports is -3 dBm at 24.0 GHz. The selection of any of the three output ports is by digital I/O, 3 bits at TTL level.

V. TRANSMITTER ASSEMBLY

A simplified schematic of the transmitter assembly is shown in Fig. 9. The transmitter assembly is a complex of power amplifiers and switches. It also provides the reference signal for the coherent detector as shown earlier in Figs. 4 and 5. The output from the WJ-1204-42 extender is fed into a bank of 5 amplifiers through proper switching. After the amplification, the major part of the signal is directed to the transmitting antenna cluster for illuminating the scattering object, while a fraction of it is extracted to provide the reference signal. The extracted signal is downconverted to below 18 GHz depending on band by a local reference at 26.5 GHz, which is generated by a local oscillator, phase-locked to the time base of the source. The downconverted signal is to be used as the reference for the coherent detector.

The antenna cluster consists of a broadband parabolic reflector (2-40 GHz, 3' diameter). Other antennas covering the 40-60 GHz band are yet to be purchased.* There are two spiral feeds for the parabolic dish, corresponding

*Unanticipated increases in the cost of several components of the system prevented the purchase of these antennas and a 26.5 GHz phase-locked local oscillator. We expect these items to be purchased from future grants in order to extend operation to 60 GHz.

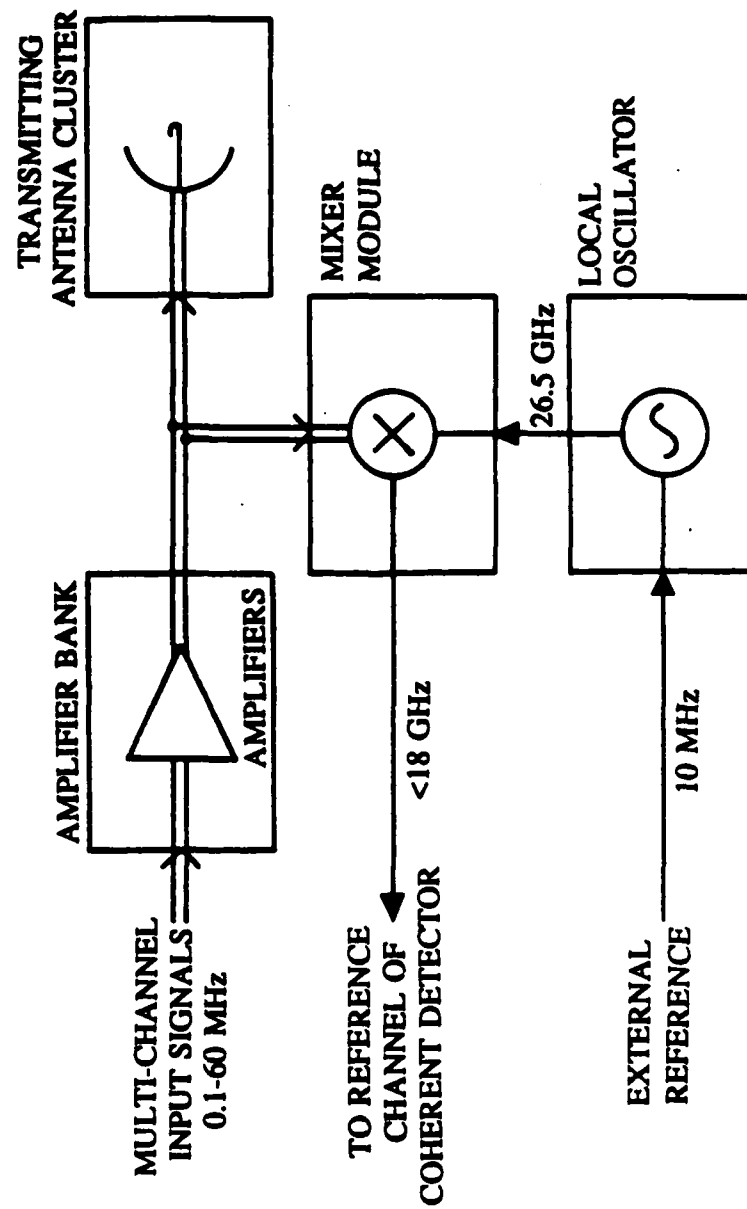


Fig. 9. Simplified version of transmitter assembly shown in Fig. 4.

to RHCP and LHCP respectively. The switching problem between the output of the amplifier bank to the transmitting antenna cluster prevents at present the complete automation of the system. The recent commercial introduction of an electronically controllable switch covering the 2 to 40 GHz band by Tektronix will alleviate this problem. Another problem is the switching of RHCP/LHCP spiral feeds. At present this can only be done manually. A Cassegrain reflector may allow mechanical rotation of the primary feeds if full automation is desirable. Even though semi-automated the present (2-60) GHz system will be of great utility.

VI. RECEIVER ASSEMBLY

The receiver assembly or module is encased in a box (see Figs. 6 and 7), and will be attached to the end of the retractable z-coordinate boom of the x,y,z, θ , ϕ positioner. In addition to the translational movement, the receiver module can be steered angularly to aim the antenna main beams towards the test object. Shown in Fig. 10 is a simplified schematic of the receiver assembly. The front end of the receiver assembly is a cluster of seven horn antennas; one dual-polarizer horn for the 2-18 GHz band, one pair of horns of opposite circular polarization for the 18-26.5 GHz band, and another similar pair for 26.5-40 GHz, and finally a pair of standard gain horns for 40-60 GHz where at present only linear polarization measurements can be conducted. Immediately following the antennas are polarization switches to control the polarization component of the scattered field to be received. The received signal is then amplified to get sufficient power for downconversion to within 18 GHz. A local oscillator, phase-locked to the reference oscillator source time base, provides the 26.5 GHz reference signal

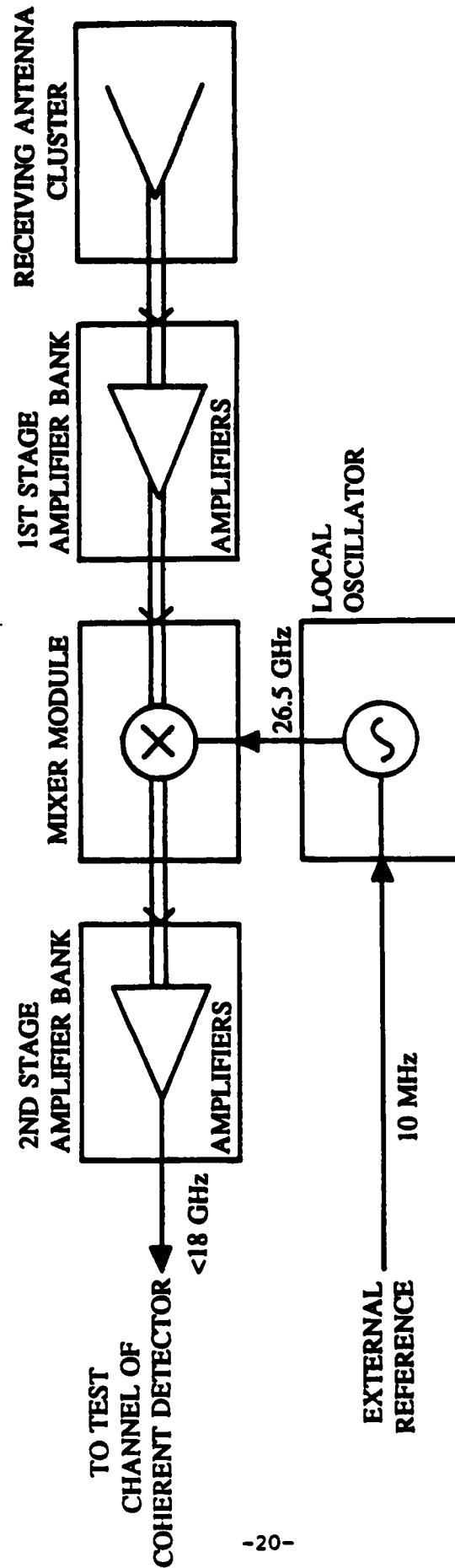


Fig. 10. Simplified version of receiver assembly shown in Fig. 6.

for the mixers. After the downconversion, the signal is passed to the second stage amplifier bank before being relayed by a flexible cable to the coherent detector. The receiver module is therefore translatable and angularly steerable to enable carrying out multistatic measurements.

VII. COHERENT DETECTOR

The coherent detector is the HP-8510A network analyzer system with the HP-8513 reflection/transmission test set. For our purpose, the measurement parameter is set to measure S_{21} , with reference channel input derived from the transmitter assembly and the test channel input derived from the receiver assembly. A simplified version of the receiver assembly given in Figs. 6 and 7 is shown in Fig. 10 in block diagram. A simplified block diagram of the coherent detector (network analyzer) is shown in Fig. 11. The test set acts as a first stage IF converter, downconverting all input RF signals to 20 MHz, which is also the frequency of the reference time base within the HP-8510A. There is a restriction on all signal power at the first harmonic mixers. Too much power will damage the harmonic mixers permanently, and too little will cause the phase-locked loop to lose track. The acceptable power to the mixers should not exceed -10 dBm; damage level is 16 dBm. Reference power to the mixer less than -50 dBm will not be adequate for phase-locking of the internal local oscillator. All the power is referred to the mixer inputs; there is additional 28 dB loss between the reference input and the mixer. Additional attenuation pads may have to be inserted to ensure good measurement accuracy.

The first IFs at 20 MHz enter the HP-8510A for second stage downconversion; this time down to 100 KHz. The second IFs are then sampled and processed to be placed in proper format for feeding to the digital

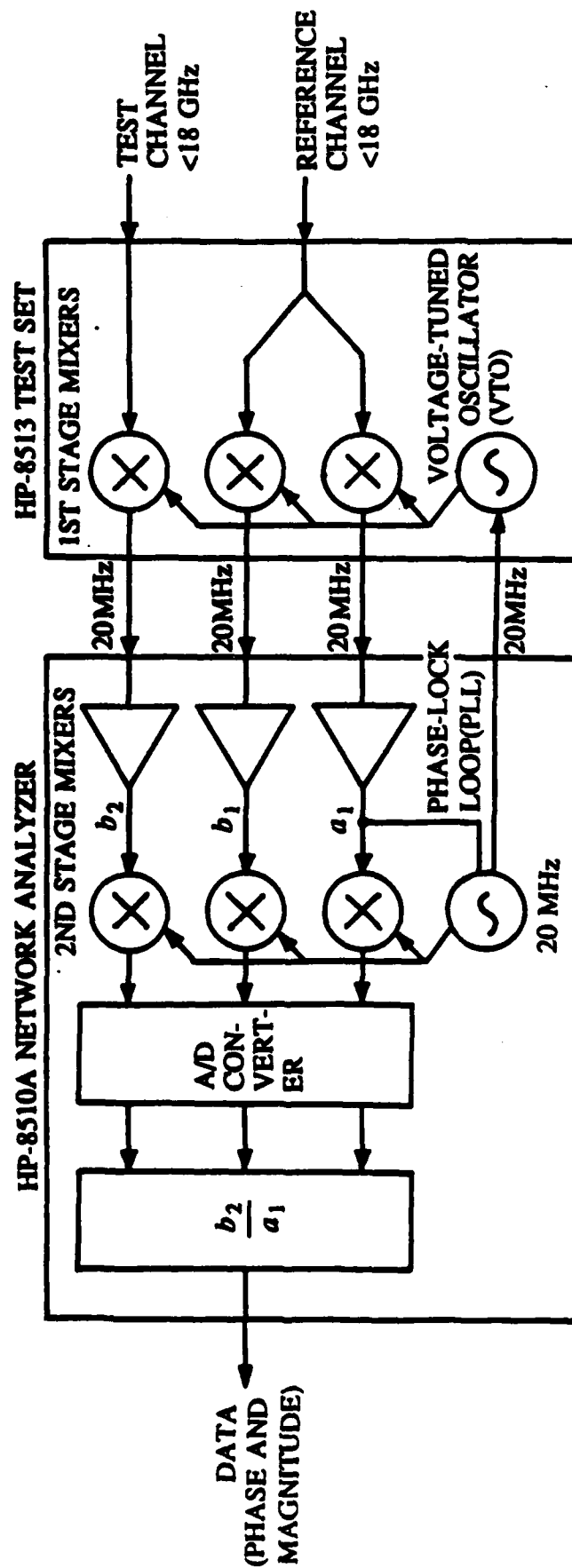


Fig. 11. Simplified schematic of the coherent detector.

phase/amplitude detector of the HP-8510A. The data are read out via the IEEE-488 GPIB, which is also the controlling bus for the HP-8510A.

For our application, the system bus connecting the HP-8510A and the source HP-8340A must be localized in order to control the HP-8340A independently. Due to this localization, some utilities encoded in the operating system of the HP-8510A cannot be used. We'll address this problem in a later section.

VIII. x,y,z, θ , ϕ POSITIONER

The positioner is designed to allow multistatic scattering measurement. To ameliorate the formidable task of having the capability of moving the receiver assembly and the transmitter assembly to arbitrary locations, we opted to provide mobility for the receiver assembly alone. The bulk of the transmitter assembly itself prohibits such mobility. The transmitter assembly is therefore stationary but additional degrees of freedom are achieved by varying the aspect angle of the scattering object. This is accomplished by mounting the test object on a computer controlled elevation over azimuth positioner. Thus the position and direction control is achieved by the combination of moving and steering the receiver assembly, and rotating the test object. A sketch of the x,y,z, θ , ϕ positioner within the anechoic chamber showing its relation to other system components was given earlier (see Fig. 2). Two parallel rails run along the length of the anechoic chamber (x direction), each 48' in length. On these parallel rails moves the transversal rails across the width of the chamber (y direction), 18' in length. A retractable boom (z direction), to the end of which is attached the receiver assembly, rides on the transversal rail, with fully extended length of 18'. There are two additional stepping motors used to

orient the elevational and the azimuthal angles (θ and ϕ) of the receiver assembly such that the antennas can be made to point toward the test object. Thus we have a total of seven stepping motors to be driven independently.

The rails are chromium-plated stainless steel shaft supported intermittently by aluminum rail supporting blocks. The rails are mounted on I-beams made of reinforced fiber glass, chosen to minimize radar cross-section and minimize reflections within the chamber. The parallel rails are attached to the wall of the anechoic chamber, with supporting blocks made of fiber glass. The transversal rails move on the parallel rails by ball-bearing pillow-block riding on stainless shafts. Similarly, the boom is attached to a platform moving on the transversal rails with ball-bearing pillow-blocks underneath. The z-coordinate collapsable boom consists of three sections of fiber glass tubing in different sizes, each section is 6' in length. The three telescoping sections contract within each other and expand under stepper motor control.

To move the positioner, a reference coordinate frame and its origin must be defined with respect to the anechoic chamber. The coordinate is chosen to coincide with the chamber frame, and the origin to be the center of the chamber or the center of rotation of the scattering object O mounted on the elevation over azimuth positioner shown in Fig. 2. Whenever the system is powered up, or before it is being turned off, the x, y, z, θ, ϕ positioner must be relocated to that origin. Therefore there must be a power-up procedure or power-off procedure to initiate the positioner. After that, the movement of the positioner and the steering of the receiving antenna are referred to the origin. Stepper motor pulse counting or mechanical or optical sensors would be incorporated in the positioner to feedback a signal to monitor the position and orientation of the receiver module. For example, by centering

the receiver module at a point representing the center of rotation of the scattering object mounted on the elevation over azimuth positioner an origin for a spherical coordinate system can be defined. The position vector of the receiver module after displacement can then be determined by computing the relative x,y, and z displacements by counting the number of calibrated steps of the x,y,z stepper motors executed to get to that point. The values of x,y and z determined in this fashion enable calculating the radial coordinate $r = (x^2 + y^2 + z^2)^{1/2}$ and the angular spherical coordinates θ' and ϕ' which enable defining the orientation θ and ϕ of the receiver module required to point it towards the object.

IX. SOME DESIGN CONSIDERATIONS

Several aspects of the measurement system design are currently being addressed. The disassociation of the source HP-8340A from the control of the HP-8510A network analyzer is necessitated by the fact that the new system must accommodate measurement at frequencies higher than the capabilities of the HP-8340A/8510A. In normal applications, the HP-8510A, running under the software provided by Hewlett-Packard Co., acts as the controller of the HP-8340A. The HP-8510A is the only instrument to be controlled by the external controller. In the new system, the frequency control of the HP-8340A is relegated from the HP-8510A internal controller to the external controller. Except for the frequency stimulus functions, the remaining utilities offered by the HP-8510A can still be used. The same situation is encountered in the HP and Hughes millimeter-wave network analyzer systems, since these systems also use HP-8510 as the key building block. The operations involving the frequency stimulus must be programmed by the user. More information may be needed from Hewlett-Packard Co. to write such a program.

In designing a network analyzer, efforts are made to maintain the attenuation and phase balance of the test channel and the reference channel. Consider our system as a network analyzer operating in transmission mode with the transmitting section as the reference channel and the receiving section as the test channel. It is ideal that the path length and the attenuation of these two channels are identical. The inequality of path length introduces linear phase difference. Different attenuation causes wrong magnitude ratio reading. Should any nonlinearity exist, e.g., phase instability or excess power in any channel, the measurement errors will be noticeable. We expect programmable power level feature of the HP 8340A synthesized sweeper used will enable precalibration of power levels through the system at different frequencies to alleviate or eliminate any nonlinearity errors.

Every component has a power handling capability such that, within a certain power range, the component is operating in its linear region. Therefore, it is essential to ensure such linear operation for each component; not only to remove nonlinear distortion, but also to use the component at its best performance. To satisfy this consideration, attenuators are inserted at various stages inside the assemblies. The price paid for achieving this is that some power is wasted and the lengths of signal paths becomes unequal. But the gain in performance sanctions such trade-in. The phase difference caused by inequality of signal paths can be eliminated by a calibration procedure which measures the total phase difference of a through connection and stores it as a calibration set, i.e., by measuring and the frequency response of the measurement system itself as was done in the original measurement system. The measurements made afterward are corrected against the calibration data set to compensate the phase

difference. The same calibration procedure can, to a certain degree, correct the residual nonlinearity and power level fluctuations within the system.

Although the design of the system has been for continuous frequency coverage from (2-60) GHz, a few small frequency gaps may exist within the overall bandwidth because of hardware limitations. The missing of these frequencies may not have significant effects on various applications.

The second stage amplification and the frequency downconversion in the receiver assembly are indispensable due to the considerable length of the flexible coaxial cable connecting the receiver assembly to the coherent detector. Flexibility is needed since the receiver assembly must be translatable for multistatic operation. To enable multistatic measurements by positioning the receiver module within the front half of the chamber a 35' coaxial cable is required. A low-loss phase stable coaxial cable must be used. An ideal attractive future alternative is to use a microwave optical fiber link when the bandwidth of such links is made to approach 18 GHz.

The actual data acquisition locations produced by the x, y, z, θ, ϕ positioner are critical in multistatic measurements, especially when frequencies in the millimeter wave range are utilized. In terms of imaging, knowledge of the exact positions where the data are taken is essential to guarantee good image reconstruction. Because of the considerable weight of the transversal rails and the boom, slight bending of the rails is inevitable. We estimate that there will be 0.6" bending in the z direction at most. It would be better if this bending can be compensated, say by retracting or extending the boom. It may become necessary to calibrate the positioner for all locations in the chamber if the position deviations turn out to be appreciably detrimental. Another aspect worth considering is the wobbling of the boom as it changes positions. Adequate time must be allowed

until the boom stabilizes before taking measurement. This would be taken into account in writing data acquisition programs.

Despite the fact that materials chosen are intended to minimize the reflection from the positioner and the receiver assembly, the effect from these reflections can be further minimized by two ways. The first method is to cover reflecting parts of the positioner, including the rails, the boom, and the receiver assembly box with appropriate broadband absorber material. The second method is to measure and store the chamber response for every positioner location on an intended scanning locus, and subtract this response from later measurements. This method may be impractical in that: firstly, the same measurement sequence has to be done twice, one for room clutter, then for test object; secondly, the accuracy, or rather the inaccuracy, of the stepping motors may prevent the positioning repeatability of the two successive measurements. The latter may nullify the very intention for clutter cancellation. A combination of both approaches may offer the best optimal solution.

X. DATA ACQUISITION PROGRAMMING

This section outlines the programming for data acquisition. As we discussed earlier, the x, y, z, θ, ϕ positioner would place itself at the origin of the chamber coordinate, the center of the chamber, before and after data acquisition. This may be done by a start-up program whose sole function is to move the positioner until it finds the chamber origin. This routine should be invoked whenever the system is started and before it is turned off.

We concentrate now on the programming for data acquisition, assuming that the start-up routine has been executed and the positioner is at the origin. Shown in Fig. 12 is the program block diagram of a typical data

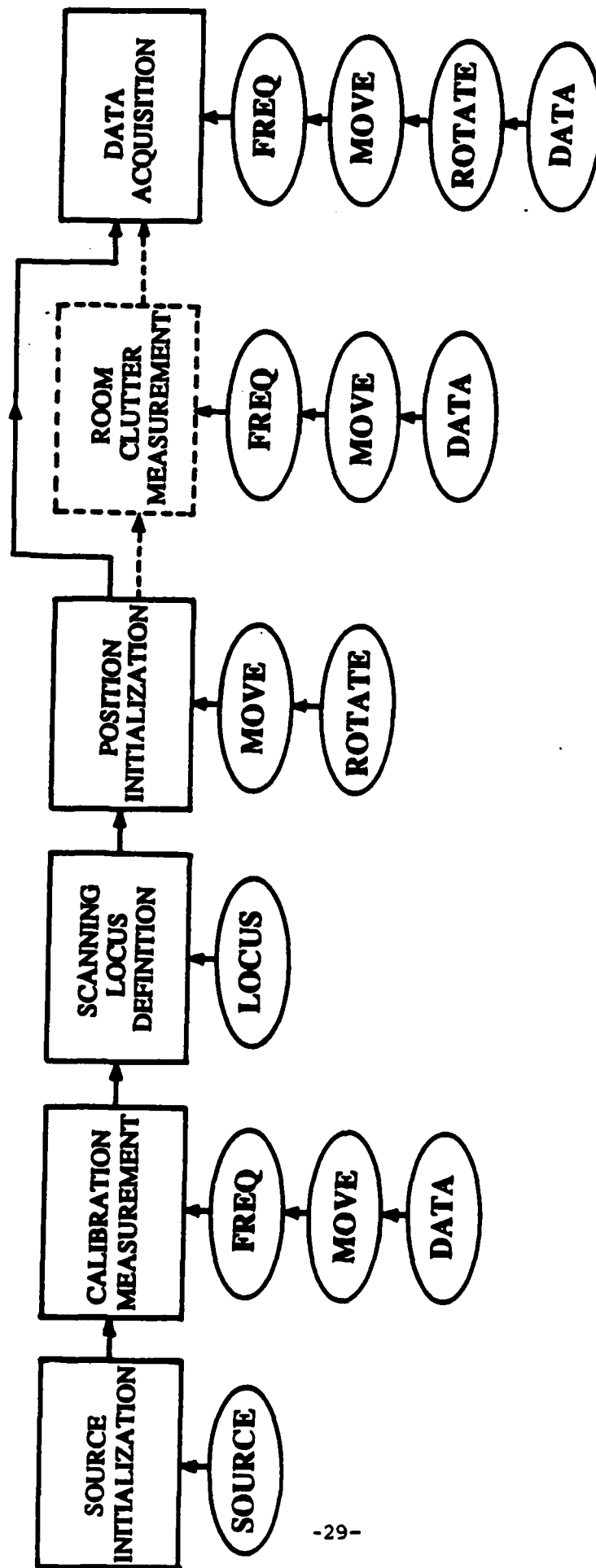


Fig. 12. Conceptual data acquisition programming flow chart.

acquisition session. Also shown below each block are the subroutines needed to perform the function of that block. The principle of modularity in programming is closely observed so that each user can tailor his own program easily using these routines as building blocks. A description of these subroutines is given next:

SOURCE

The source subroutine performs dialogue to accept frequency definitions, e.g., start and stop frequencies, number of frequency samples, power level at each frequency, etc., from the user. From these user-specified parameters, the routine initializes the source and the coherent detector, and generates the switching map for each of the cross-band switches if the frequency range involves cross-band measurement. Also the desired polarization combination is selected.

FREQ

The frequency subroutine uses the parameters generated by SOURCE to perform frequency setting of a single sweep of the specified frequency range. It not only controls the frequency setting and timing, it is also responsible for setting up the proper signal path for cross-band measurement using the switching map generated by SOURCE.

MOVE

The move subroutine controls the relative movement of the x, y, z, θ, ϕ positioner and the orientation θ, ϕ of the receiver module through the control of different stepping motors. The inputs to this routine are the distances in x, y, z directions and the elevation (θ) and azimuthal

(ϕ) angles of the receiver module. All parameters are relative, not related to the absolute coordinates of the chamber. Therefore, these parameters are pre-calculated.

DATA

The data subroutine reads the measurement of one stepped frequency sweep from the network analyzer and delivers the data to the auxiliary storage devices. The data format must be conformed to the other data processing programs.

LOCUS

The locus subroutine calculates the scanning locus of a data acquisition session. It is highly dependent on the specific locus the user intends to synthesize. It is difficult to write a subroutine that gives options for all possible loci, although some regular loci may be implemented. The key parameters to be generated in this routine are the relative changes in positions x, y, z and angles θ, ϕ given a locus definition. The locus definition includes the starting position for scanning, the number of positions, the locus equations, etc.

ROTATE

The rotate subroutine controls the rotation of the test object mounted on the pedestal in order to change its aspect relative to the stationary illuminating antenna and the mobile receiver module. This enables complete multistatic measurement to be carried out.

The aforementioned subroutines are the basic building blocks for any data acquisition program. We describe next the steps in a typical data acquisition session, illustrated in Fig. 12.

The first step is the source initialization. the SOURCE subroutine is the key routine to be called. The functions to be performed at this stage are:

- * Frequency sweep format definition: start and stop frequencies, sweep mode, sampling number.
- * HP-8340A initialization: power level, sweeping time, averaging factor.
- * HP-8510A initialization: measurement parameter S_{21} , system localization, display formats.
- * Switching map calculation for setting the signal path.
- * Selection of polarization states.

After system initialization, a calibration measurement is performed for later data correction. Two subroutines are used in this procedure:

- * Move the receiver assembly to the calibration location by the use of MOVE routine. A good choice of the calibration location is the location closest to the transmitter assembly as if in monostatic arrangement. Also the receiver assembly would be pointing towards the origin of the coordinate (e.g., center of rotation of object on elevation over azimuth positioner).
- * A reference target, a metallic sphere or a metallic cylinder, is centered at the origin of the coordinates.
- * A single frequency sweep of data is taken and stored in the HP-8510A or the computer for later correction. Subroutines used are FREQ and DATA.

After the calibration data measurement, the user enters the locus definition by the use of LOCUS subroutine as follows:

- * Scanning locus definition: starting coordinate, locus equation, and number of scanning positions.
- * Scanning position calculation. Coordinate increments of successive scanning locations are calculated.
- * Scanning angle calculation. Angular increments needed to steer the receiver module toward the object at successive scanning locations are calculated.
- * Define the test object orientation for each scanning location. This step is needed only when more complex loci is desired.

After calculating all the parameters needed, now the positioner is moved to the initial scanning location:

- * Move the positioner to the starting scanning location by the use of MOVE.
- * Rotate the test object to the initial orientation by the use of ROTATE.

The system now is ready to collect the data. The data acquisition consists of the following steps:

- * Collect one frequency sweep of data by the use of FREQ.
- * Get the data from the system and store them by the use of DATA.
- * Move to the next scanning location and orientation of the receiver module by the use of MOVE.
- * Change the object orientation as desired by the use of ROTATE.
- * Repeat the same procedure.

After the end of data acquisition, the positioner and the object are reset to their initial location and orientations.

Note that in Fig. 12, there is an intermediate step of clutter measurement. This step is essentially the same as data acquisition, except that now there is no object placed on the pedestal. The measured quantity is the aspect dependent room clutter. After clutter measurement, the positioner is moved to the initial scanning location.

XI. CONCLUSIONS

The new upgraded system possessing wavelength, polarization, and position diversity measurement capability in the (2-60) GHz range is described. The equipment and components are delineated. Many aspects of the design problems and the viable solutions to these problems are presented. The programming considerations are addressed, with a typical data acquisition session as an example. Most of the components are in hand and in a state of partial assembly. The construction and assembly of the x,y,z,θ,ϕ positioner is about 60% completed. The implementation of the system is a challenging task. However once fully operational, the system will be a unique tool in the study of multistatic scattering, polarization effects, and radar imaging modalities in the (2-60) GHz range. The system will also be invaluable in the generation of high fidelity target representations and signatures in the study and development of automated recognition schemes based on models of neural networks.

The components of the system have been chosen with multifunctionality in mind. For example the components of the frequency agile phase-locked reference oscillator in Fig. 4 can be reconfigured as shown in Fig. 13 to furnish a high-speed synthesized source for illuminating a target for rapid data acquisition that is one to two order of magnitude faster than with the hp 8340A based system.

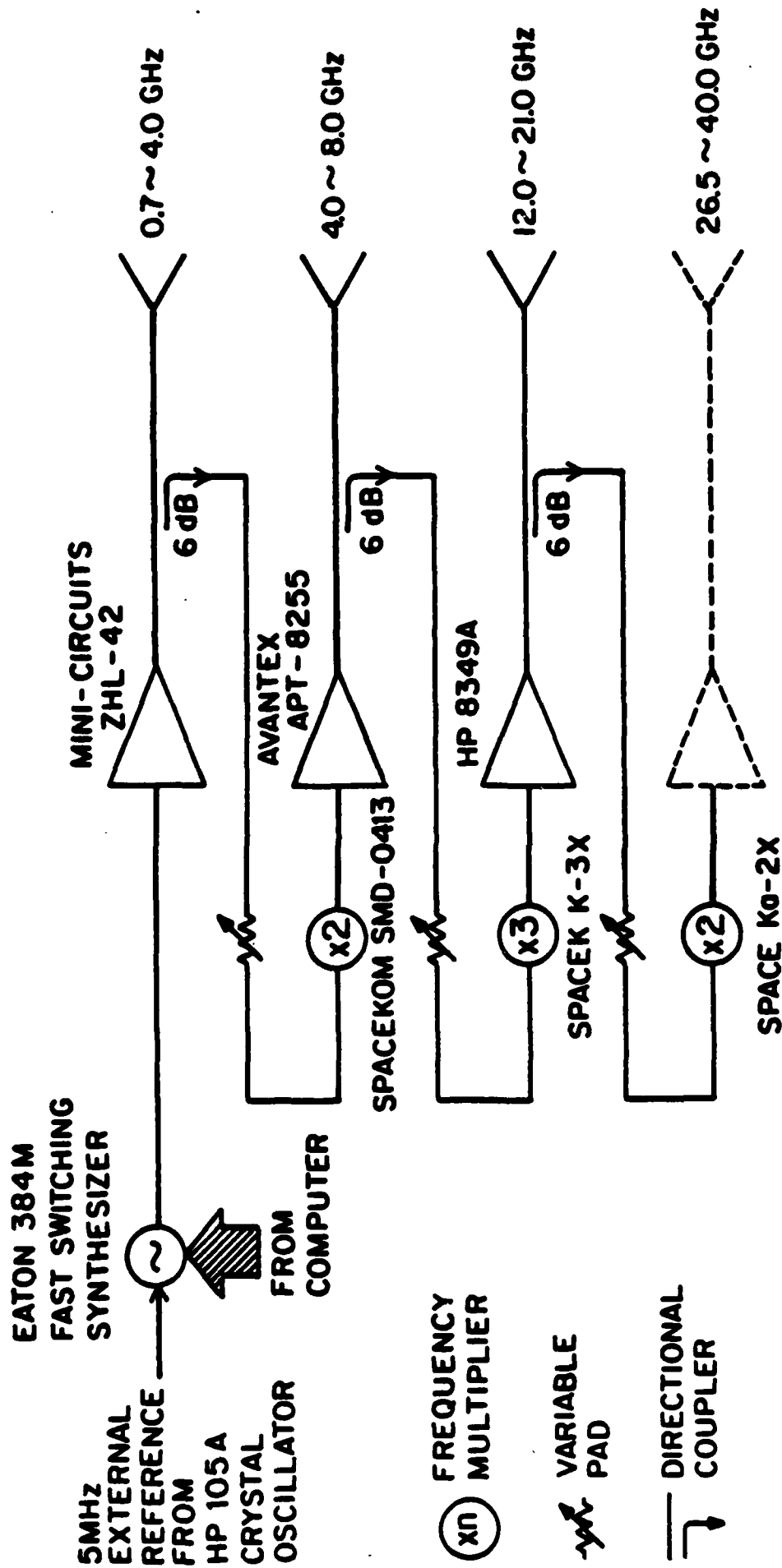


Fig. 13. Fast switching (.7-40) GHz synthesized transmitter module.

OPTICAL ANALOGS OF TWO-DIMENSIONAL NEURAL NETWORKS AND THEIR APPLICATION IN RECOGNITION OF RADAR TARGETS

N.H. Farhat, S. Miyahara and K.S. Lee
University of Pennsylvania
The Electro-Optics and Microwave-Optics Laboratory
200 S. 33rd Street
Philadelphia, PA 19104-6390

ABSTRACT

Optical analogs of 2-D distribution of idealized neurons (2-D neural net) based on partitioning of the resulting 4-D connectivity matrix are discussed. These are desirable because of compatibility with 2-D feature spaces and ability to realize denser networks. An example of their use with sinogram classifiers derived from realistic radar data of scale models of three aerospace objects taken as learning set is given. Super-resolved recognition from partial information that can be as low as 20% of the sinogram data is demonstrated together with a capacity for error correction and generalization.

INTRODUCTION

Neural net models and their analogs furnish a new approach to signal processing that is collective, robust, and fault tolerant. Optical implementations of neural nets^{1,2} are attractive because of the inherent parallelism and massive interconnection capabilities provided by optics and because of emergent optical technologies that promise high resolution and high speed programmable spatial light modulators (SLMs) and arrays of optical bistability devices (optical decision making elements) that can facilitate the implementation and study of large networks. Optical implementation of a one-dimensional network of 32 neurons exhibiting robust content-addressability and associative recall has already been demonstrated to illustrate the above advantages.³ Extension to two-dimensional arrangements are of interest because these are suitable for processing of 2-D image data or image classifiers directly and offer a way for optical implementation of large networks.⁴

In this paper we will discuss content addressable memory (CAM) architectures based on partitioning of the four dimensional T_{ijkl} memory or interconnection matrix encountered in the storage of 2-D entities. A specific architecture and implementation based on the use of partitioned unipolar binary (u.b.) memory matrix and the use of adaptive thresholding in the feedback loop are described. The use of u.b. memory masks greatly simplifies optical implementations and facilitates the realization of larger networks $\sim (10^3 - 10^4 \text{ neurons})$. Numerical simulations showing the use of such 2-D networks in the recognition of dilute point-like objects that arise in radar and other similar remote sensing imaging applications are described. Dilute objects pose a problem for CAM storage because of the small

Hamming distance between them. Here we show that coding in the form of a *sinogram classifier* of the dilute object can remove this limitation permitting recognition from partial versions of the stored entities. The advantage of this capability in super-resolved recognition of radar targets is discussed in the context of a new type of radar diversity imaging, studied extensively in our laboratory, that is capable of providing sinogram information compatible with 2-D CAM storage and interrogation. Super-resolved automated recognition of scale models of three aero-space objects from partial information as low as 20% of a learned entity is shown employing hetero-associative storage where the outcome is a word label describing the recognized object. Capacity for error correction and generalization were also observed.

TWO-DIMENSIONAL NEURAL NETS

Storage and readout of 2-D entities in a content addressable or associative memory is described next. Given a set of M 2-D bipolar binary patterns or entities $v_{ij}^{(m)}$ $m=1,2,\dots,M$ each of $N \times N$ elements represented by a matrix of rank N , these can be stored in a manner that is a direct extension of the 1-D case as follows: For each element of a matrix a new $N \times N$ matrix is formed by multiplying the value of the element by all elements of the matrix including itself taking the self product as zero. The outcome is a new set of N^2 binary bipolar matrices each of rank N . A formal description of this operation is,

$$T_{ijkl}^{(m)} = \begin{cases} v_{ij}^{(m)} v_{kl}^{(m)} & i \neq k, j \neq l \\ 0 & i = k, j = l \end{cases} \quad (1)$$

which is a four dimensional matrix. An overall or composite synaptic or connectivity memory matrix is formed then by adding all 4-D matrices $T_{ijkl}^{(m)}$ i.e.,

$$T_{ijkl} = \sum_m T_{ijkl}^{(m)} \quad (2)$$

This symmetric 4-D matrix has elements that vary in value between $-M$ to M also in steps of two as for the 1-D neural net case and which assume values of $+1$ and -1 (and zeros for the self product elements) when the matrix is clipped or binarized as is usually preferable for optical implementations. Two dimensional unipolar binary entities

$b_{ij}^{(m)}$ are frequently of practical importance. These can be transformed

in the usual way into bipolar binary matrices through $v_{ij}^{(m)} = (2b_{ij}^{(m)} - 1)$

which are then used to form the 4-D connectivity matrix or memory as described. Also, as in the 1-D neural net case, the prompting entity

can be unipolar binary $b_{ij}^{(m)}$, which would simplify further optical

implementations in incoherent light.

Architectures for optical implementation of 2-D neural nets must contend with the task of realizing a 4-D memory matrix. Here a scheme is presented that is based on the partitioning of the 4-D memory matrix into an array of 2-D matrices of rank N.

Nearest neighbor search of the memory matrix for a given entity $b_{ij}^{(mo)}$ is done by forming the estimate,

$$\hat{b}_{ij}^{(mo)} = \sum_{k,l}^N T_{ijkl} b_{kl}^{(mo)} \quad \dots i,j,k,l = 1,2,\dots,N \quad (3)$$

followed by thresholding to obtain a new u.b. matrix which is used to replace $b_{kl}^{(mo)}$ in eq. (3) and the procedure is repeated until the resulting matrix converges to the stored entity closest to the initiating matrix $b_{ij}^{(mo)}$. The operation in eq. (3) can be interpreted as first partitioning of the 4-D T_{ijkl} matrix into an array of 2-D submatrices of rank N: $T_{11kl}, T_{12kl}, \dots, T_{1Nkl}; T_{21kl}, T_{22kl}, \dots, T_{2Nkl}; \dots, T_{N1kl}, T_{N2kl}, \dots, T_{NNkl}$ as depicted schematically in Fig. 1(a) where the partition submatrices are arranged in a 2-D array. This first step is followed by multiplication of $b_{kl}^{(mo)}$ by each of the partition submatrices, on an element by element basis, and summing the products for each submatrix to obtain the first estimate $\hat{b}_{ij}^{(mo)}$. The tensor multiplications and summation operations called for in eq. (3) are carried out in Fig. 1(a) by placing a spatially integrating photodetector (PD) behind each submatrix of the partitioned

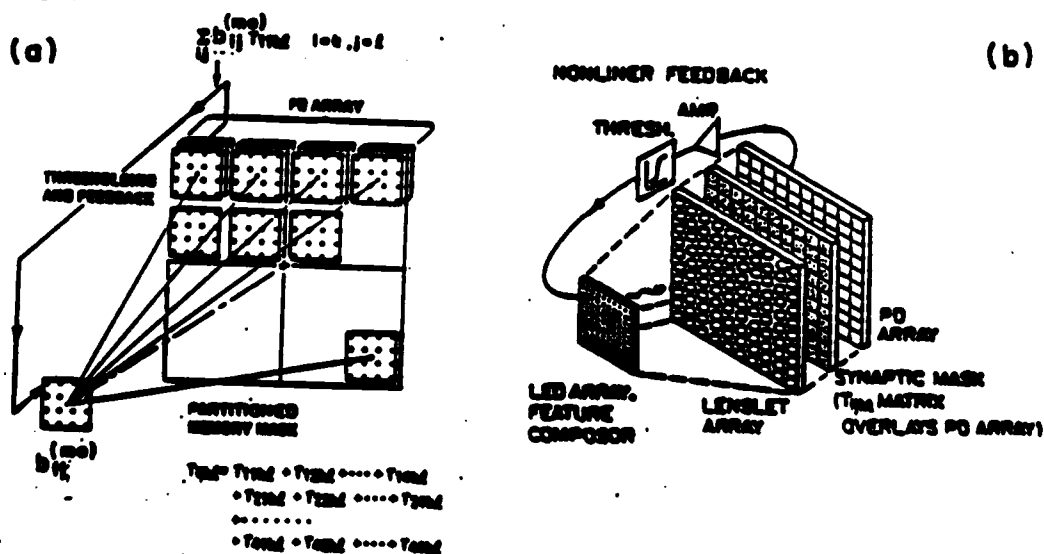


Fig. 1. Optical analog of 2-D neural net. (a) Architecture based on partitioning of connectivity matrix, (b) Opto-electronic embodiment.

memory mask which is assumed for the time being to be realized by pixel transmittance modulation in an ideal transparency capable of assuming negative transmittance values. The input entity $b_{ij}^{(mo)}$ is assumed to be displayed on a suitable LED array. The LED display of $b_{ij}^{(mo)}$ is multiplied by the ideal transmittance of each of the partition submatrices by imaging the display on each of these with exact registration of pixels by means of a lenslet array as depicted in Fig. 1(b). The output of each PD, proportional to one of the components of eq. 3, is thresholded, amplified, and fed back to drive an associated LED. The (i,j) -th LED is paired with the (i,j) -th PD. This completes the interconnection of the 2-D array of $N \times N$ neurons in the above architecture where each neuron communicates its state to all other neurons through a prescribed four dimensional synaptic or memory matrix in which information about M 2-D binary matrices of rank N (entities) have been stored distributively. The number of 2-D entities that can be stored in this fashion is $M \approx N^2/8 \ln N$, which follows directly from the storage capacity formula for the 1-D neural net case by replacing N by N^2 .

The added complexity associated with having to realize a bipolar transmittance in the partitioned T_{ijkl} memory mask of Fig. 1 can be avoided by using unipolar transmittance. This can lead however to some degradation in performance. A systematic numerical simulation study⁵ of a neural net CAM in which statistical evaluation of the performance of the CAM for various types of memory masks (multivalued, clipped ternary, clipped u.b.) and thresholding schemes (zero threshold, adaptive threshold where energy of input vector is used as threshold, adaptive thresholding and relaxation) was carried out. The results indicate that a u.b. memory mask can be used with virtually no sacrifice in CAM performance when the adaptive thresholding and relaxation scheme is applied. The scheme assumes an adaptive threshold is used that is proportional to the energy (total light intensity) of the input entity displayed by the LED array at any time. In the scheme of Fig. 1(b) this can be realized by projecting an image of the input pattern directly onto an additional PD element. The PD output being proportional to the total intensity of the input display is used as a variable or adaptive threshold in a comparator against which the outputs of the PD elements positioned behind the partitioned components of the T_{ijkl} memory mask are compared. The outcomes, now bipolar, are attenuated and each is fed into a limiting amplifier with delayed feedback (relaxation). Each limiter/amplifier output is used to drive the LED that each photodetector is paired with. It was found⁵ that this scheme yields performance equivalent to that of an ideal CAM with multivalued connectivity matrix and zero thresholding. Note that although the initializing 2-D entity $b_{ij}^{(mo)}$ is unipolar binary, the entities fed back after adaptive thresholding and limited amplification to drive the LED array would initially be analog resulting in multivalued iterates and intensity displays. However, after few iterations the

outputs become binary assuming the extreme values of the limiter. The ability to use u.b. memory matrices in the fashion described means that simple black and white photographic transparencies or binary SLMs can be used respectively as stationary or programmable synaptic connectivity masks as suggested by Fig. 1.

SINOGRAM CLASSIFIERS AND HETEROASSOCIATIVE STORAGE

Sinograms are object representations encountered in tomography^{6,7}. They are also useful as object classifiers specially when the objects are point-like and dilute⁸. Given a set of 2-D dilute objects the Hamming distances between their sinogram classifiers will be greater than the Hamming distances between the objects themselves, with both sets digitized to the same number of pixels, making it easier for an associative memory to distinguish between the sinograms⁸. Sinogram classifiers have additional advantages that enable scale, rotation, and shift invariant recognition of radar target which can not be detailed here because of limited space. A sinogram is a cartesian plot of the polar projections of object detail. For example referring to Fig. 2(a) which represents a dilute object consisting of 16 points on a 32x32 pixel grid, the distance that the projection of each point makes on the y axis as measured from the origin when the object is rotated about the origin traces a sinusoidal pattern when plotted against rotation angle as shown in Fig. 2(b). Figure 2(c) is a

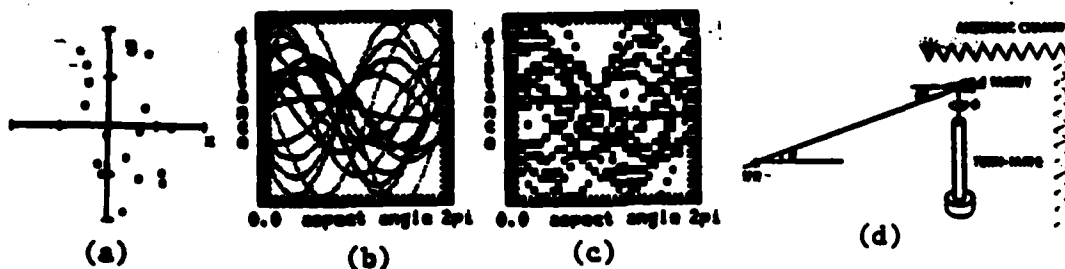


Fig. 2. Sinogram generation. (a) Sparse object, (b) Sinogram, (c) Digitized sinogram, (d) Experimental sinogram generation in radar by range-profile measurement.

digitized version of the sinogram of Fig. 2(b) plotted on a 32x32 pixel grid. The sinogram of a radar target is produced by measuring the differential range or range-profile of the target employing the arrangement of Fig. 2(d). The system basically measures, with high resolution, the differential distance (differential range or range-profile) from the rotation center of the projections of the scattering centers of the object (here scale models of aerospace targets) on the line-of-sight of the radar system. Cartesian plots of the differential distance or range-profile versus azimuthal angle of rotation ϕ results in a sinogram classifier or feature space of the target which characterizes it at any fixed elevation angle θ . The top row of Fig. 3 shows three digitized sinogram classifiers of scale models of three aerospace targets plotted on a 32x32 pixel

grid. These are treated as a learning set and stored hetero-associatively rather than autoassociatively by replacing $v_{kl}^{(m)}$ in eq. (1) by $r_{kl}^{(m)}$ $k, l=1, 2, \dots, 32$; $m=1, 2, 3$ where $r_{kl}^{(m)}$ represents abbreviated word labels shown in the bottom row of Fig. 3 with which the three test objects are to be associated.

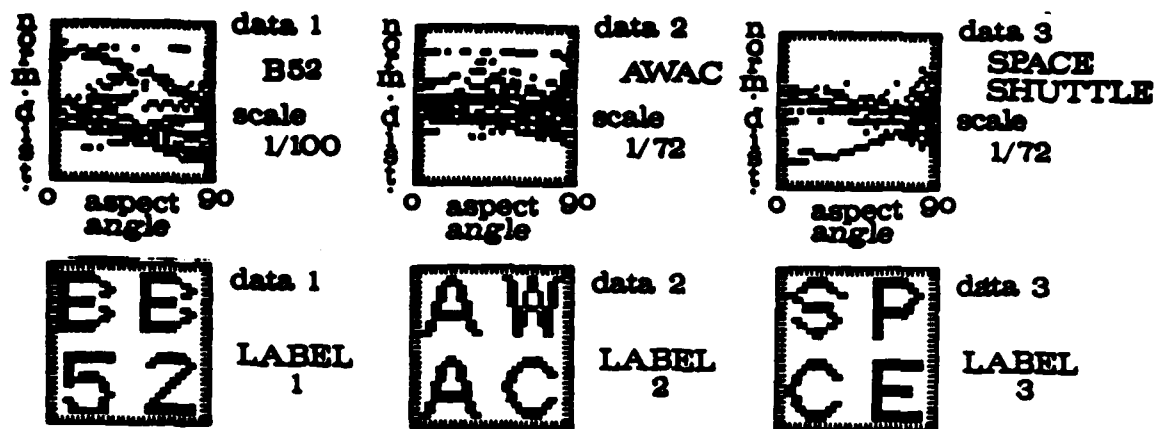


Fig. 3. Hetero-associative storage. Digitized sinograms (top) and associated word labels (bottom).

RESULTS

Representative results of numerical simulation of exercising the heteroassociative memory matrix with complete and partial versions of one of the stored entities in which the fraction η of correct bits or pixels in the partial versions ranged between 1 and .1 are presented in Fig. 4. Reliable recognition was found to occur after one iteration for all entities stored down to $\eta = .2$. For $\eta = .1$ or less successful recall of correct labels was found to depend on the angular location of the partial data the memory is presented with as illustrated in the two

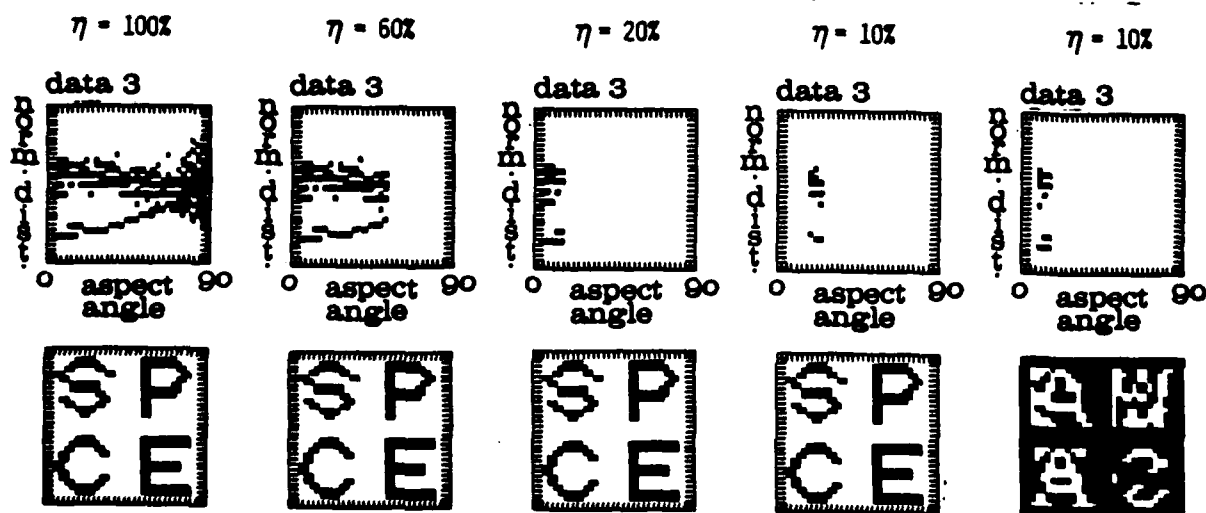


Fig. 4. Example of recognition from partial information. Complete and partial sinograms of data set 3 used as input (top), and final memory state-recognized label (bottom).

right-most examples in Fig. 4. Here the memory could not label the partial input correctly but converged instead onto a label that it did not learn before. This appears to be a generalization (mixture) of the three entities stored earlier. This is quite analogous to the generalization capability of the brain. Note the generalization is contrast reversed as we know that stable states of a memory with symmetric connectivity matrix are not only the entities stored but also their compliments.

CONCLUSIONS

Architectures for optical implementation of 2-D neural nets based on partitioning of the 4-D connectivity matrix are shown to be suitable for use with 2-D object classifiers or feature spaces. An example of their utility in super-resolved recognition (labeling) of radar targets characterized by sinogram classifiers is presented. The results show that neural net models and their opto-electronic analogs furnish a new viable approach to signal processing and automated recognition that is both robust and fault tolerant.

ACKNOWLEDGEMENT

The work described was carried out under a grant from DARPA/NRL, and partial support from AFOSR, ARO, and RCA (GE) Corporation.

REFERENCES

1. D. Psaltis and N. Farhat, Opt. Lett., 10, 98, (1985).
2. A.D. Fisher, et. al., SPIE, 625, 28 (1986).
3. N. Farhat, D. Psaltis, A. Prata and E. Paek, App. Optics, 24, 1469, (1985).
4. N. Farhat and D. Psaltis, Digest OSA Annual Meeting, Wash., D.C., p. 58, (1985).
5. K.S. Lee and N. Farhat, Digest OSA Annual Meeting, Wash., D.C., p. 48, (1985).
6. G. Herman, Image Reconstruction From Projections (Academic Press, N.Y., 1980), p. 11.
7. G.R. Gindi and A.F. Gaitro, Opt. Eng., 23, p. 499, (1984).
8. N. Farhat and S. Miyahara, Technical Digest, Spring 86 OSA Topical Meeting on Signal Recovery and Synthesis II, p. 120, (1986).

A NEW ITERATIVE ALGORITHM FOR EXTRAPOLATION OF DATA AVAILABLE IN MULTIPLE RESTRICTED REGIONS WITH APPLICATION TO RADAR IMAGING

Hsueh-Jyh Li, Nabil H. Farhat and Yuhryen Shen

The Moore School of Electrical Engineering
University of Pennsylvania
Philadelphia, PA. 19104

I. INTRODUCTION

It is well known that the resolution of microwave diversity imaging systems [1] depends on the spectral and angular (aspect related) windows utilized and on the use of polarization diversity to enhance the amount of information about a scattering object collected by a highly thinned recording aperture. To obtain the range information of the target, one can use a pulsed signal analyzed in the time domain and map thus the range profile of the target as function of aspect angle or use a broad-band CW signal analyzed in frequency domain to yield its frequency response. The range resolution is inversely proportional to the bandwidth coverage of the measurement system. The latter approach is ordinarily easier to implement. In practical situations, however, due to limitation of the measurement system or restriction of bandwidth allocation, the observed data can lie in multiple restricted spectral regions which we call pass bands. Several methods of extrapolating the measured data beyond the observed regions have been proposed and tested [2,3,4] in an attempt to achieve the full resolution of the unrestricted spectral range, when a prior knowledge of the maximum dimension of the object exists, and an iterative procedure is applied.

To increase the resolution obtained from spectral data of such limited extent, techniques of nonlinear power spectrum estimation have been used with notable success [5]. These include autoregression (AR), linear prediction (LP), and maximum entropy method (MEM). For a stationary Gaussian process, the above methods can be shown to be equivalent [5].

Although the spectra estimated by MEM or AR can be very sharp and well resolved, this may not be to advantage in a microwave imaging system. If the data are not sampled densely enough in the spectral domain as the sharp well resolved component may be missed, and the results may not reflect faithfully the actual spectral amplitudes. Besides, image reconstruction from microwave diversity imaging systems involves coherent superposition of the data in the spectra, or range profiles, of the scatterer (obtained at different looks or aspect angle), where these are estimated from partial data available in segmented bands [1]. If the estimated amplitudes of the range profiles obtained by MEM or AR depart from the desired values because of undersampling, image degradation will result. Therefore, to overcome the dense sampling requirement, it may be preferable to extrapolate the data available in the various pass bands into the vacant bands before the spectra or range profile are formed, and image reconstruction is undertaken.

If one wishes to predict the next value in a sequence on the basis of previous samples, one can use the linear prediction model which consists of finding the parameters that minimize the summation of prediction error energies which will be defined in the later section. To extrapolate the data beyond the observed region, an intuitive way is to predict the exterior data by using the same parameters obtained by the linear prediction model. The most popular approach for linear prediction parameters estimation with N data samples is the Burg algorithm [5,6]. For a given number of data samples in a given observation interval, in order to separate the discrete spectra (in this paper, spectrum is defined as the Fourier transform of the observed data), the required model order in the linear prediction method increases as the separation of spectra decreases, i.e., it is easier to model the data sequence for spectra with larger separation than those with closer separation, which translates into well separated scattering centers. In addition, for a given model order and given number of sampling points, it is easier to distinguish the two close spectra components (scattering centers) by a data set with longer observation interval than that by a data set with shorter observation interval. It was also suggested that the model order should not exceed half of the number of data points

for short data segment because otherwise the linear prediction spectral estimate will exhibit spurious peaks [5]. From the above observations, one can conclude that it would be more difficult to resolve two closer point targets (Fourier transform of the observed data in frequency domain) with short data band. If all the observed data within multiple restricted regions can be fully utilized, better resolution can be expected.

It is known that the linear prediction method is especially suited for those cases when the spectra are in discrete type. Under high frequency condition, the scattered fields of a complex target can be ascribed to a few discrete scattering centers and edge diffractions. It will be shown that under the high frequency approximation the locations of the scattering centers and their scattering strengths are independent of the operating frequency for a given transmitter/receiver pair. These phenomena provide the motivation to investigate a new method for extrapolation of scattered field data available in multiple restricted frequency bands.

In this paper, a new iterative algorithm which uses the Burg algorithm to find the linear prediction parameters and an iterative method to modify the prediction parameters is proposed and tested with both simulated and realistic measured data generated in our anechoic chamber experimental microwave imaging and measurement facilities. With this algorithm, one can obtain acceptable extrapolation beyond the observed region if the spectra are in discrete forms and the separation of the spectra are not too close. Both simulation and experimental results are presented to demonstrate as an example the effectiveness of the method in microwave diversity radar imaging.

II. THE NEW ITERATIVE ALGORITHM

The most popular approach to linear prediction parameter estimation with N data samples $\{x_1, \dots, x_N\}$ was introduced by Burg [6]. The linear prediction parameters are obtained by minimizing the sum of the forward and backward prediction error energies e_p ,

$$e_p = \sum_{n=p}^{N-1} |e_{pn}|^2 + \sum_{n=p}^{N-1} |b_{pn}|^2, \quad (1)$$

subject to the constraint that the prediction parameters satisfy a recursion relationship [5], where e_{pm} is the forward prediction error with model order p and is given by

$$e_{pm} = \sum_{k=0}^p a_{pk} x_{n-k}, \quad (2)$$

and b_{pm} is the backward prediction error with model order p and is given by

$$b_{pm} = \sum_{k=0}^p a_{pk}^* x_{n-p+k}. \quad (3)$$

a_{pk} are called linear prediction parameters, and asterisk denotes the complex conjugate operation.

If one is going to extrapolate from the available data beyond the observed region, a straight forward way is to use the estimated prediction parameters \hat{a}_{pk} and the measured data by the following equations,

$$\hat{x}_{N+j} = \sum_{k=1}^p \hat{a}_{pk} x_{N+j-k} \quad j > 0; \quad (4)$$

$$\hat{x}_{-j} = \sum_{k=1}^p \hat{a}_{pk}^* x_{-j+k} \quad j > 0, \quad (5)$$

where the $\hat{}$ denotes the estimated value.

If the data available are confined to multiple separate spectral regions or pass-bands of equal width as illustrated in Fig. 1, and one tries to extrapolate from the observed data to the vacant bands, an intuitive method is to divide the inner vacant band into two parts of equal width and to extrapolate into the left part by using the prediction parameters obtained from the data set of region I and extrapolate into the right part by using the model parameters obtained from the data set of region II.

If the data sequence can be correctly expressed by the prediction parameters, then the extrapolation error, which is defined as the absolute value of the complex difference between the theoretical values and extrapolated values, would be very small. However, if the prediction parameters cannot model the sequence correctly, the error of extrapolation may accumulate.

We have found that the longer the available data string, the larger the model order, the linear prediction model which characterizes the data sequence would be more accurate especially in the presence of noise. However, the model order should not exceed half of the number of the samples because the estimated spectrum will produce spurious peaks [5].

In order to utilize the information available in different regions, a new iterative algorithm using the Burg algorithm to estimate the prediction parameters and a new iterative method is proposed. The procedure illustrated in Fig. 2 is as follows:

1. Divide the inner vacant band into two parts of equal width. Extrapolate into the left part by using the prediction parameters obtained from the data set of region I and extrapolate into the right part by using the prediction parameters obtained from the data set of region II. If the bands are not equal in width, unequal division of the vacant intervening bands may be appropriate.
2. With the "vacant band"s' data together with the observed data, use the Burg algorithm to find a new set of prediction parameters.
3. Using this set of prediction parameters and the data of region I, extrapolate into the left part of vacant bands, and using the same set of prediction parameters and the data in region II, extrapolate into the right part of the vacant bands.
4. Using this set of parameters together with the extrapolated data, estimate the data in the observation region I and II. Calculate the error energy between the measured data and the estimated data in the observation regions. The error energy is denoted by E_1 and is given by:

$$E_1 = \sum_i |x_i - \hat{x}_i|^2 + |x_i - \hat{x}'_i|^2 = \sum_i |e_i|^2 + |b_i|^2, \quad (6)$$

where x_i are the measured data, \hat{x}_i are the forward estimation of x_i , \hat{x}'_i are the backward estimation of x_i , e_i is the forward prediction error, and b_i is the backward prediction error.

5. With the measured data together with the estimated "vacant band"s' data, use the Burg algorithm to find a new set of prediction parameters. From the measured data and this new set of prediction parameters, extrapolate the "vacant band"s' data as described in step 3.
6. Use the same procedure of step 4 to calculate the new error energy of the pass-bands, call it E_2 .
7. Compare E_1 with E_2 , if E_2 is smaller than E_1 , replace the error energy E_1 by E_2 , repeat step 5.
8. If E_2 is greater than E_1 , stop the iteration, and take the extrapolated data of the previous loop as the final result.

In step 1, if the width of a single band (band I and/or band II) is not large enough, the extrapolation errors produced by the prediction parameters obtained from single pass-band data may be very large, in that case, we can set the data in the vacant bands to zero.

The above iterative method can be easily applied to the case where only one single data band is available to extrapolate outside it. The procedures are almost the same except that only one data band sequence is used to extrapolate to the exterior bands and to calculate the extrapolation errors.

III. SCATTERING PROPERTIES OF A METALLIC OBJECT

In this section we shall show that under the high frequency approximation the scattered fields of a metallic object can be expressed as superposition of scattered fields of discrete scattering centers. These phenomena allow us to apply the proposed extrapolation algorithm to radar imaging.

For a metallic object large compared with wavelength, the scattering mechanism can be divided into the following components [7]:

1. Specular scattering points
2. Scattering from surface discontinuity: edges, corners, tips etc.
3. Scattering from surface derivative discontinuities
4. Creeping waves
5. Traveling waves
6. Scattering from concave regions
7. Multiple scattering points

For most situations, the major contributions to the scattered waves are ascribed to the specular scattering points and edge diffractions.

Consider a metallic object seated on a rotated pedestal and illuminated by a plane wave as shown in Fig. 3. The distance between the rotation center O and the transmitter and receiver are R_t and R_r , respectively, and the unit vectors in the direction of transmitter and receiver are \hat{l}_t and \hat{l}_r , respectively. Under the physical optics and Born approximations, the scattered fields at the receiver under far field condition can be expressed as [1]

$$\vec{E}_s(k) = \frac{jk}{2\pi R_r} e^{-jkR_r} \int_{S_{ill}} 2\hat{n}(\vec{r}') \times \vec{H}_0(k) e^{jk[(\hat{l}_r - \hat{l}_t) \cdot \vec{r}']} dS', \quad (7)$$

where k is the wave number, S_{ill} the illuminated region, $\hat{n}(\vec{r}')$ the unit normal vector at the surface point \vec{r}' , and $\vec{H}_0(k)$ the incident magnetic field at the rotation center.

As k approaches infinity, the asymptotic expression of the above equation can be obtained by applying the stationary phase method [8] to eq. (7). The result is,

$$\vec{E}_s(k) = \frac{jk}{2\pi R_r} e^{-jkR_r} \sum_j \frac{\sqrt{2\pi}}{k\sqrt{S_j}} 2\hat{n}(\vec{r}'_j) \times \vec{H}(k) e^{jk[(\hat{l}_r - \hat{l}_t) \cdot \vec{r}'_j]} \quad (8)$$

where \vec{r}'_j are the vectors such that

$$\left. \frac{d[(\hat{l}_r - \hat{l}_t) \cdot \vec{r}']}{da'} \right|_{\vec{r}' = \vec{r}'_j} = 0, \quad (9)$$

and

$$S_j = \frac{d^2 [(\hat{l}_r - \hat{l}_t) \cdot \mathcal{P}']}{da'^2} \Big|_{\mathcal{P}' = \mathcal{P}'_j} \quad (10)$$

where $\frac{d}{da'}$ is the derivative with respect to the surface curvature. The points \mathcal{P}'_j corresponding to the solutions of eq. (9) are called stationary points or equi-phase points or the scattering centers; the term $\hat{A}(\mathcal{P}'_j) \times \hat{H}_0(k) / \sqrt{S_j} = \alpha_j$ is called the scattering strength for the particular scattering center at \mathcal{P}'_j . It is seen that the locations of the scattering centers depend on the directions of \hat{l}_r , \hat{l}_t as well as the shape of the metallic surface. The scattering strength depends on the local properties of the scattering centers. The above analysis illustrates that the object function we would be dealing with in high frequency radar imaging are of discrete form consisting of point scattering centers.

If the received scattered fields have been calibrated with a reference target [1], the corrected fields $\hat{E}'_s(k)$ can be expressed as

$$\hat{E}'_s(k) = \sum_j \alpha_j e^{jk[(\hat{l}_r - \hat{l}_t) \cdot \mathcal{P}'_j]} \quad (11)$$

The Fourier transform of eq. (11) will give the range profile and scattering strength of the scattering centers.

IV. RESULTS

In this section, the performance of the proposed new algorithm using both simulated and realistic data will be evaluated. First, assume for simplicity an object consisting of n point scatterers located at $(r_o + y_j)$ is illuminated by a plane wave, where r_o is the distance between the transmitter/receiver and a reference point of the object and y_j is the differential range of the j th scatterer (range relative to r_o). Under far field condition and ignoring multiple scattering, and considering for simplicity a scalarized version of eq. (11), the corrected scalar field can be expressed as

$$\hat{E}'_s(k) = \sum_j a_j e^{j2ky_j} \quad (12)$$

In the following simulation, the theoretical values of $E'_s(k)$ are calculated in 200 equally spaced frequency steps covering the frequency range $f_1 = 6$ GHz to $f_{200} = 16$ GHz, with an assumed signal to noise ratio set to 40 dB. These values anticipate the realistic experimental data utilized in testing the algorithm.

Assume the available (computed) data are in the following pass-band (f_{30}, f_{80}) and (f_{120}, f_{170}) . We want to extrapolate the data to the vacant bands (f_1, f_{29}) , (f_{81}, f_{129}) , and (f_{171}, f_{200}) . The range resolution obtained by the DFT method using the whole bandwidth (f_1, f_{200}) is about 1.5 cm. The resolution using a single frequency band is about 5.5cm. The resolution using both frequency bands is about 2.0 cm, however, very high side-lobe level will be produced. We consider a scatterer with seven point scatterers, the location and scattering strength for each point scatterware $(r_1 = -30$ cm, $a_1 = 0.5)$, $(r_2 = -20$ cm, $a_2 = 0.5)$, $(r_3 = -10$ cm, $a_3 = 0.5)$, $(r_4 = -2$ cm, $a_4 = 1)$, $(r_5 = 10$ cm, $a_5 = 0.25)$, $(r_6 = 20$ cm, $a_6 = 0.25)$, $(r_7 = -30$ cm, $a_7 = 0.25)$. The values of the field at each sampled frequency f_j are calculated using eq. (12).

Define the extrapolation error at frequency f_j as

$$e(f_j) = |E'_s(f_j) - \hat{E}'_s(f_j)|, \quad (13)$$

where $\hat{E}'_s(f_j)$ is the extrapolated value at each f_j . The extrapolation errors for different algorithms are compared and shown in Fig. 4(a). The bold solid curve is the amplitude of the theoretically computed fields $E'_s(f_j)$, the thin solid curves are the extrapolation error after 100 iterations using the algorithm proposed in [3], the dashed curves are obtained by using the Burg algorithm to find the prediction parameters from the respective pass-band, and using this set of parameters together with data in each pass-band to extrapolate to the outside regions (bands III and IV). The dotted line curves are obtained using this new algorithm with one iteration and with model order 25. The algorithm proposed in [3] involves basically application of the Gerchberg algorithm to data in the multiple restricted regions. However, no numerical or experimental results are given in that paper. It is clear from the results obtained

here that the algorithm in [3] seems not to be effective in the case considered as the errors can exceed the amplitude of the theoretical fields. Extrapolation from single pass-band are not good in this example, because the model order is not sufficient to model the data series in the presence of noise. The proposed new method after one iteration is seen to produce small error.

The Fourier transform (FT) of the all-band data (i.e, data in region I to IV), pass-band data only, pass-band plus extrapolated data using the algorithm in [3] and pass-band plus extrapolated data with the new proposed method are shown in Fig. 4(b) to 4(e) respectively. Note that the FT of spectral data yields range profile of the scattering object. It is clear that FT using pass-band data only (Fig. 4(c)) has very high side-lobe structure, the FT of the extrapolated data using the algorithm in [3] (Fig. 4(e)) is totally different from the original of Fig. 4(b). The result obtained by Fourier transforming the data generated by the proposed algorithm is shown in Fig. 4(d) which exhibits excellent agreement with the all-band result of Fig. 4(b). The magnitudes of the peaks in Figs. 4(b) and 4(d) depart from the original assigned values because of zero padding used in the fast Fourier transform (FFT) algorithm. This lack of fidelity in scattering strength reconstruction does not have a discernible degrading effect on the quality of image reconstructed as will be illustrated below, but is important and must be dealt with when quantitative analysis of scattering strengths is needed.

If the frequency coverage is increased to ($f_1 = 6$ GHz, $f_{200} = 20$ GHz) with the number of sampling points being fixed to 200 and the pass-bands are kept at (f_{30}, f_{80}) and (f_{120}, f_{170}), the computed fields and the extrapolation errors would be as shown in Fig. 5. It is seen that the extrapolation error indicated by the dashed line becomes smaller. If the frequency coverage is decreased to ($f_1 = 6$ GHz, $f_{200} = 12$ GHz), the results would be as shown in Fig. 6. It is seen that the extrapolation errors indicated by the dashed and dotted curves are now both high. The FFT of the whole band data, pass-band data only, and the extrapolated plus pass-band data using this method are shown in Figs. 6(b) to 6(d) respectively. The results in Figs. 5 and 6 indicate the desirability of using segmented spectral data spanning wider spectral ranges.

The performance of the algorithm using realistic data is also evaluated. The test object, a metalized 100:1 scale model of a B-52 aircraft with 79 cm wing span and 68 cm long fuselage was mounted on a computer-controlled elevation-over-azimuth positioner situated in an anechoic chamber environment. 201 equal frequency steps covering the $f_1 = 6.1$ to $f_{201} = 17.5$ GHz range were used to obtain the frequency response of the object as described in [1]. The target is positioned for a fixed elevation angle of 30° while the azimuth angle was altered between 0° and 90° in steps of 0.7° for a total of 128 angular looks.

The pass-band is first defined as (f_{30}, f_{90}) and (f_{120}, f_{170}) . The measured values and the extrapolated errors of the broad-side look which is 90° from the head-on look are shown in Fig. 7(a). The solid line curve is the amplitude of the range-phase corrected field (see [1]). The dashed curve represents the extrapolation error resulting from extrapolating from each single band (bands I, II) with model order 25 as described in step 1 of the proposed algorithm. The dotted line curves are obtained using the new algorithm with 1 iteration and model order 25. The extrapolation error for measurement is defined in a manner similar to the definition of error in numerical simulation as the magnitude of the difference between the corrected measured fields and extrapolated fields. The Fourier transform from the whole band data, the pass-band data only, and the pass-band together with extrapolated data are shown in Figs. 7(b), 7(c) and 7(d) respectively. Fourier transform of the corrected scattered fields will give the range profile of the target in that view. In this figure, it is seen that the extrapolation errors do not improve after one iteration. The reason can be explained from the plot of the range profile shown in Fig. 7(b). In this view direction, the major contributions to the scattered fields are due to fuselage and primarily those engines and fuel tank which are on the illuminated side. Specular scattering from these points are well separated in time or distance and their number is small. Hence the linear prediction parameters obtained from single pass-band are sufficient to model the data sequence. The extrapolation errors are not as small as those obtained by simulations. The reason of this is that the applicability of linear prediction model to the extrapolation of scattered fields of a metallic object is based on the high

frequency approximation. In the measurement data, however, polarization effects, edge diffraction, multiple scattering and the failure to satisfy the high frequency approximation in the lower region of the frequency band utilized in the measurement will degrade the performance of the algorithm.

The reconstructed images of the test object using data collected in an angular windows of 90° extending from head-on to broadside in 128 looks (see [1] for detail) and different frequency bands are shown in Fig. 8. The transmitting antenna is right-hand circularly polarized and the receiving antenna is left-hand circularly polarized, which constitutes by the convention given in [7] a co-polarized transmitting/receiving system. Figure 8(a) is obtained by using the whole band data; Fig. 8(b) is obtained by using the pass-band data alone. Figures 8(c) and 8(d) are obtained by extrapolating without iteration and after one iteration respectively. The model order used is $M = 25$ in both cases.

If the pass-band is defined as (f_{65}, f_{130}) , the reconstructed images obtained by using the pass-band data alone and by extrapolation without iteration and after 1 iteration are shown in Figs. 8(e), 8(f), and 8(g) respectively. The model order used is also $M = 25$.

It is seen that the image quality of Figs. 8(c) and 8(e) are as good as that of Fig. 8(a). These results show the effectiveness of the application of the proposed algorithm to radar imaging from segmented data bands.

V. CONCLUSION

A new method employing the Burg algorithm and an iterative procedure to extrapolate observed data beyond restricted regions of observation has been proposed and tested. Simulation and experimental results prove the effectiveness of this proposed method. The algorithm is especially effective when the spectra of the collected data (the object range profile in this case) are in discrete form. Possible applications of this new method can be found in diverse fields whenever the data is available in restricted bands. For example, in multiple band microwave imaging system, the quality of the image obtained by extrapolating from a much

smaller bandwidth can be as good as that obtained by data in the full bandwidth. The cost of the imaging system can hence be reduced drastically as the cost of the required gear can be much lower than the cost of the gear to cover the full bandwidth and restrictions on use of frequency bands can be accommodated.

ACKNOWLEDGEMENT

This research was supported by the Air Force Office of Scientific Research, Air Force system Command, under grant AFOSR-81-0240F and by the Army Research Office under contract DAAG 29-83-K-0120-P02.

REFERENCE

- [1] N.H Farhat, C.L. Werner and T.H. Chu, "Prospects for Three-Dimensional Projective and Tomographic Imaging Radar Networks," *Radio Science*, Vol. 19, No. 5, pp. 1347-1355, 1984.
- [2] R.W. Gerchberg, "Super-Resolution Through Error Energy Reduction," *Optica Acta*, Vol. 21, No. 9, pp. 708-720, 1974.
- [3] Yoshiki Yamakoshi and Takuso Sato, "Iterative Image Restoration From Data Available in Multiple Restricted Regions," *Applied Optics*, Vol. 21, No. 24, pp.4473-4480, 1982.
- [4] C.Q. Lan, K.K. Xu and Glen Wade, "Limited Angle Diffraction Tomography and Its Application to Planar Scanning Systems," *IEEE Trans. on Sonics and Ultrasonics*, Vol. SU-32, No. 1, pp. 9-16, 1985.
- [5] Steven M. Kay and Stanley Lawrence Marple, "Spectrum Analysis - A Modern Perspective," *Proc. of the IEEE*, Vol. 69, pp.1380-1419, November 1981.
- [6] Burg, John P., "A New Analysis Technique for Time Series Data", NATO Advanced Study Institute on Signal Processing with Emphasis on Underwater Acoustics, pp. 12-23, August 1968.
- [7] G. T. Ruck, *et al.*, *Radar Cross Section Handbook*, edited by G. T. Ruck, Chapter 8, Plenum Press, New York 1970.
- [8] Jon Mathews and R.L. Walker, *Mathematical Methods of Physics*, 2nd Ed., W.A. Benjamin, Inc., Menlo Park, California, 1970.

FIGURE CAPTIONS

Fig. 1 Available data in multiple regions. Passband(shaded region) surrounded by vacant bands.

Fig. 2 Schematic diagram of the proposed new iterative extrapolation method.

Fig. 3 Geometry of the scattering measurement system.

Fig. 4 (a) Magnitude of theoretical fields and comparison of extrapolation errors of different methods, $f_1 = 6$ GHz, $f_{200} = 16$ GHz.

——— magnitude of theoretical fields.

——— extrapolation error from a single passband, no iteration.

..... extrapolation errors from new iterative algorithm.

——— extrapolation errors from algorithm proposed in [3].

(b) FFT of the whole band data.

(c) FFT of the passband data.

(d) FFT of the passband and extrapolated data with 1 iteration.

(e) FFT of the passband and extrapolated data using algorithm proposed in [3].

Fig. 5 Magnitude of theoretical fields and comparison of extrapolation errors with and without iteration, $f_1 = 6$ GHz, $f_{200} = 20$ GHz.

——— magnitude of theoretical fields.

——— extrapolation error from respective passband, no iteration.

..... extrapolation errors from new iterative algorithm.

Fig. 6 (a) Magnitude of theoretical fields and comparison of extrapolation errors with and without iteration, $f_1 = 6$ GHz, $f_{200} = 12$ GHz.

- magnitude of theoretical fields.**
 - extrapolation error from respective passband, no iteration.**
 - extrapolation errors from new iterative algorithm.**
- (b) FFT of the whole band data.**
- (c) FFT of the passband data.**
- (d) FFT of the passband and extrapolated data with 1 iteration.**

Fig. 7 (a) Magnitude of the measured fields and comparison of extrapolation errors without and with 1 iteration

- magnitude of theoretical fields.**
 - extrapolation error from respective passband, no iteration.**
 - extrapolation errors from new iterative algorithm.**
- (b) FFT of the whole band data.**
- (c) FFT of the passband data.**
- (d) FFT of the passband and extrapolated data with 1 iteration.**

Fig. 8 Reconstructed images of the metalized scale model B-52 aircraft using an angular window of 90° extending from head-on to broad-side in 128 looks and different spectral coverage.

Reconstructions from:

(a) entire bandwidth (f_1, f_{201}).

(b) passband (f_{30}, f_{80}), (f_{120}, f_{170}).

(c) passband (f_{30}, f_{80}), (f_{120}, f_{170})

and extrapolation data (extrapolated data into empty bands) without iteration.

(d) passband (f_{30}, f_{80}), (f_{120}, f_{170})

and extrapolation data with 1 iteration.

(e) passband (f_{65}, f_{130}).

(f) passband (f_{65}, f_{130}) and extrapolation data without iteration.

(g) passband (f_{65}, f_{130}) and extrapolation data with 1 iteration.

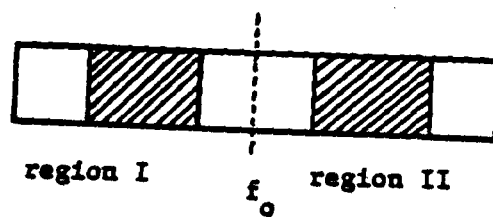
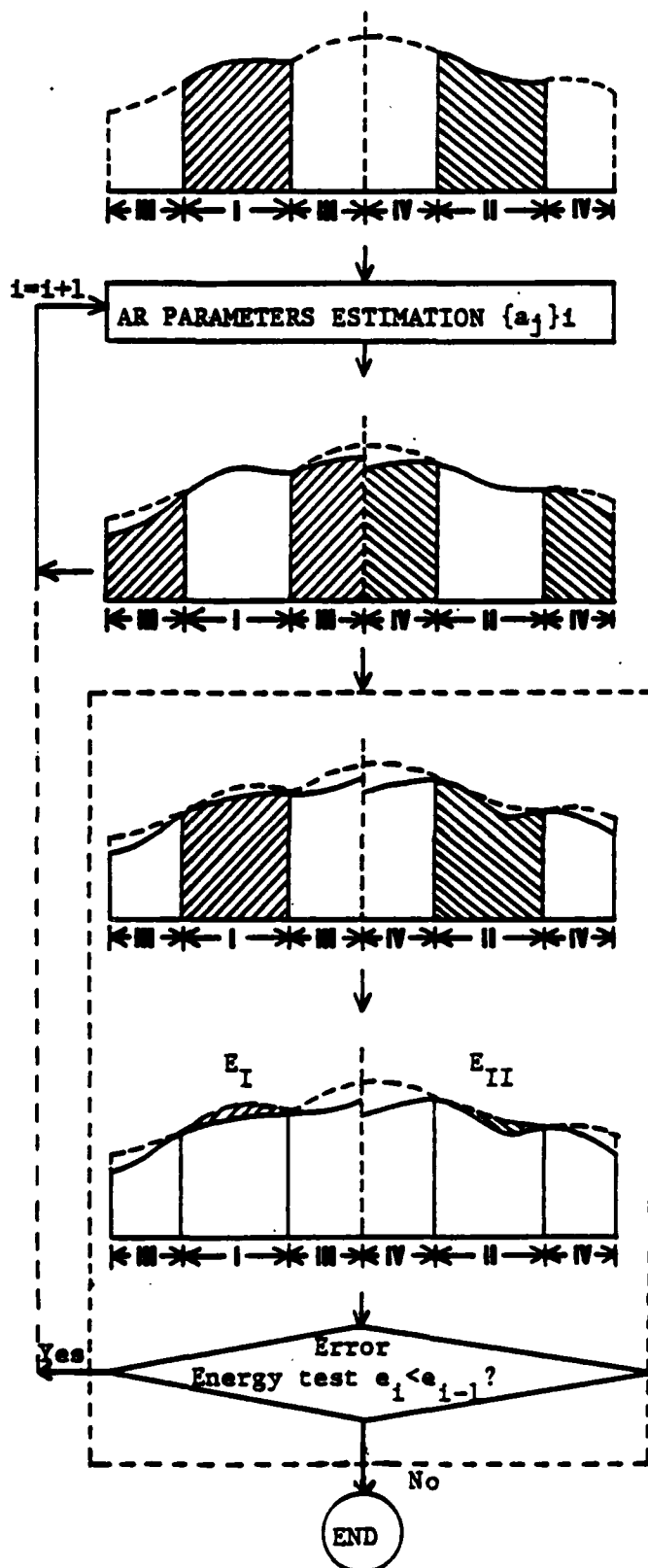


Fig 1

ITERATION ALGORITHM



1. Available data in regions I & II are used to extrapolate into regions III & IV.

2. Use data in regions I + II + III + IV to estimate the parameters $\{a_j\}_i$, where i represents the iteration number.

3. Use data in I and $\{a_j\}_i$ to extrapolate into region III. Use data in II and $\{a_j\}_i$ to extrapolate into region IV.

Convergence Test

a. Use data in III and $\{a_j\}_i$ to estimate new data values in region I. Use IV and $\{a_j\}_i$ to estimate new data values in region II.

b. Calculate error

$$e_i = E_I + E_{II}$$

c. For the resultant data is in step 3: If $e_i < e_{i-1}$, $i+1 \rightarrow i$, go from step 3 to 2 otherwise iteration stopped.

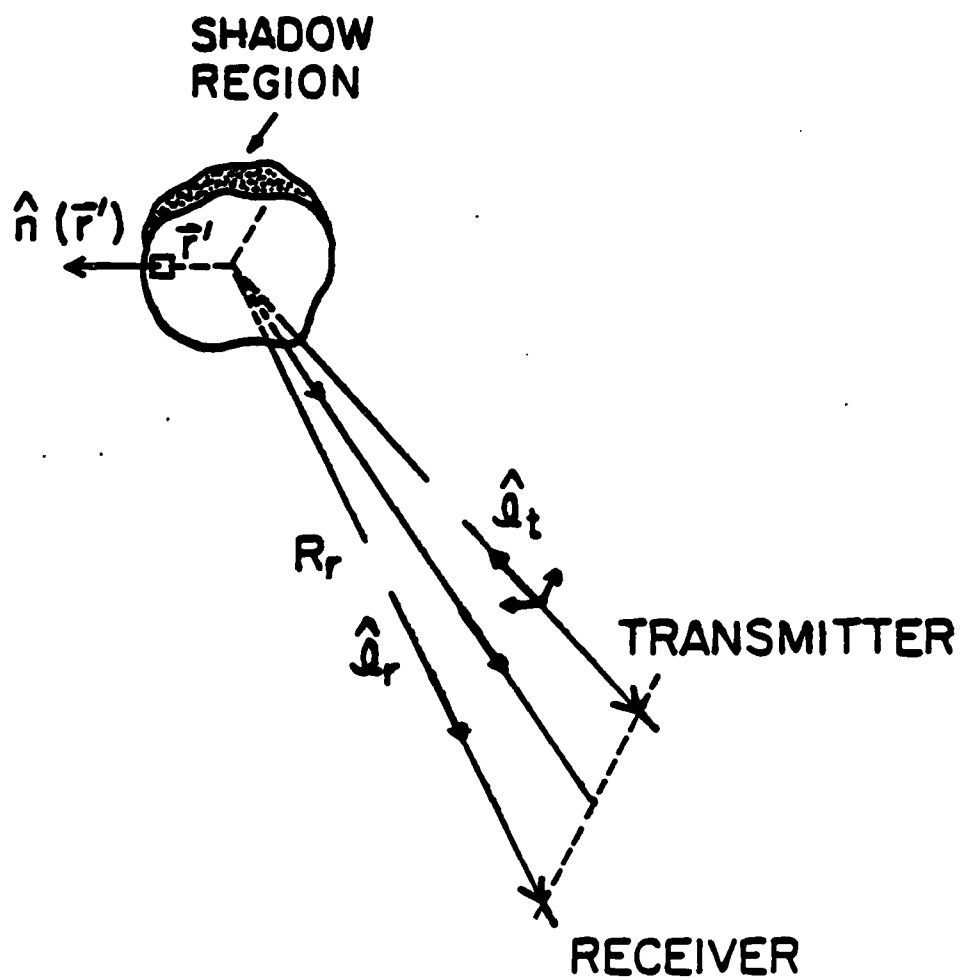
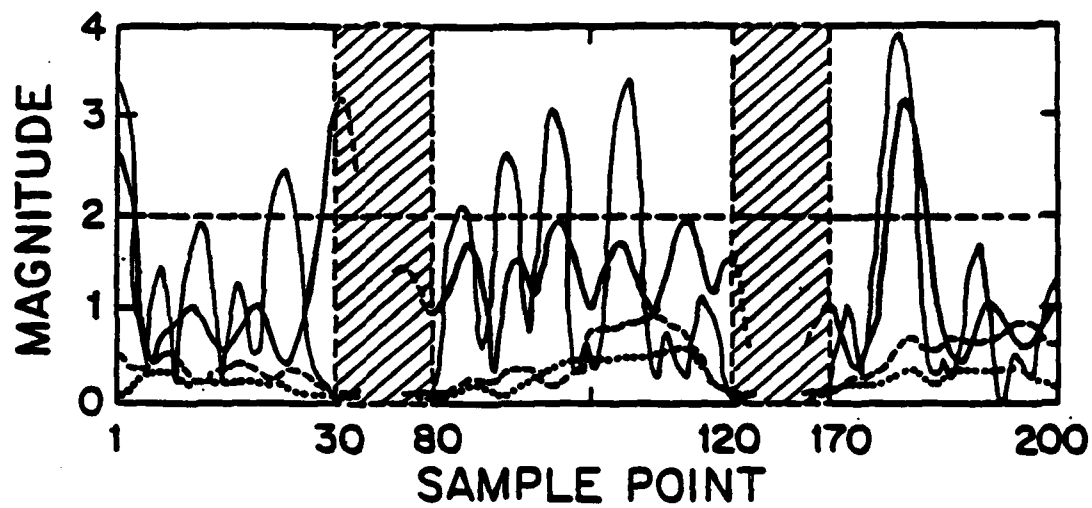
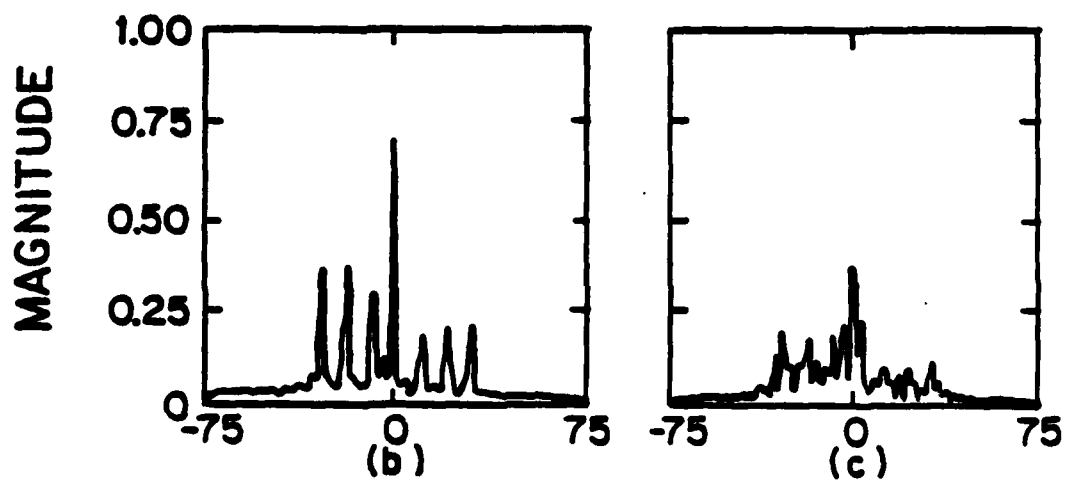


Fig. 3

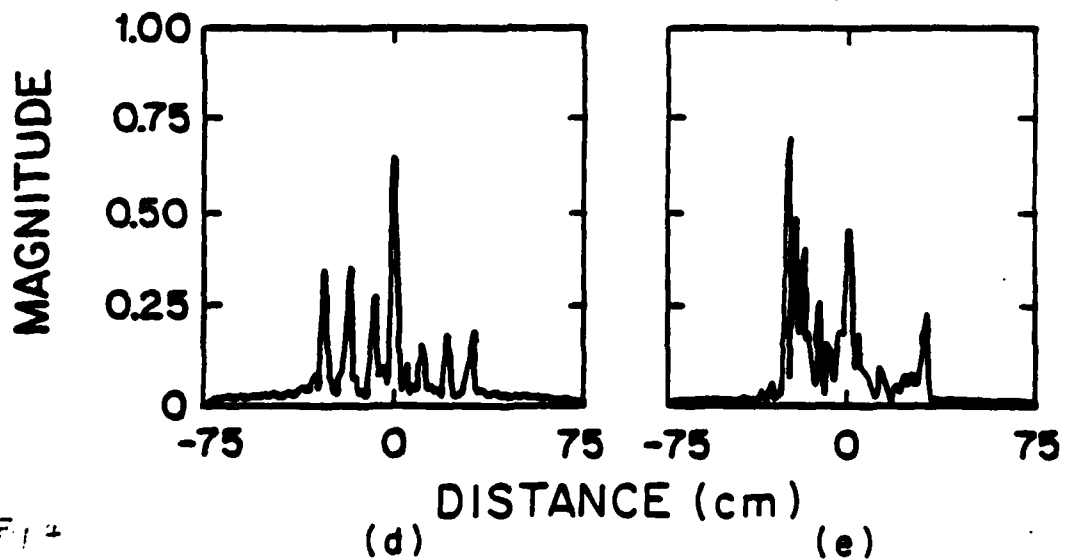


(a)



(b)

(c)



(d)

(e)

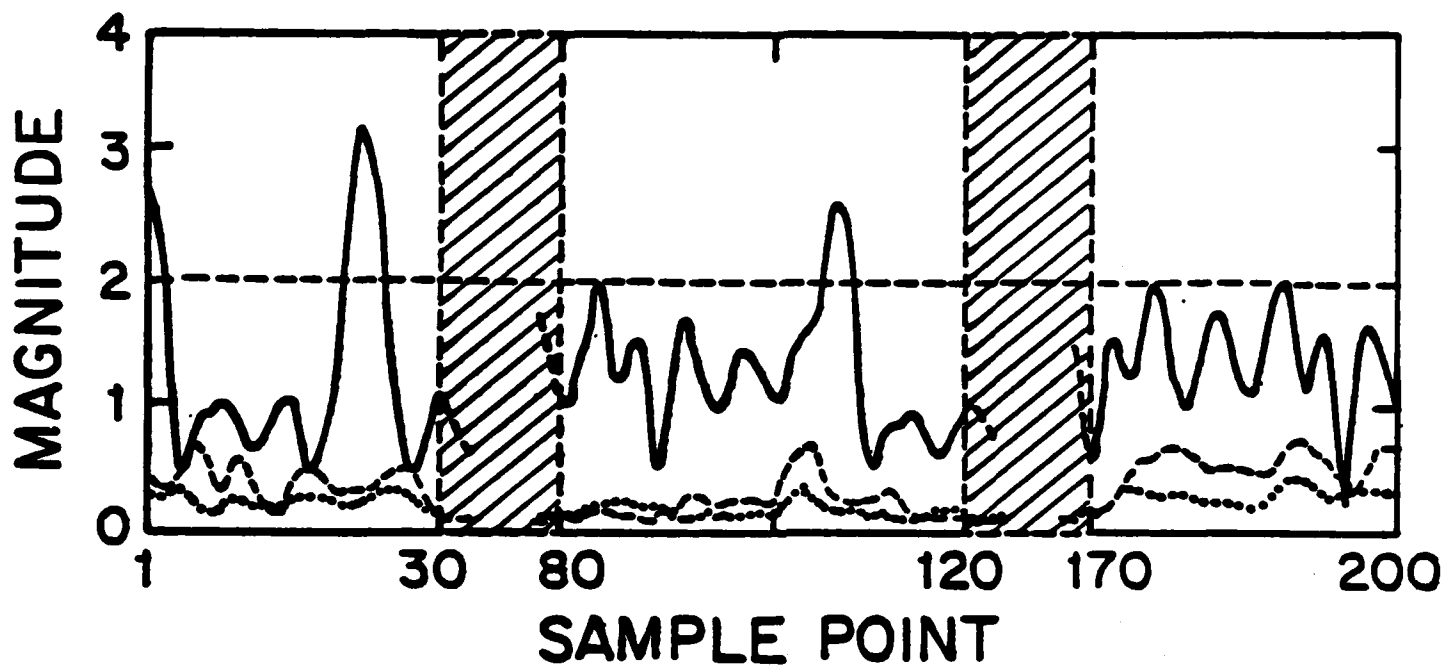


Fig. 5

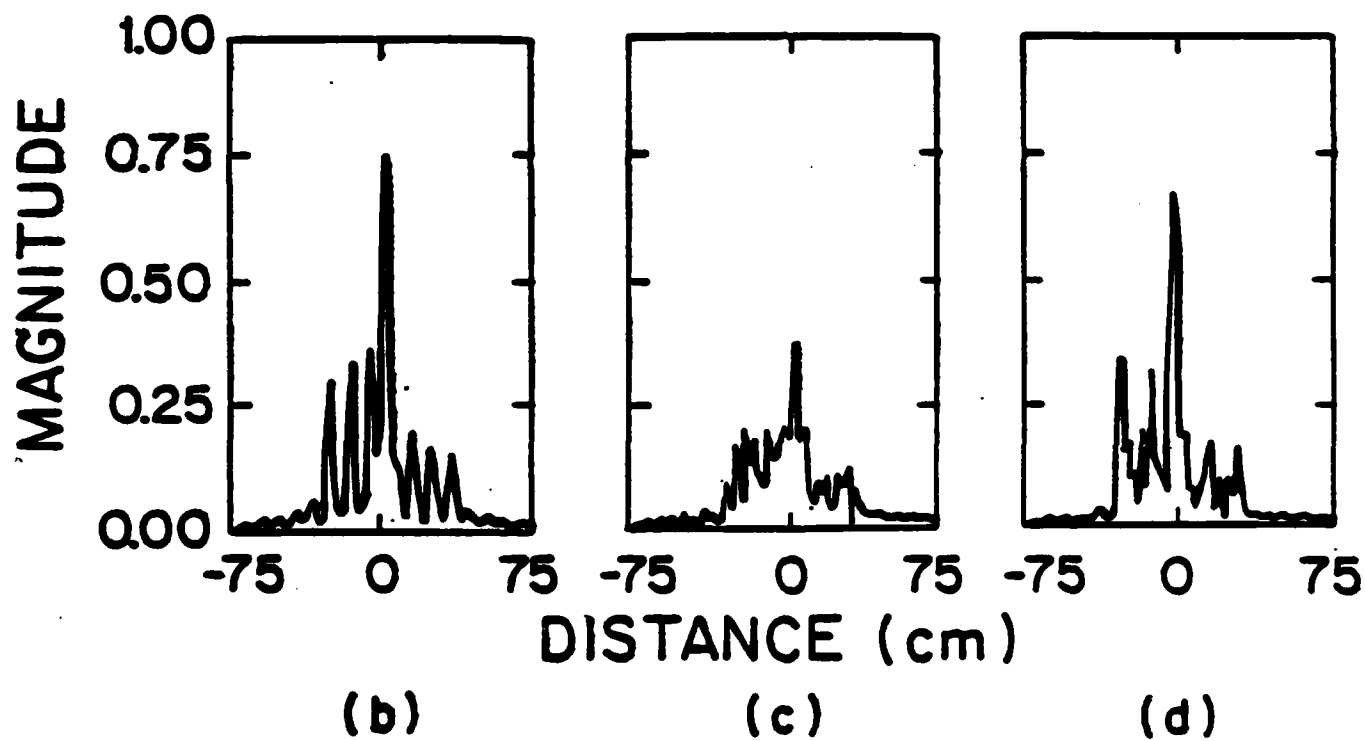
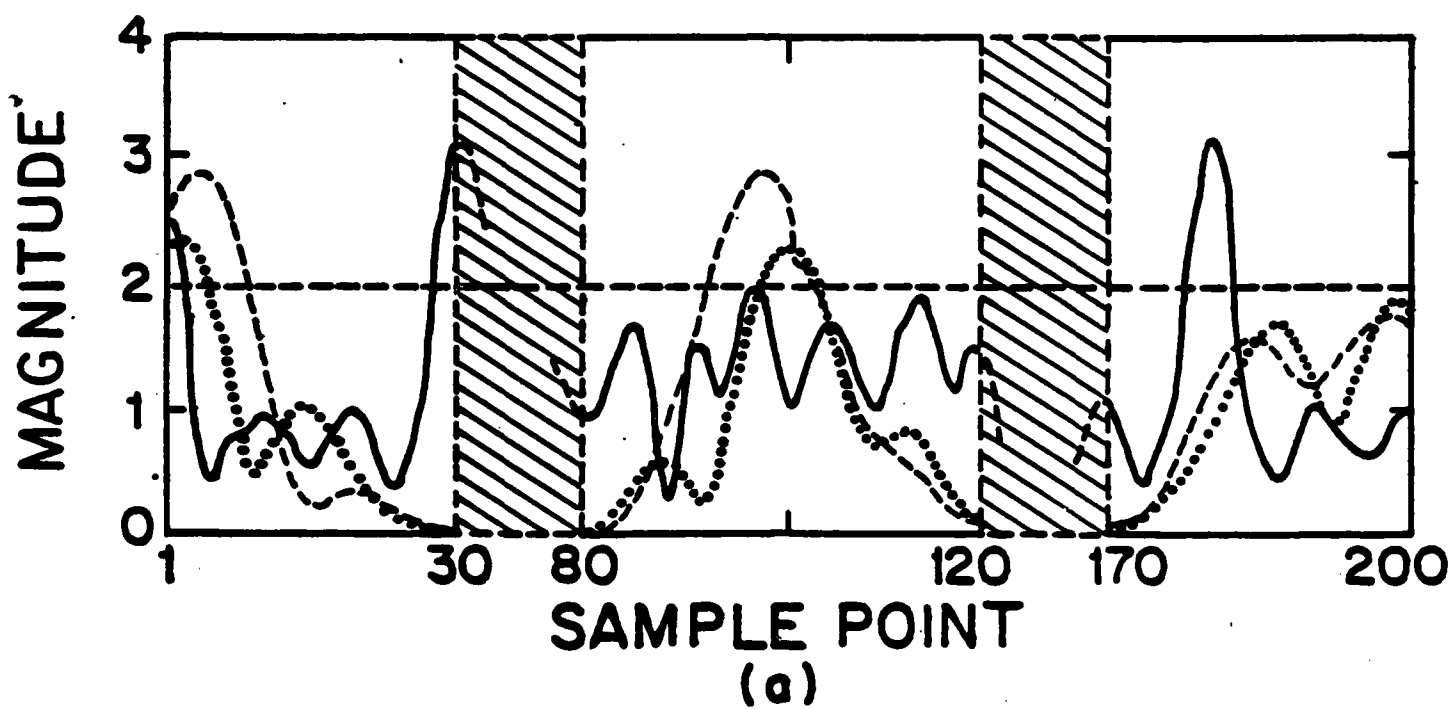
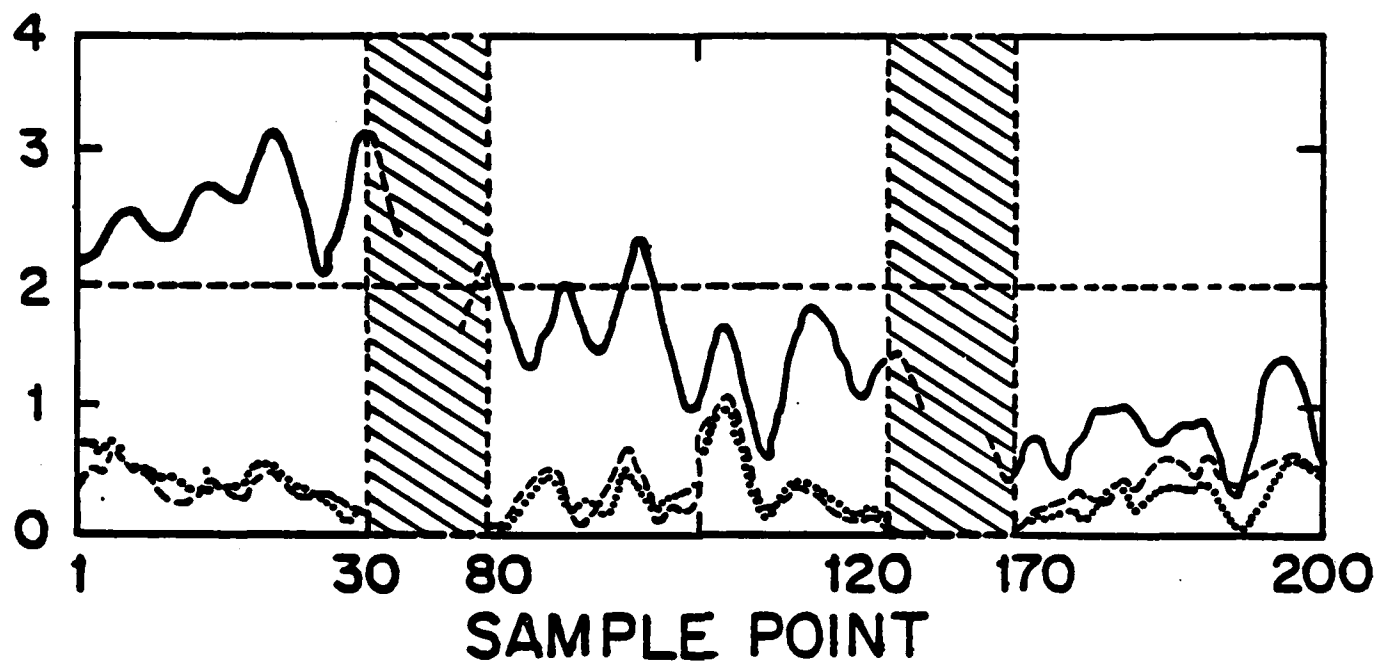
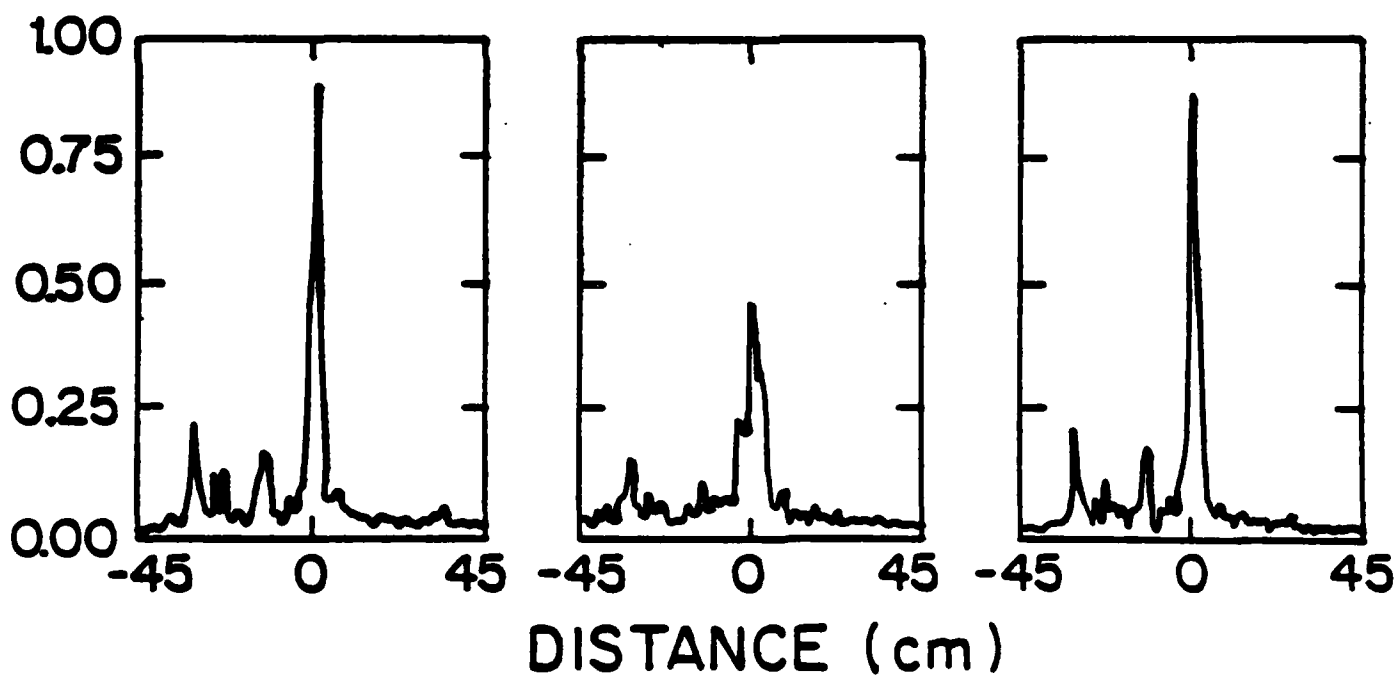


Fig 6



(a)

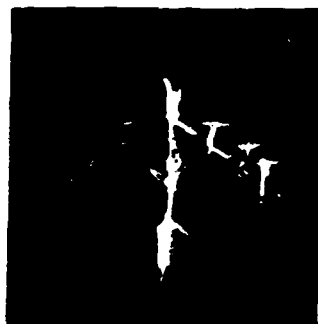


(b)

(c)

(d)

Fig. 7



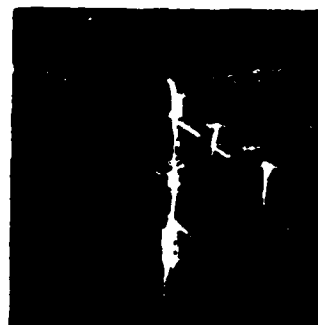
(a)



(b)



(c)



(d)



(e)



(f)



(g)

ARCHITECTURES FOR OPTO-ELECTRONIC ANALOGS OF SELF-ORGANIZING NEURAL NETWORKS

Nabil H. Farhat
University of Pennsylvania
Electrical Engineering Department
Electro-Optics and Microwave-Optics Laboratory
Philadelphia, PA 19104-6390

Abstract

Architectures for partitioning opto-electronic analogs of neural nets into input/output and internal units to enable self-organization and learning where a net can form its own internal representations of the "environment" are described.

1. INTRODUCTION: In our preceeding work on optical analogs of neural nets, [1],[2], the nets described were programmed to do a specific computational task, namely a nearest neighbor search by finding the stored entity that is closest to the address in the Hamming sense. As such the net acted as a content addressable associative memory. The programming was done by computing first the interconnectivity matrix using an outer-product recipe given the entities we wished the net to store and become familiar with followed by setting the weights of synaptic interconnections or links between neurons accordingly.

In this paper we are concerned with architectures for opto-electronic implementation of neural nets that are able to program or organize themselves under supervised conditions, i.e., of nets that are capable of (a) computing the interconnectivity matrix for the associations they are to learn, and (b) of changing the weights of the links between their neurons accordingly. Such self-organizing networks have therefore the ability to form and store their own internal representations of the entities or associations they are presented with.

Multi-layered self-programming nets have been described recently [3]-[5] where the net is partitioned into three groups. Two are groups of visible or external input/output units or neurons that interface with the outside world i.e., with the net environment. The third is a group of hidden or internal units that separates the input and output units and participates in the process of forming internal representations of the associations the net is presented with, as for example by "clamping" or fixing the states of the input and output neurons to the desired associations and letting the net run through its learning algorithm to arrive ultimately at a specific set of synaptic weights or links between the neurons that capture the underlying structure of all the associations presented to the net. The hidden units or neurons prevent the input and output units from communicating with each other directly. In other words no neuron or unit in the input group is linked directly to a neuron in the output group and vice-versa. Any such communication must be carried out via the hidden units. Neurons within the input group can communicate with each other and with hidden units and the same is true for neurons in the output group. Neurons in the hidden group can not communicate with each other. They can only communicate with neurons in the input and output groups as stated earlier.

Two adaptive learning procedures in such partitioned nets have attracted considerable attention. One is stochastic involving a simulated annealing process [6],[7] and the other is deterministic involving an error back-propagation process [4]. There is general agreement however; that because of their iterative nature, serial digital computation of the links with these algorithms is very time consuming. A faster means for carrying out the required computations is needed. Never-the-less the work mentioned represents a milestone in that it opens the way for powerful collective computations in multilayered neural nets and in that it dispels earlier reservations [8] about the capabilities of early models of neural nets such as the Perceptron [9] when the partitioning concept is introduced. What is most significant and noteworthy, in our opinion, is the ability to now define buffered input and output groups with unequal number of neurons in a net which was not possible with earlier nets where all neurons participate in defining the initial (input) and final (output) states of the net.

2. ANALOG IMPLEMENTATIONS: Optics and opto-electronic architectures and techniques can play an important role in the study and implementation of self-programming networks and in speeding-up the execution of learning algorithms. We have done some exploratory work in this regard to see how the neurons in an opto-electronic analog of a neural net can be partitioned into groups with specific interconnection patterns. Here, for example, a method for partitioning an opto-electronic analog of a neural net into input, output, and internal units with the selective communication pattern described earlier to enable, stochastic learning, i.e., carrying out a simulated annealing learning algorithm in the context of a Boltzmann machine formalism is described. (see Fig. 1(a)). The arrangement shown in Fig. 1(a) derives from the neural network analogs we described earlier [2]. The

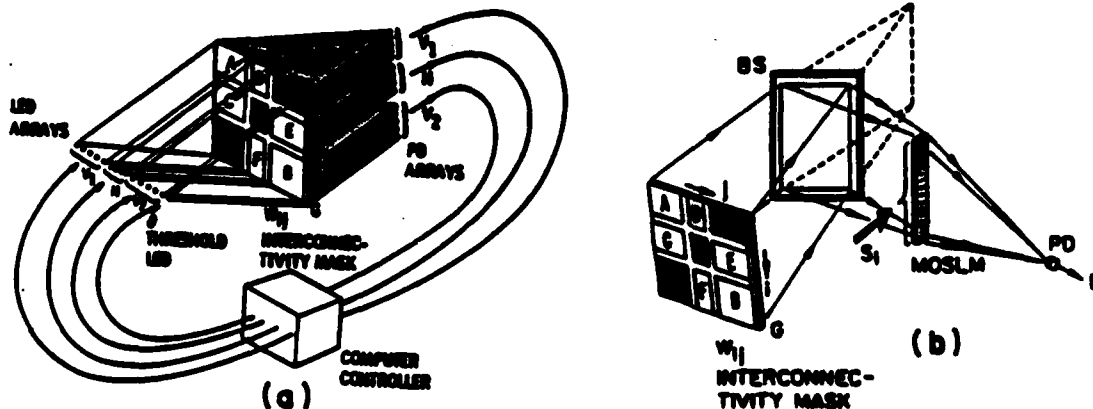


Fig. 1. Partitioning concept (a) and method for rapid determination of the net's energy E .

network, consisting of say N neurons, is partitioned into three groups. Two groups, V_1 and V_2 , represent visible or exterior units that can be used as input and output units respectively. The third group H are hidden or internal units. The partition is such that $N_1 + N_2 + N_3 = N$ where subscripts 1, 2, 3 on N refer to the number of neurons in the V_1 , V_2 and H groups respectively. The interconnectivity matrix, designated here as W_{ij} , is partitioned into nine submatrices, A, B, C, D, E, and F plus three zero matrices shown as blackened or opaque regions of the W_{ij} mask. The LED array

represents the state of the neurons, assumed to be unipolar binary LED on = neuron firing, LED off = neuron not-firing. The W_{ij} mask represents the strengths of interconnection between neurons in a manner similar to earlier arrangements [2]. Light from the LEDs is smeared vertically over the W_{ij} mask with the aid of an anamorphic lens system (not shown in Fig. 1(a)) and light emerging from rows of the mask is focused with the aid of another anamorphic lens system (also not shown) onto elements of the photodetector (PD) array. Also we assume the same scheme utilized in [2] for realizing bipolar values of W_{ij} in incoherent light is adopted here, namely by separating each row of the W_{ij} mask into two subrows and assigning positive values W_{ij}^+ to one subrow and negative values W_{ij}^- to the other, then focusing light emerging from the two subrows separately onto pairs of adjacent photosite connected in opposition in the V_1 , V_2 and H segment of the photodetector array. Submatrix A with $N_1 \times N_1$ elements, provides the interconnection weights of units or neurons within group V_1 . Submatrix B with $N_2 \times N_2$ elements, provides the interconnection weights of units within V_2 . Submatrices C (of $N_1 \times N_3$ elements) and D (of $N_3 \times N_1$ elements) provide the interconnection weights between units of V_1 and H and submatrices E (of $N_2 \times N_3$ elements) and F (of $N_3 \times N_2$) provide the interconnection weights of units of V_2 and H. Units in V_1 and V_2 can not communicate with each other directly because locations of their interconnectivity weights in the W_{ij} matrix or mask are blocked out (blackened lower left and top right portion of W_{ij}). Similarly units within H do not communicate with each other because locations of their interconnectivity weights in the W_{ij} mask are also blocked out (center blackened square of W_{ij}). The LED element θ is always on to provide a fixed or adaptive threshold level to all other units by contributing to the light focused onto only negative photosites of the photodetector (PD) arrays.

By using a computer controlled nonvolatile spatial light modulator to implement the W_{ij} mask in Fig. 1(a) and including a computer/controller as shown the scheme can be made self-programming with ability to modify the weights of synaptic links between its neurons to form internal representations of the associations or patterns presented to it. This is done by fixing or clamping the states of the V_1 (input) and V_2 (output) groups to each of the associations we want the net to learn and by repeated application of the simulated annealing procedure with Boltzmann, or other, stochastic state update rule and collection of statistics on the states of the neurons at the end of each run when the net reaches thermodynamic equilibrium.

For each clamping of the V_1 and V_2 units to one of the associations, annealing is applied, starting from an arbitrary W_{ij} , with switching states of units in H until thermodynamic equilibrium is reached. The state vector of the entire net, which represents a state of global energy minimum, is then stored by the computer. This procedure is repeated for each

association several times recording the final state vectors every time. The probabilities P_{ij} of finding the i -th and j -th neurons in the same state are then obtained. Next with the output units V_2 unclamped to let them free run like the H units the above procedure is repeated for the same number of annealings as before and the probabilities P'_{ij} are obtained. The weights W_{ij} are then incremented by $\Delta W_{ij} = \eta(P_{ij} - P'_{ij})$ where η is a constant that controls the speed and efficacy of learning. Starting from the new W_{ij} the above procedure is repeated until a steady W_{ij} is reached at which time the learning procedure is complete. Learning by simulated annealing requires calculating the energy E of the net [3],[5]. A simplified version of a rapid scheme for obtaining E opto-electronically is shown in Fig. 1(b). A slight variation of this scheme that can deal with the bipolar nature of W_{ij} would actually be utilized. This is not detailed here because of space limitation.

3. REMARKS: The partitioning architecture described is extendable to multilayered nets of more than three layers and to 2-D arrangement of neurons. Learning algorithms in such layered nets lead to multivalued W_{ij} . Therefore high-speed computer controlled SLMs with graded pixel response are called for. Methods of reducing the dynamic range of W_{ij} or for allowing the use of W_{ij} with ternary weights are however under study to enable the use of commercially available nonvolatile SLM devices that are mostly binary e.g., Litton's MOSLM.

4. ACKNOWLEDGEMENT: The work reported was supported by grants from DARPA/NRL, The Army Research Office, and the University of Pennsylvania Laboratory for Research on the Structure of Matter.

REFERENCES:

1. Psaltis, D. and N. Farhat, Digest of the 13-th Congress of Intern. Commiss. on Optics, ICO-13, Saporro, Japan, 1984. Also, Opt. Lett., Vol. 10, pp. 98-100, 1985.
2. Farhat, N.H., et. al., App. Optics, Vol. 24, pp. 1469-1475, 1985.
3. G.F. Hinton, et. al., Carnegie-Mellon University Report No. CMU-CS-84-119, May (1984).
4. D.E. Rumelhart, G.E. Hinton and R.J. Williams, Institute for Cognitive Science Report 8506, Univ. of California, San Diego, Sept. 1985.
5. T.J. Sejnowski and C.R. Rosenberg, Johns Hopkins University, Electrical Engineering and Computer Science Technical Report No. JHU/EECS-96/01 (1986).
6. N. Metropolis, et. al., J. Chem. Phys., Vol. 21, 6, pp. 1087-1092, June, 1953.
7. S. Kirkpatrick, et. al., Science, Vol. 220, pp. 671-680, May 1983.
8. M.L. Minsky and S. Papert, Perceptrons, MIT Press, Cambridge, MA, (1969).
9. F. Rosenblatt, Principles of Neuro-Dynamics: Perceptions and the Theory of Brain Mechanisms, Spartan Books, Wash. D.C., 1962.

Phased Array Antenna Pattern Synthesis By Simulated Annealing

N.H. Farhat and B. Bai

ABSTRACT: A new procedure is described for optimum phased array synthesis. The synthesis is optimized by a simulated annealing process in which the energy function is directly related to the far field intensity of a phased array. Numerical simulation results are presented. A possible optical-digital hybrid implementation that can perform the required computation at higher speed than a pure digital implementation is discussed.

1 INTRODUCTION

For the synthesis of an antenna array with uniformly spaced elements it is well known that, if the current distribution function is not restricted, a Dolph-Chebyshev distribution function over the antenna gives rise to an optimum pattern which has the lowest sidelobe level for a specified mainbeam width [1]. However, if for the purpose of easy practical implementation, the distribution function is restricted to some specific set, other methods have to be investigated and used for optimum synthesis. The simulated annealing method presented here is, by our study, one of the choices for optimum synthesis of phased arrays with restricted distribution functions. The synthesis is optimal in the sense that the lowest sidelobe level is achieved while the specified mainbeam width is maintained. This method can be used for both microwave phased arrays and optical arrays. In our study so far, we have been mainly concerned with optical arrays, which appear to be technologically feasible with present electronic and

*The authors are with the Electro-Optics and Microwave Optics Laboratory, the Moore School of Electrical Engineering, University of Pennsylvania, Philadelphia, PA 19104.

optical technologies. Hence, the parameters assumed in the simulations below are relevant to the optical case, but the method and conclusions apply to phased arrays in general.

2 SIMULATED ANNEALING METHOD

Metropolis *et al.* introduced the simulated annealing algorithm for calculating the properties of any system of interacting individual molecules [2]. The algorithm was previously applied to combinatorial optimization problems, including physical design of computers, and the traveling salesman problem [3]. The method can be extended for general optimization problems. For the system to be optimized, an "energy" or "cost" function E is first established and a dynamic variable T , the "temperature" of the system, is chosen to control the process. Starting at a high "temperature", the system is slowly cooled down, until the system "freezes" and reaches the optimum state in a manner similar to annealing of a crystal during growth to reach a near perfect structure. At each "temperature", a change in the system is made according to a certain rule, and then the "energy" or "cost" change of the system ΔE is calculated. If $\Delta E \leq 0$, the system alteration is retained and the process is continued. The acceptance or rejection of the alteration or change of grain of the system when $\Delta E > 0$ is treated probabilistically. Accordingly, the Boltzman factor $f(\Delta E) = \exp(-\frac{\Delta E}{KT})$ is calculated, where K is a constant whose dimension depends on the dimensions of ΔE and T . Then a random number R uniformly distributed in the interval $[0, 1)$ is chosen. If $R \leq f(\Delta E)$, the change of grain is retained; on the other hand, if $R > f(\Delta E)$, the change is discarded, that is, the system before change is used for the next step of the process. This procedure is repeated for each "temperature" until the system is optimized by arriving at a global energy minimum. The choices of K and the initial T are crucial for the success and speed of convergence of simulated annealing process. Because of the probabilistic Boltzman selection rule of the $\Delta E > 0$ case, the process can always get out of a local minimum of the "energy" or "cost" function in which it could get trapped and proceed to the desired global minimum. This makes simulated annealing different from iterative improvement procedure [3]-[6].

3 PHASED ARRAY SYNTHESIS

For a 2-dimensional phased array with $(2M+1) \times (2N+1)$ identical subapertures, the far field is the product of its subaperture factor and its array factor. The array factor can be written as,

$$Q(f_x, f_y) = \sum_{m=-M}^M \sum_{n=-N}^N W_{mn} \exp[-j2\pi(mAf_x + nBf_y)] \quad (1)$$

where, A and B are the spacing between elements in an orthogonal array coordinate; $f_x = \frac{x}{\lambda R_0}$, $f_y = \frac{y}{\lambda R_0}$, x and y being the transverse far field coordinates, and R_0 is the distance between point (x, y) and the array origin.

Since the subaperture factor is fixed for a given subaperture function and it varies much more slowly than the array factor, the effect of the subaperture factor is insignificant and hence ignored in the present synthesis. The array factor $Q(f_x, f_y)$ will be studied by changing the weighting factor W_{mn} for all possible m and n to achieve the optimum radiation pattern.

The "energy" or "cost" function in simulated annealing can be established in many different ways for phased array synthesis. Since our primary work is done for optical and infrared phased arrays and this kind of array has a relatively large size compared to the wavelength λ used (λ on the order of 10^{-6} m), the beam width is very small (on the order of 10^{-2} degrees). It is important to achieve the lowest sidelobe level. For this purpose, one obvious way to choose the "energy" or "cost" function for phased array synthesis would be the energy outside a specified main lobe. When this energy function is minimized, under the assumption that the total energy remains constant, it could be expected that the energy would become concentrated in the main beam. Consequently, the relative sidelobe level could be minimized. However, from simulations we have run, it turns out that this energy constraint cannot minimize the sidelobe level, since minimizing the energy does not necessarily constrain the peak sidelobe level. In the simulation presented here, the intensity E associated with the highest sidelobe level is used as the "energy" or "cost" function for simulated annealing. Of course, if necessary, a constraint about the beamwidth could be included in the "energy" or "cost" function. When the "energy" is minimized, the relative sidelobe level is now also minimized. The beamwidth at the final run will be taken as the optimum beamwidth associated with the final W_{mn} .

weights. The relationship of beamwidth and sidelobe level is then optimum in the sense of Dolph-Chebyshev, that is, the sidelobe level is the lowest for the given beamwidth.

4 SIMULATION

Since the simulated annealing process is the same for a 2-dimensional array as for a 1-dimensional array and considering the limited computation power of the MICRO PDP-11 computer available for our simulation, a 1-dimensional array is used in our study. The 1-dimensional array is also assumed to be a continuous one with many desired pixels. Each of the pixels acts as a subaperture. The simulation starts with a uniform distribution (all subapertures with 1 or -1). The far field pattern is shown in Fig.1(a) for this uniform distribution case and has the usual -13.3(dB) sidelobe level. The distribution function is restricted to the set of 1, -1, which means real transmittance with binary phase (phase = 0 or π) modulation. Then, simulated annealing is carried out by just changing the sign of each subaperture in turn, calculating the intensity of the highest sidelobe and applying the algorithm for each change. At each "temperature" for the simulated annealing algorithm, if either the number of accepted changes on randomly selected elements exceeds $\frac{1}{5}$ of the total subaperture numbers or the number of attempts exceeds 10 times the total subaperture numbers, the process goes to the next lower "temperature". If the desired number of acceptances is not achieved at three successive "temperatures", the process is considered "frozen" and the optimum pattern is attained. The final optimum result is given in Fig.1(b). This simulation is done for an array of 41 subapertures. The subaperture size is assumed to be equal to the spacing A between subapertures and is taken to be 61λ (figure relevant for optical arrays). The element distribution function that gives the final optimum result is shown in table 1. This function is seen to be asymmetric. From formula (1) it is seen that two elements with opposite index, say $n = -10$ and $n = 10$ for the 1-dimensional case, have different phases and therefore their contributions to the far field factor are different. In general, the array factor given in formula (1) is a complex quantity. Although it is frequently thought that the optimum array factor is real, there seems to be no reason to exclude a complex quantity as an optimum

array factor. Even if the array factor is a complex quantity and asymmetric, it can be shown that the far field (power) pattern is symmetric for arrays with real weights. In our simulation, the weights are real (1 or -1) and the pattern in Fig.1(b) is therefore symmetric. The distribution function in table 1 for the optimum pattern shown in Fig.1(b) is for elements -18, -15, and -12 with weights equal to -1; if we make elements +18, +15, and +12 also with weights equal to -1, which gives a symmetric array factor, the pattern obtained will be that shown in Fig.1(c) and is seen not to be optimum. From the simulation, it is found that the result of the simulated annealing procedure is relatively robust for different initial distribution functions, that is, it eventually gives the same optimum pattern for different initial distribution functions, as long as the initial distribution function forms a pattern with a single main beam. The final weighting function in table 1 was obtained from a uniform initial distribution function (all weights= 1) and it is interesting that switching of weights happens for only a few elements (three). The function in table 1 gives an optimum pattern only for broad side direction. Like the Dolph-Chebyshev optimum function, the optimum function given by simulated annealing is different for different steering angles, but an optimal weight distribution can be computed for each steering angle. From the simulation result, it is seen that the optimum far field pattern has similar features to the pattern given by the Dolph-Chebyshev distribution function. In the Dolph-Chebyshev pattern, all the sidelobes have the same level for a specified beamwidth. A numerical example in [1] shows an 8-element array (element separation $d = 0.5\lambda$) with 25.8(dB) sidelobe level and 40.8° beamwidth. The optimum pattern given by our simulation shows nearly equal level side lobes which are minimized for the given beamwidth.

5 DISCUSSION

Simulated annealing is a modification of the iterative improvement algorithm [4]. It is physically more meaningful and can be computed more systematically than the iterative improvement [4]. Physically, the simulated annealing process is analogous to the cooling of atoms in crystal growth: careful annealing produces a defect-free crystal, rapid annealing produces a defective crystal or glass [3]. The probabilistic treatment with the probability function $P(\Delta E) = \exp(-\frac{\Delta E}{KT})$

provides a way to accept the unfavorable changes and is easy to compute. From our simulation, it has been found that the simulated annealing algorithm seems always to give better performance than the iterative improvement algorithm.

Since simulated annealing is a modified iterative improvement process, it takes a relatively long time to do an optimization problem just as iterative improvement does in a computer calculation. The phased array synthesis in our simulation runs for one hour or so for an array of 41 elements on a MICRO PDP-11 computer. Finding an efficient scheme to reduce the excessive amounts of computer time on most optimum problems has always been of concern [5]-[7]. Otherwise, if enough computation power is available, iterative improvement can be run from random starts for many times to approach the optimum state. Fast opto-digital computing schemes similar to those described in [8] may also be considered for phased array synthesis by simulated annealing. It is understood that the far field is the Fourier transform of the array distribution function. An optical lens can be used for computing the Fourier transform as the distribution function is inputted to the front focal plane of the lens via, for example, an appropriate computer driven spatial light modulator (SLM). The Fourier transform in the back focal plane can be recorded and fed to the computer/controller to make the simulated annealing decision. The outcome is feedback to the SLM to change the distribution function in the front focal plane. The hybrid opto-digital scheme will do the Fourier transform instantly. In this fashion the computation associated with the Fourier transform can be virtually eliminated assuming a high speed SLM and computer interface are utilized. An opto-electronic Boltzman machine for accelerating the selection rule has also been proposed earlier in [8]. This process can be repeated for every step in simulated annealing. Also, a Cauchy probability selection rule, instead of the Boltzman selection rule, can be used to speed up the whole annealing process further [7].

6 ACKNOWLEDGEMENT

This work was supported by DARPA/NRL and with partial support from the Air Force Office of Scientific Research and the Army Research Office.

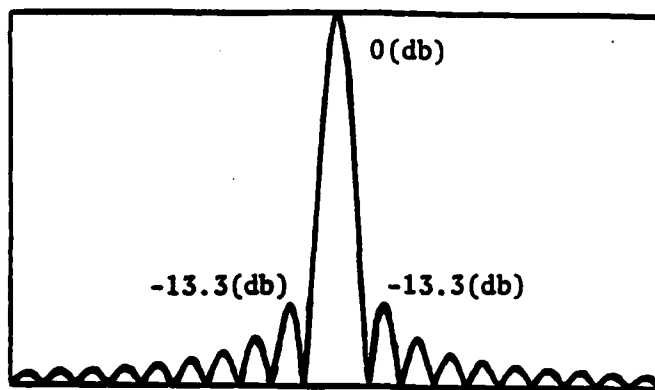
References

- [1] C. L. Dolph, "A current distribution for broadside arrays which optimizes the relationship between beam width and side-lobe level", *Proc. IRE.* 34, pp.335-348, June 1946.
- [2] N. Metropolis, *et al.*, "Equation of state calculations by fast computing machines", *J. Chem. Phys.* 21, pp.1087-1092, June 1953.
- [3] S. Kirkpatrick, *et al.*, "Optimisation by simulated annealing", *Science* 220, pp.671-680, May 1983.
- [4] W.E. Smith, *et al.*, "Reconstruction of objects from coded images by simulated annealing", *Opt. Lett.* 8, pp.199-201, April 1983
- [5] B. Dunham, "Design by natural selection", *Synthese* 15, pp.254-258, 1983.
- [6] S. Lin, "Heuristic programming as an aid to network design", *Network* 5, pp.33-43, 1975
- [7] H. Ssu, "Fast Simulated Annealing with Cauchy Probability Density", *Neural Networks for Computing Conference*, Snowbird, Utah, April 1986
- [8] H. Barrett, *et al.*, "Optical Boltzman Machines", Post-deadline paper, *OSA Topical Meeting on Optical Computing*, Incline Village, NEV. (1985)

ELEMENT	-20	-19	-18	-17	-16	-15	-14	-13	-12	-11	-10	-9	-8	-7	-6	-5	-4	-3	-2	-1	0	1	2	3	4	5	6	7	8	9	10	11	12	13	14	15	16	17	18	19	20
WEIGHT	1	1	-1	1	1	-1	1	1	-1	1	1	1	1	1	1	1	1	1	1	1	1	1	1	1	1	1	1	1	1	1	1	1	1	1	1	1	1	1	1	1	1

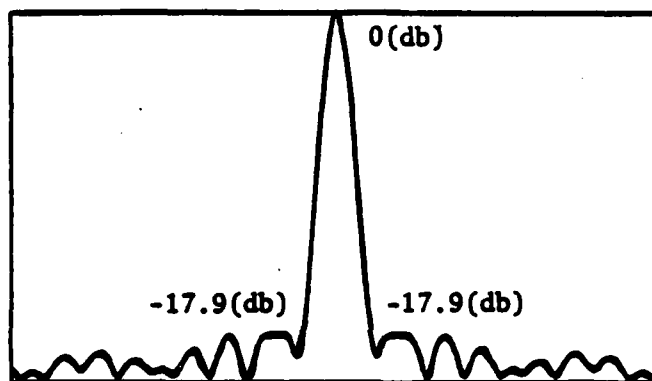
Table 1. The Final Distribution Function Weights for the Optimum Pattern

Fig. 1. Simulated annealing result. (a) Far field pattern for the uniform distribution; (b) Pattern obtained by simulated annealing; (c) Pattern obtained from a symmetrized version of the weights distribution obtained by simulated annealing.



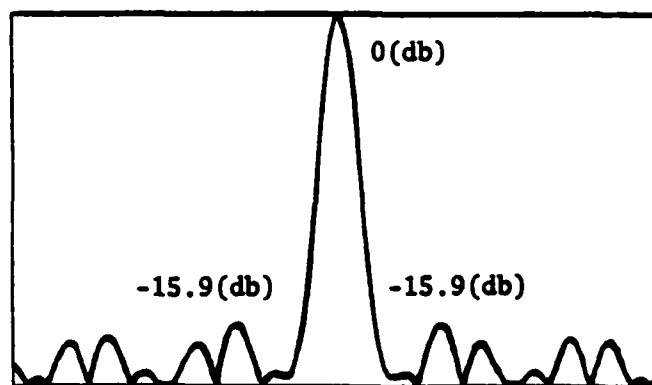
(a)

mainbeam width: 4.58×10^{-2} (degree)
view range: [-3, 3] (degree)



(b)

mainbeam width: 5.5×10^{-2} (degree)
view range: [-3, 3] (degree)



(c)

mainbeam width: 7.7×10^{-2} (degree)
view range: [-3, 3] (degree)

END

7-87

DTIC